

AEDC-TR-06-3



Engine Test Cell Aeroacoustics and Recommendations

**Dr. Christopher Tam
Department of Mathematics
Florida State University**

October 2007

Final Report for Period October 1, 2005 to September 30, 2006

Statement A: Approved for public release; distribution is unlimited.

**ARNOLD ENGINEERING DEVELOPMENT CENTER
ARNOLD AIR FORCE BASE, TENNESSEE
AIR FORCE MATERIEL COMMAND
UNITED STATES AIR FORCE**

NOTICES

When U. S. Government drawings, specifications, or other data are used for any purpose other than a definitely related Government procurement operation, the Government thereby incurs no responsibility nor any obligation whatsoever, and the fact that the Government may have formulated, furnished, or in any way supplied the said drawings, specifications, or other data, is not to be regarded by implication or otherwise, as in any manner licensing the holder or any other person or corporation, or conveying any rights or permission to manufacture, use, or sell any patented invention that may in any way be related thereto.

References to named commercial products in this report are not to be considered in any sense as an endorsement of the product by the United States Air Force or the Government.

DESTRUCTION NOTICE

For unclassified, limited documents, destroy by any method that will prevent disclosure or reconstruction of the document.

APPROVAL STATEMENT

This report has been reviewed and approved.



CHARLES R. VINING
Applied Technology Division
Test Operations Directorate

Approved for publication:

FOR THE COMMANDER



THOMAS P. FETTERHOFF
Director, Technology Division
Capabilities Integration Directorate

REPORT DOCUMENTATION PAGE				Form Approved OMB No. 0704-0188	
<small>The public reporting burden for this collection of information is estimated to average 1 hour per response, including the time for reviewing instructions, searching existing data sources, gathering and maintaining the data needed, and completing and reviewing the collection of information. Send comments regarding this burden estimate or any other aspect of this collection of information, including suggestions for reducing the burden, to Department of Defense, Washington Headquarters Services, Directorate for Information Operations and Reports (0704-0188), 1215 Jefferson Davis Highway, Suite 1204, Arlington, VA 22202-4302. Respondents should be aware that notwithstanding any other provision of law, no person shall be subject to any penalty for failing to comply with a collection of information if it does not display a currently valid OMB control number.</small>					
PLEASE DO NOT RETURN YOUR FORM TO THE ABOVE ADDRESS					
1. REPORT DATE (DD-MM-YYYY) xx-10-2007		2. REPORT TYPE Final Report		3. DATES COVERED (From – To) Oct. 1, 2005 – Sept. 30, 2006	
4. TITLE AND SUBTITLE Engine Test Cell Aeroacoustics and Recommendations				5a. CONTRACT NUMBER ATA-05-42	
				5b. GRANT NUMBER	
				5c. PROGRAM ELEMENT NUMBER	
6. AUTHOR(S) Dr. Christopher Tam Department of Mathematics Florida State University				5d. PROJECT NUMBER 11808	
				5e. TASK NUMBER	
				5f. WORK UNIT NUMBER	
7. PERFORMING ORGANIZATION NAME(S) AND ADDRESS(ES) C.W.K. Tam 2127 Orleans Drive Tallahassee, FL 32308-5924				8. PERFORMING ORGANIZATION REPORT NO. AEDC-TR-06-3	
9. SPONSORING/MONITORING AGENCY NAME(S) AND ADDRESS(ES) Arnold Engineering Development Center/XRS Arnold AFB, TN 37389				10. SPONSOR/MONITOR'S ACRONYM(S) AEDC/XRS	
				11. SPONSOR/MONITOR'S REPORT NUMBER(S)	
12. DISTRIBUTION/AVAILABILITY STATEMENT Statement A: Approved for public release; distribution is unlimited.					
13. SUPPLEMENTARY NOTES Available in the Defense Technical Information Center (DTIC).					
14. ABSTRACT Ground testing of turbojet engines in test cells necessarily involves very high acoustic amplitudes, often enough and severe enough that testing is interrupted and facility hardware and test articles are damaged. The acoustic response of test cells containing energetic jets is poorly understood and generally unpredictable. Nevertheless, there is a clear need to be able to predict deleterious acoustic events in advance of facility entry. A predictive capability would permit evaluating possible fixes in advance of the entry to preclude interruption of testing and damage to hardware, both of which are costly and disruptive of weapons systems program schedules. To establish the needed predictive capability, the Arnold Engineering Development Center (AEDC) is implementing a computational aeroacoustics (CAA) capability. This report by C. K. Tam is one of several steps toward that goal. Here, Tam consolidates what is presently known about the aeroacoustics of jets and flowing ducts. The material presented includes analytical and semi-empirical models of various acoustic situations as well as test data. Also included is a proposal to ameliorate a particularly damaging acoustic event referred to as "super resonance." A future report will present CAA technology appropriate for numerical solution of the flow equations as applied to jet cells.					
15. Subject Terms					
16. SECURITY CLASSIFICATION OF:			17. LIMITATION OF ABSTRACT	18. NUMBER OF PAGES	19A. NAME OF RESPONSIBLE PERSON
A. REPORT	B. ABSTRACT	C. THIS PAGE			Stephen A. Bancroft
U	U	U	U	109	19B. TELEPHONE NUMBER (Include area code) 931-454-6418

PREFACE

The work reported herein was conducted by the Arnold Engineering Development Center (AEDC), Air Force Materiel Command (AFMC), at the request of AEDC/XRS. The results of the research were obtained by Aerospace Testing Alliance, the operations, maintenance, information management, and support contractor for AEDC, AFMC, Arnold Air Force Base, Tennessee, under Subcontract ATA-0542 with consultant and author Prof. Christopher Tam, Florida State University, Tallahassee, FL. The ATA Project Manager was Ms. Bonnie D. Heikkinen, and the ATA Technical Monitor was Mr. Frederick L. Shope. The Air Force Project Manager was Mr. Jeffrey T. Staines. This work was funded through the Arnold Engineering Development Center, Arnold Air Force Base, TN, under Project Number 11808, “Modeling, Simulation and Analysis.”

The reproducibles used in the reproduction of this report were supplied by the author.

Introduction

One of the primary objectives of this report is to provide an overview of the sources of noise in engine test cells. An engine test cell is either a closed or a partially closed system. The solid surfaces that form the cell reflect back any incident acoustic waves. Thus a test cell creates a special acoustic environment depending on its geometrical design. Therefore, a second objective of this primer is to provide a simple mathematical analysis of the acoustic characteristics of a test cell. The noise source and the acoustic property of a test cell may under certain circumstances be directly coupled. When this happens, strong resonance may occur. This form of interaction tones is also discussed in this primer.

The acoustic spectrum in an engine test cell consists of tones and broadband noise. Whereas large amplitude tones are of primary concern to AEDC, the ability to predict and to understand broadband noise as well as medium and relatively small amplitude tones is an invaluable asset of a test engineer.

The source of acoustic energy in an engine test cell is the jet flow. One important part of the noise is the direct noise radiated from a high-speed turbulent jet. The noise components are essentially the same as those of a free jet. These noise components are discussed in Chapter 1. Another important noise component of an engine test cell is the noise generated by the coupling of the jet flow to the acoustic environment provided by the test cell. Usually, the coupling will result in tones occurring at the resonance frequencies. This type of resonant tone is discussed in Chapter 3. Chapter 2 is devoted to an examination of the acoustic environment existing in several types of engine test cells.

In Part II of this report, a method to suppress super resonance is proposed. This is followed by a recommendation on the establishment of a computational aeroacoustics (CAA) capability at AEDC.

OUTLINE

Introduction

Part I. Aeroacoustics of Engine Test Cells

Chapter 1. The noise of high-speed jets

- 1.1 Dimensional analysis of jet noise.
- 1.2 Power law.
- 1.3 The principal components of supersonic jet noise.
- 1.4 Turbulent mixing noise.
- 1.5 Broadband shock cell noise.
- 1.6 Screech tones.

Chapter 2. The acoustic environment formed by a test cell

- 2.1 Ejector type engine test cells.
- 2.2 High-altitude engine test cells.

Chapter 3. Interaction noise.

- 3.1 Instabilities of high speed jets.
- 3.2 Resonances.
- 3.3 Receptivity.
- 3.4 Amplified instability wave spectrum.
- 3.5 Super-Resonance.

References

Part II. Recommendations

- 1. Suppression of super-resonance: The method of barriers.
- 2. Establishing a CAA capability at AEDC.

Part I. Aeroacoustics of Engine Test Cells

Chapter 1. The Noise of High-Speed Jets

We will begin by performing a dimensional analysis of jet noise experiments. Such an analysis serves two useful purposes. First, it focuses attention on the variables or physical quantities that are under the control of an experimentalist or a test cell engineer. In addition, such an analysis will help to develop scaling formulas so that measured data from small scale models can be scaled up to full scale test cell conditions. Then, we will turn our attention to the three principal components of supersonic jet noise. Their characteristics will be examined and prediction methods will be discussed.

1.1 Dimensional Analysis of Jet Noise Experiments.

1.1.1 Derivation of Scaling Formula

We will consider an ideal jet noise experiment as shown in Figure 1.1. We will define an ideal experiment as one that satisfies the following conditions/assumptions.

1. The jet velocity profile at the nozzle exit is fairly uniform and the nozzle internal wall boundary layer is reasonably thin such that it has no strong effect on the radiated jet noise.
2. The level of upstream disturbances is normal and exerts no unusual influence on the noise of the jet.
3. Noise absorption by ambient air (humidity absorption) can be ignored or the measured data has been adjusted. In other words, only the lossless far field noise is considered.

Conditions/assumptions 1 and 2 have the explicit purpose of restricting our study to pure jet mixing noise. Here, to avoid misunderstanding, we wish to make it clear that an ideal experiment is not an impossible experiment. Recently, Viswanathan & Clark (2004) studied the effects of internal nozzle boundary layer thickness on jet noise. They concluded that unless there was flow separation inside the nozzle, boundary layer thickness had minimal impact on pure jet

mixing noise. Condition/assumption 2 is extremely important. It has been known since the seventies that upstream disturbances such as tones could have drastic effect on the level and spectral shape of the noise of a jet. In a more recent study, Viswanathan (2003) documented the contamination of jet noise by various components of rig noise in an improperly designed test facility. But once rig noise is sufficiently reduced, the quality of far field jet noise is significantly improved, opening the possibility of scalability. Assumption 3 is needed because humidity correction is frequency and hence jet size specific. Such correction cannot be scaled.

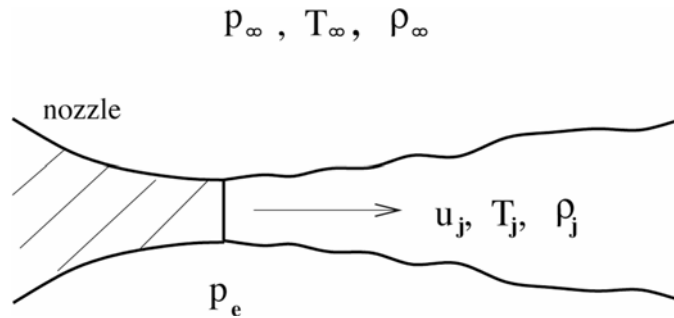


Figure 1.1. Input variables of an ideal jet noise experiment.

We will refer to the variables of an experiment that affect the noise radiated from the jet as input variables. We will call variables that are a part of the measured or processed data of the experiment “output variables.” The far field noise radiated from a jet is influenced by both the jet exit variables as well as the variables characterizing the ambient conditions. The ambient variables as shown in Figure 1.1 are p_∞ , ρ_∞ and T_∞ . But instead of T_∞ , we may use a_∞ , the ambient sound speed. The two variables are equivalent since $a_\infty = (\gamma R T_\infty)^{1/2}$. Also by the equation of state of a perfect gas, we have $\rho_\infty = p_\infty / a_\infty^2$, so that only two of the three ambient variables are independent. We will take p_∞ , a_∞ or T_∞ as the input ambient variables.

The jet variables are U_j (fully expanded jet velocity), p_e (pressure of jet at the nozzle exit), ρ_j , T_j (the fully expanded jet density and temperature), ν (kinematic viscosity) and D_j (the fully expanded jet diameter; in the case of subsonic and perfectly expanded supersonic jets, it is the same as D , the nozzle exit diameter). For subsonic and perfectly expanded supersonic jets, the static pressure of the jet at the nozzle exit is almost the same as the ambient pressure. That is

$p_e \cong p_\infty$. Thus p_e is not an independent input variable. We will defer the consideration of imperfectly expanded supersonic jets, for which p_e is not equal to p_∞ , until later.

Again, by the perfect gas law, we have $\rho_j = p_\infty / (RT_j)$. It follows that ρ_j is also not an independent input variable. In a jet noise experiment, it is more convenient to control the reservoir temperature, T_r , of the jet. By the energy equation, T_j is related to U_j and T_r by,

$$C_p T_r = C_p T_j + \frac{1}{2} U_j^2.$$

Hence, we may use T_r instead of T_j as an input variable. Therefore, the input variables characterizing the jet exit conditions are U_j , T_r , ν and D_j .

Let the three fundamental dimensions in mechanics, namely, mass, length and time be denoted by M , L and T , respectively. The dimensions of all the input variables are as shown, in parentheses, below,

$$p_\infty \left(\frac{M}{LT^2} \right), \quad a_\infty \left(\frac{L}{T} \right), \quad U_j \left(\frac{L}{T} \right), \quad T_r \left(\frac{L^2}{T^2 R} \right), \quad \nu \left(\frac{L^2}{T} \right), \quad D_j (L)$$

where R is the gas constant of the equation of state. It is to be noted that of the six variables, only p_∞ has dimension M . For this reason, it cannot be combined with other input variables to form a dimensionless group. Three independent dimensionless groups can be formed from the remaining five variables. A convenient choice of groupings leads to,

$$\frac{U_j}{a_\infty}, \quad \frac{T_r}{T_\infty}, \quad \frac{U_j D_j}{\nu} = \text{Re (Reynolds number of the jet)}.$$

Of interest in a jet noise experiment is the far field noise power spectral density S at a point with spherical coordinates (r, θ, ϕ) (the origin of the coordinate system is at the center of the nozzle exit) defined by,

$$\overline{p^2} = \int_0^\infty S(r, \theta, \phi, f) df. \quad (1.1)$$

where $\overline{p^2}$ is the time average of the square of the pressure fluctuations at (r, θ, ϕ) and f is the frequency. A simple dimensional analysis of (1) indicates that the dimensions of S are $(M^2 L^{-2} T^{-3})$. At the same time, f has the dimension of T^{-1} . On using the input variables to nondimensionalize the two output variables, two dimensionless groups can be formed. They are

$$\frac{S}{p_\infty^2 (D_j/U_j)} \quad \text{and} \quad \frac{f D_j}{U_j} \quad (\text{Strouhal number})$$

Now according to Buckingham pi theorem (see e.g.; Sedov, 1959; White, 2003), the dimensionless power spectral density must be a function of all the other dimensionless groups. Therefore, we may write,

$$\frac{S U_j}{p_\infty^2 D_j} = \frac{F\left(\frac{U_j}{a_\infty}, \frac{T_r}{T_\infty}, \frac{f D_j}{U_j}, \text{Re}, \theta\right)}{\left(\frac{r}{D_j}\right)^2}. \quad (1.2)$$

In (1.2), the inverse square dependence of sound on the distance of propagation is explicitly exhibited. For full scale jet engines, the jet Reynolds number is in the millions. At such a large value, the function F would be insensitive to the exact value of the Reynolds number. Another way of stating this is that F would have essentially reached its asymptotic value for large Re, so that it is practically independent of Re. This reduces (1.2) to,

$$\frac{S U_j}{p_\infty^2 D_j} = \frac{F\left(\frac{U_j}{a_\infty}, \frac{T_r}{T_\infty}, \frac{f D_j}{U_j}, \theta\right)}{\left(\frac{r}{D_j}\right)^2}. \quad (1.3)$$

In a laboratory experiment, if the Reynolds number is sufficiently large, say half a million or more, (1.3) would also apply. When this is true, (1.3) provides a basic formula for scaling small-scale jet noise data to full size prototype.

If in a series of experiments, the ambient pressure is practically the same, then we may replace p_∞^2 on the left side of (1.3) by p_{ref}^2 where p_{ref} is the reference pressure for the dB scale

$$\frac{SU_j}{p_{\text{ref}}^2 D_j} = \frac{\bar{F}\left(\frac{U_j}{a_\infty}, \frac{T_r}{T_\infty}, \frac{fD_j}{U_j}, \theta\right)}{\left(\frac{r}{D_j}\right)^2}. \quad (1.4)$$

However, we must caution that (1.4) is just an approximation. Eq. (1.3) is the correct scaling formula based on dimensional analysis.

1.1.2 Testing Scaling Formula

Scaling formulas (1.3) and (1.4) will now be applied to a variety of jet noise data. The purpose is to see if, indeed, data can be collapsed according to these formulas. Also, if there are problems collapsing the data, we wish to examine what might be the cause of the problems.

Figures 1.2(a) and 1.2(b) show two sets of data from Mach 2.0 jets measured by Seiner (see Tam, Golebiowski & Seiner 1996). One jet has an exit diameter of 3.60 in. (9.14 cm), the other 1.96 in. (4.98 cm). The spectrum data are plotted according to formula (1.4) as a function of Strouhal number. As can be seen from these figures, there is a good collapse of data in all directions of radiation in spite of the fact that the smaller jet is only slightly over 50% of the size of the larger jet. At Strouhal number above 6.0 the spectra of the smaller jet drops off abruptly. This is, most likely, an instrumentation problem. This part of the spectra should be disregarded.

Figures 1.3(a) and 1.3(b) show similar comparisons for two sets of Mach 0.5 data at a jet temperature ratio of 2.15 measured by Bhat (2001) of the Boeing company. In this case, the larger jet is 2.3 times larger. Over the angular sector from $\theta = 50^\circ$ to $\theta = 160^\circ$, the spectra collapse fairly well except at very low and very high Strouhal numbers. The problem at low Strouhal number, where the spectra of the large jet make a steep drop off, is due primarily to the low frequency filter. This part of the spectra should be ignored. At high Strouhal number, the

noise spectra of the smaller jet are consistently lower. Figures 1.4(a) and 1.4(b) show similar data at Mach 1.0. Again overall, the spectra seem to scale quite close to each other. But the collapse again is not good at very low and very high Strouhal numbers. The low Strouhal number problem is the same as the Mach 0.5 jet. The discrepancy at high Strouhal numbers is somewhat puzzling. A very appealing first suggestion is that it is a Reynolds number effect. The Reynolds numbers for the Mach 0.5 jets are 1.87×10^5 and 4.30×10^5 , respectively. The smaller jet has such a low Reynolds number, it is most likely that the initial boundary layer is transitional. On the other hand, the larger jet having a Reynolds number close to half a million should be nearly fully turbulent. One would, therefore, expect that the larger jet generates more high frequency noise. However, for the Mach 1.0 jets, the Reynolds numbers are 4.36×10^5 and 1.0×10^6 , respectively. These Reynolds numbers are sufficiently large that Reynolds number should not be a factor in the radiated noise. But Figures 1.4(a) and 1.4(b) (as well as Figure 1.2) show significant difference in the noise spectra of the jets at high Strouhal number; very similar to those of Figures 1.3(a) and 1.3(b). This casts doubt on the proposition that Reynolds number is really the cause of the discrepancy. We are, at the present time, unable to find a good explanation.

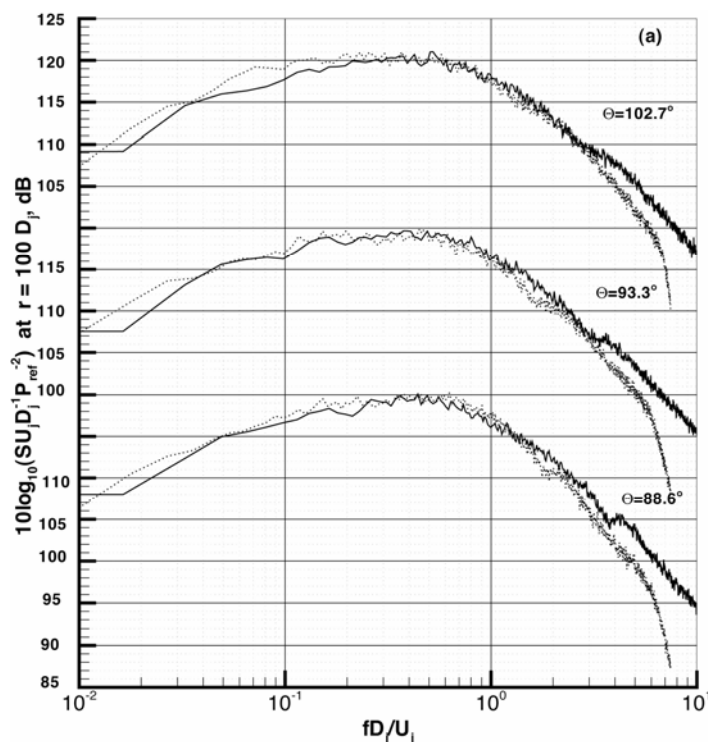


Figure 1.2(a). Scaling of jet noise spectra. Data from Seiner. $M_j = 2.0$, $T_r/T_\infty = 1.8$.
 ——— $D_j = 3.60$ in. (9.14 cm), ······ $D_j = 1.96$ in. (4.98 cm).

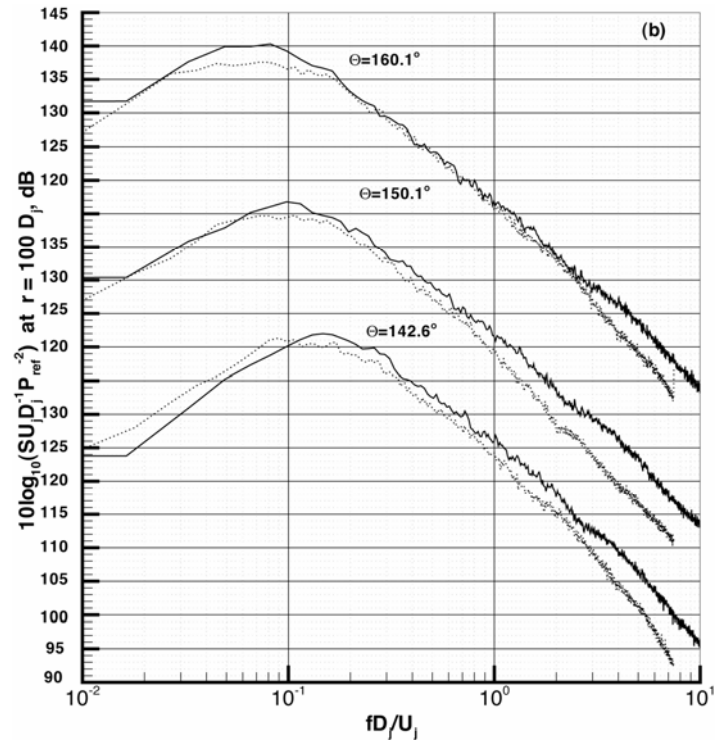


Figure 1.2(b).

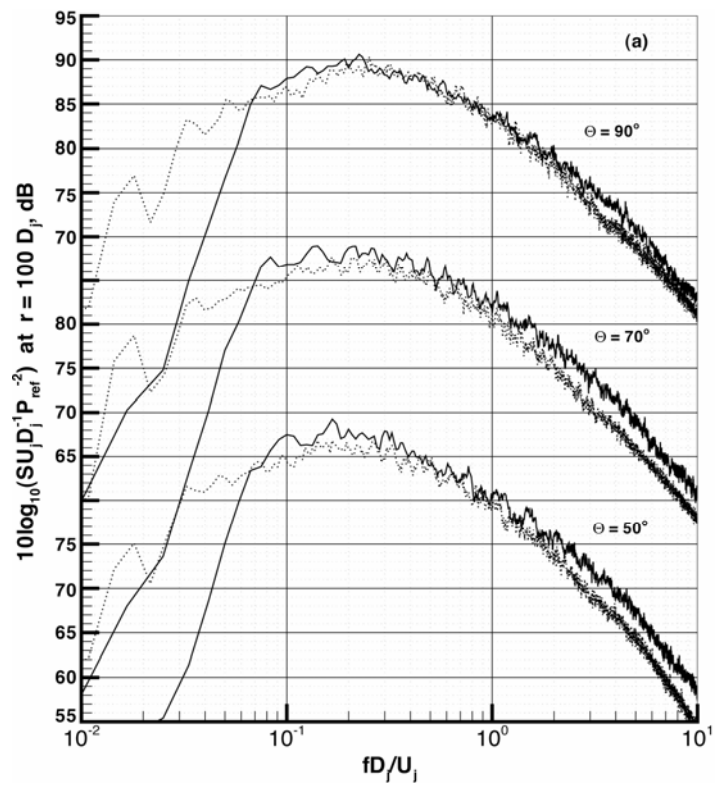


Figure 1.3(a). Scaling of jet noise spectra. Boeing data (Bhat 2001). $M_j = 0.5$, $T_r/T_\infty = 2.15$. — $D_j = 3.46$ in. (8.79 cm), $D_j = 1.5$ in. (3.81 cm).

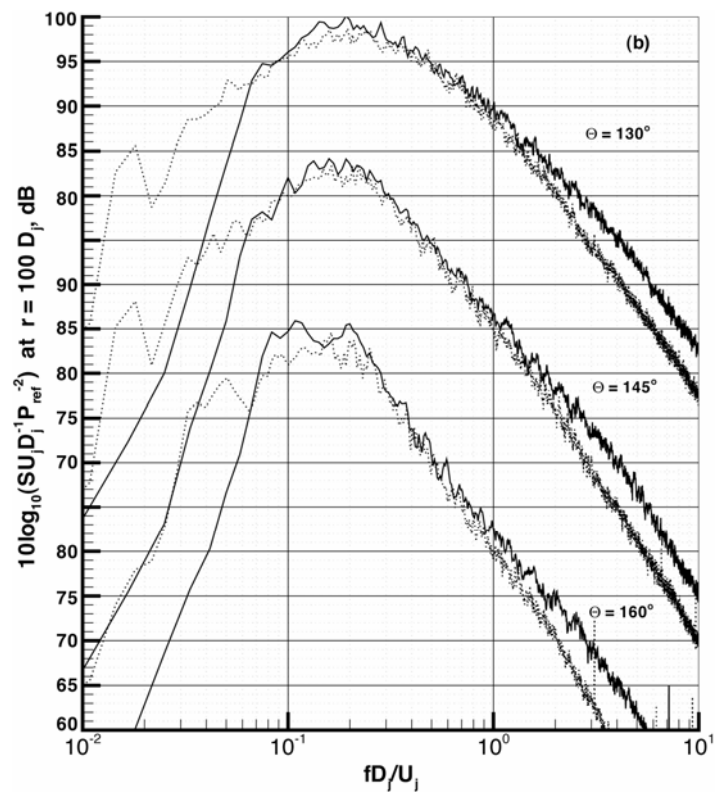


Figure 1.3(b).

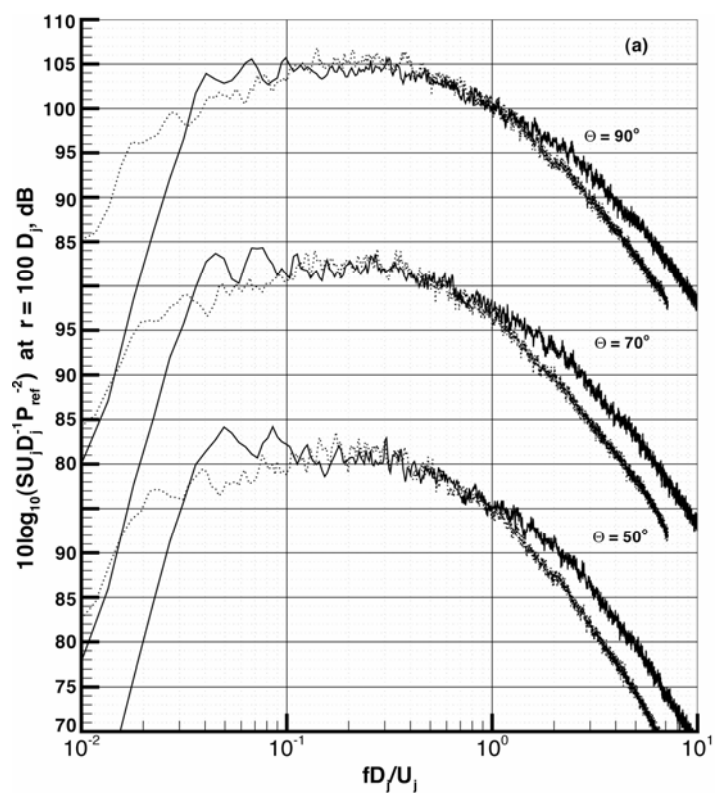


Figure 1.4(a). Scaling of jet noise spectra. Boeing data (Bhat 2001). $M_j = 1.0$, $T_r/T_\infty = 2.15$. ——— $D_j = 3.46 \text{ in. (8.79 cm)}$, ······ $D_j = 1.5 \text{ in. (3.81 cm)}$.

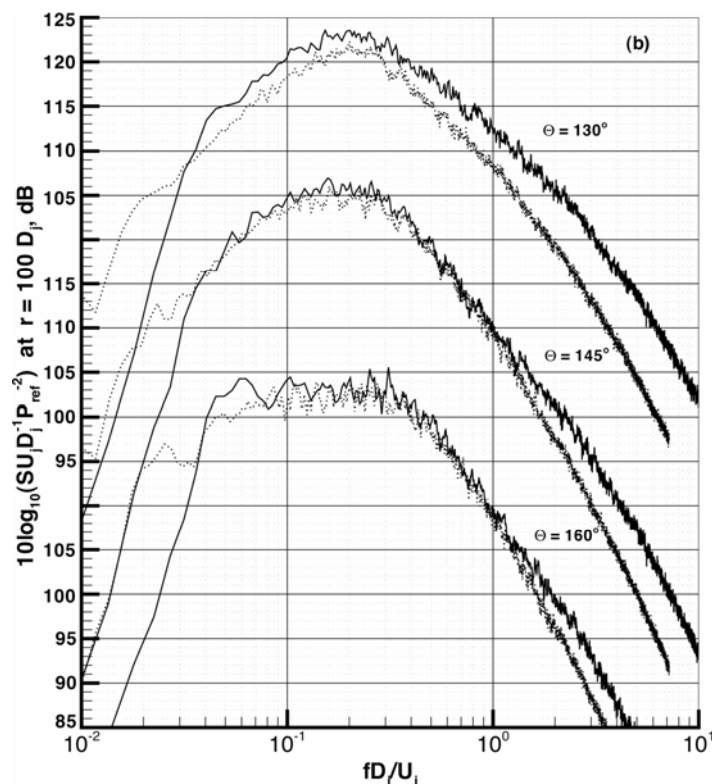


Figure 1.4(b).

Recently, Viswanathan (2002) measured a set of high quality jet noise data over a wide range of Mach numbers and temperature ratios. In his experiment, nozzles of 1.5, 2.45 and 3.46 inches or 3.81, 6.22, and 8.79 cm diameters were used. Here we present a small set of his data using (1.4) as the scaling formula. Figures 5 and 6 are noise spectra at $T_r/T_\infty = 1.8$. Mach 0.6 data are shown in Figure 1.5, whereas Mach 1.0 data are given in Figure 1.6. Figures 1.7 and 1.8 show similar spectra at a much higher temperature ratio of 3.2. It is evident from these figures that the noise spectra from the two larger diameter nozzles do collapse well. There are some differences in the high frequency part of the spectra at low Mach number and low temperature ratio jet operating conditions. The spectra of the 1.5 in. (3.81 cm) diameter jet are consistently lower at high Strouhal number. The fact that the spectra of the two larger nozzles collapse into a nearly single curve suggests that the collapsed spectrum should be very close to the pure jet noise spectrum at the particular jet operating conditions.

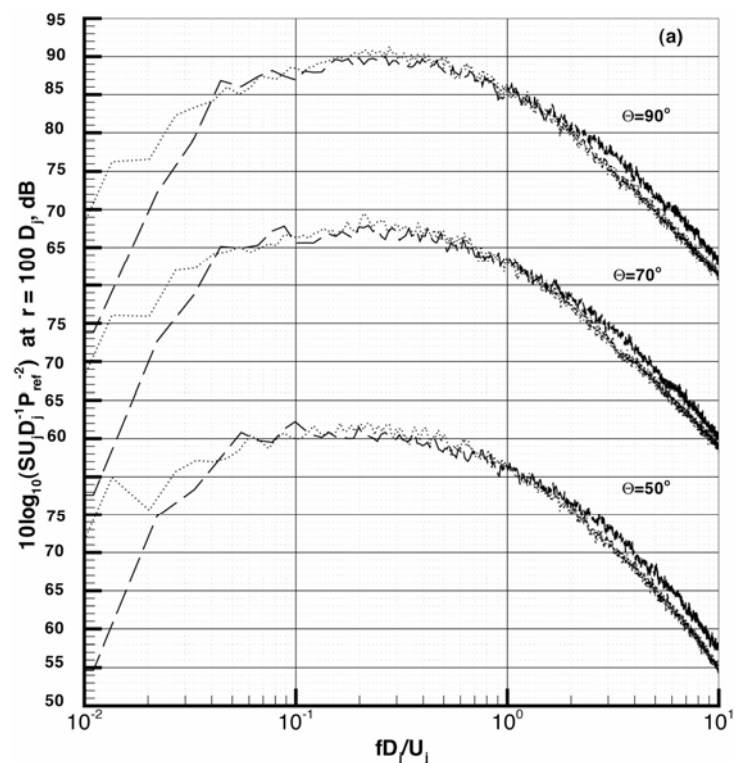


Figure 1.5(a). Scaling of jet noise spectra. Data from Viswanathan (2002). $M_j = 0.6$, $T_j/T_\infty = 1.8$. — $D_j = 2.45$ in. (6.22 cm), \cdots $D_j = 1.5$ in. (3.81 cm).

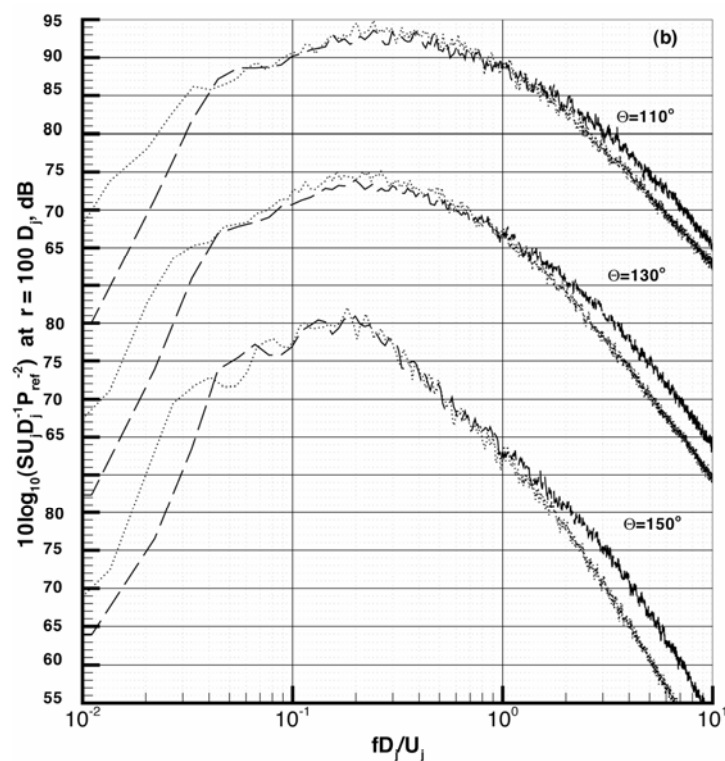


Figure 1.5(b).

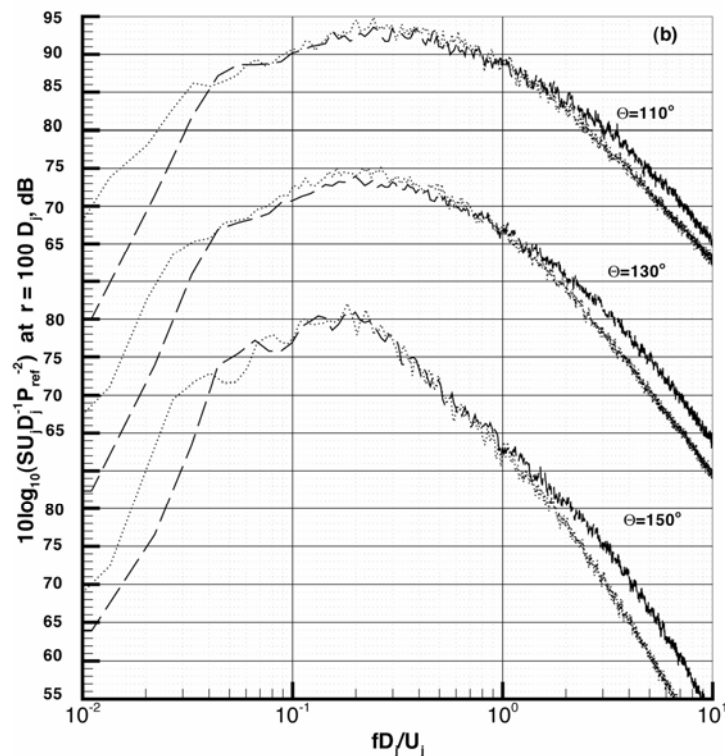


Figure 1.6(a). Scaling of jet noise spectra. Data from Viswanathan (2002). $M_j = 1.0$, $T_j/T_\infty = 1.8$. ——— $D_j = 3.46$ in. (8.79 cm), — — — $D_j = 2.45$ in. (6.22 cm), ······ $D_j = 1.5$ in. (3.81 cm).

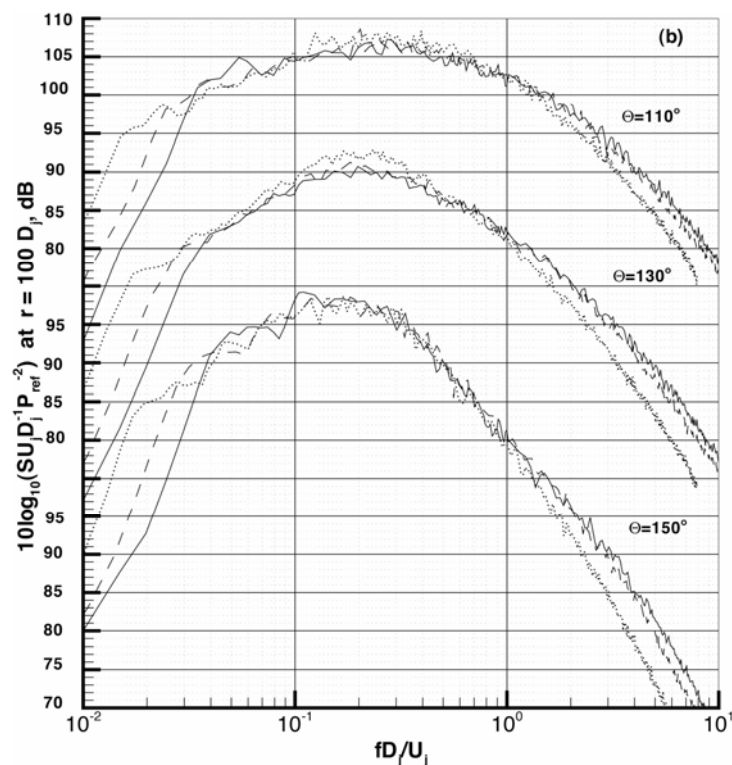


Figure 1.6b.

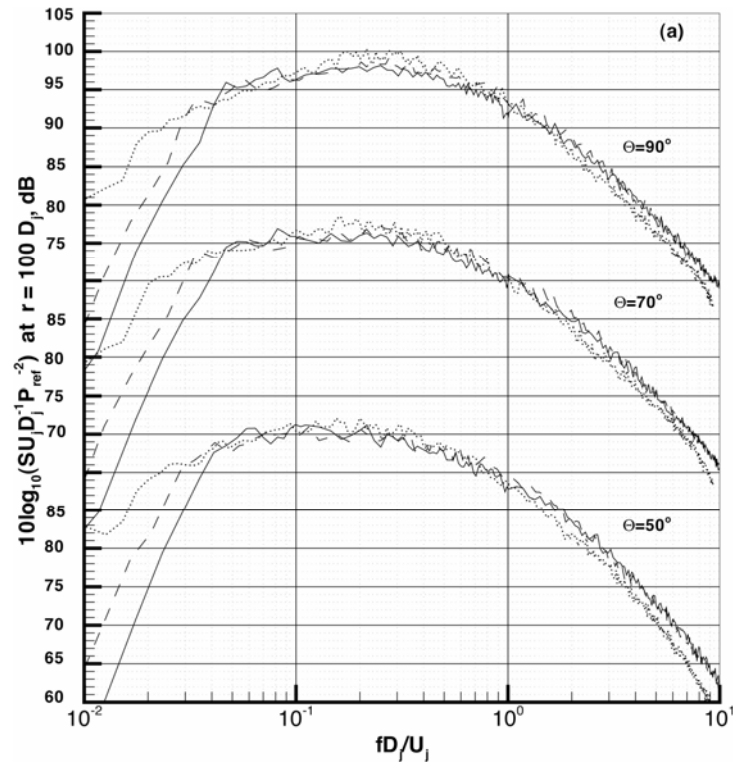


Figure 1.7(a). Scaling of jet noise spectra. Data from Viswanathan (2002). $M_j = 0.6$, $T_j/T_\infty = 3.2$. ——— $D_j = 3.46 \text{ in. (8.79 cm)}$, — — — $D_j = 2.45 \text{ in. (6.22 cm)}$, ······ $D_j = 1.5 \text{ in. (3.81 cm)}$.

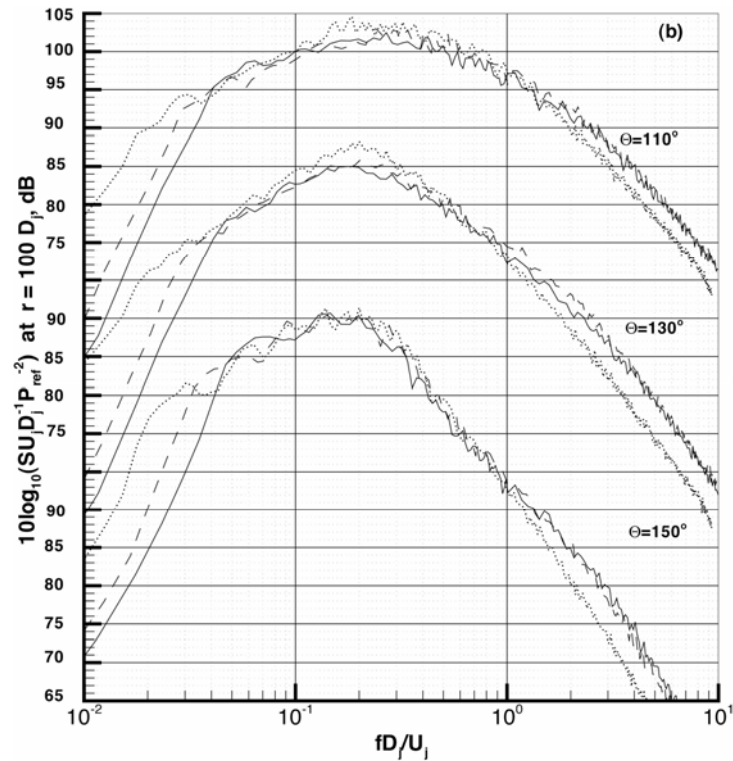


Figure 1.7(b).

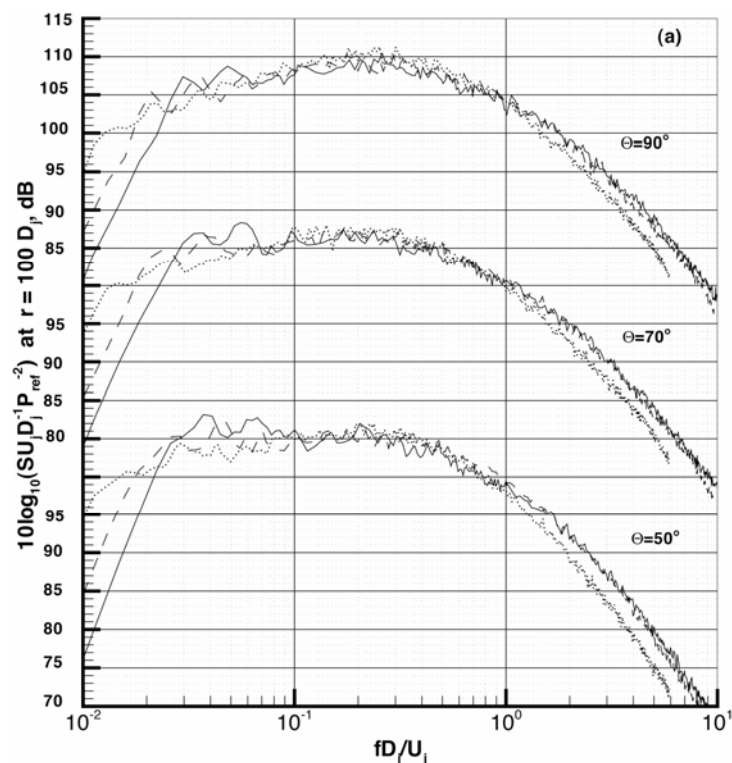


Figure 1.8(a). Scaling of jet noise spectra. Data from Viswanathan (2002). $M_j = 1.0$, $T_j/T_\infty = 3.2$. ——— $D_j = 3.46$ in. (8.79 cm), — — — $D_j = 2.45$ in. (6.22 cm), ······ $D_j = 1.5$ in. (2.81 cm).

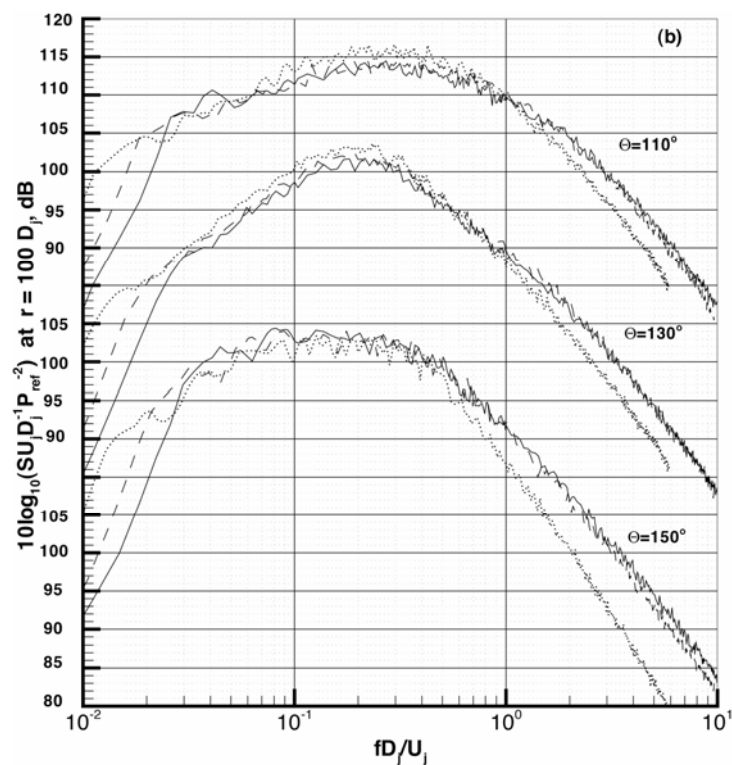


Figure 1.8(b).

Table I
Jet Reynolds number at $T_r/T_\infty = 3.2$

$M_j \setminus D_j$	1.5 inch jet (3.81cm)	2.45 in. (6.22 cm)	3.46 in. (8.79 cm)
0.6	1.4×10^5	2.38×10^5	3.36×10^5
1.0	2.67×10^5	4.50×10^5	6.37×10^5

Table II
Jet Reynolds number at $T_r/T_\infty = 1.8$

$M_j \setminus D_j$	1.5 inch jet (3.81 cm)	2.45 in. (6.22 cm)	3.46 in. (8.79 cm)
0.6	2.70×10^5	4.59×10^5	6.49×10^5
1.0	5.20×10^5	8.80×10^5	1.24×10^6

The reason why the spectra of the smallest jet of Viswanathan's data are consistently low at high Strouhal number is not known. It is not completely a Reynolds number problem. Tables I and II show the Reynolds numbers of these jets. There is no question that, as shown in Table I, the Reynolds number is low at temperature ratio 3.2 for the smallest jets. However, in Table II at temperature ratio 1.8 and Mach 1.0, the Reynolds number of the smallest jet is more than half a million. As yet, Figure 1.6 shows that the noise spectra still have similar discrepancies at high Strouhal number similar to the lower Reynolds number jet. We will not pursue this further here, as it may be a facility problem or even a humidity correction problem. Humidity correction starts to become important at 20 KHz. For the smallest jet, the corresponding Strouhal number lies in the range of 1.3 to 2.7. If there is an over correction, the noise spectra would be lower at Strouhal number higher than the 20 KHz Strouhal number. We, however, have no evidence that this is the case.

1.1.3 Imperfectly Expanded Supersonic Jets

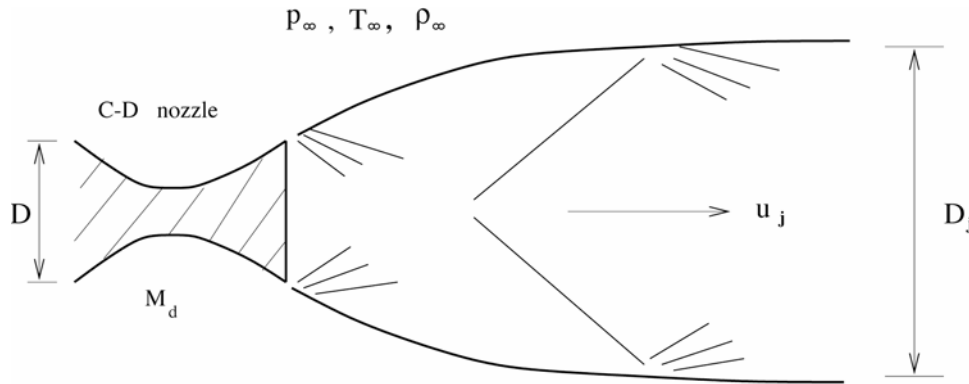


Figure 1.9. Schematic diagram of an underexpanded supersonic jet.

For imperfectly expanded supersonic jets, the pressure at the nozzle exit is not the same as the ambient pressure. Thus the analysis of Section II is not directly applicable to these jets. Let us consider an underexpanded jet from a convergent-divergent (C-D) nozzle as shown in Figure 1.9. By definition the static pressure of the jet at the nozzle exit is higher than the ambient pressure. The gas coming out of the nozzle would, therefore, undergo further expansion. This further expansion leads to an effective (or fully expanded) jet diameter, D_j , larger than the physical diameter, D , of the nozzle exit. A simple relationship between D_j and D can be found by appealing to conservation of mass flux.

Since the gas expands downstream of the nozzle exit, it is, therefore, a reasonably good approximation to assume that the flow through the nozzle as well as in the initial portion of the free jet is isentropic. We will use subscripts r , e and j to denote variables in the reservoir, at the nozzle exit and in the fully developed jet. Conservation of enthalpy leads to,

$$C_p T_r = C_p T_e + \frac{1}{2} U_e^2 = C_p T_j + \frac{1}{2} U_j^2. \quad (1.5)$$

where C_p is the specific heat at constant pressure. Eq. (1.5) may be rewritten as,

$$\frac{T_r}{T_e} = 1 + \frac{\gamma - 1}{2} M_d^2 = \left(\frac{\rho_r}{\rho_e} \right)^{\gamma - 1}. \quad (1.6)$$

$$\frac{T_r}{T_j} = 1 + \frac{\gamma-1}{2} M_j^2 = \left(\frac{\rho_r}{\rho_j} \right)^{\gamma-1}. \quad (1.7)$$

The last equality of (1.6) and (1.7) comes from isentropic relation, $T \propto \rho^{\gamma-1}$. In (1.6) M_d is the design Mach number of the CD nozzle ($M_d = 1.0$ for a convergent nozzle) and is equal to the flow Mach number at the nozzle exit; i.e., $M_d = M_e$. M_j in (1.7) is the fully expanded jet Mach number. The combination of (1.6) and (1.7) yields,

$$\frac{\rho_e}{\rho_j} = \left[\frac{1 + \frac{\gamma-1}{2} M_j^2}{1 + \frac{\gamma-1}{2} M_d^2} \right]^{\frac{1}{\gamma-1}} \quad (1.8)$$

and

$$\frac{T_j}{T_e} = \left[\frac{1 + \frac{\gamma-1}{2} M_d^2}{1 + \frac{\gamma-1}{2} M_j^2} \right]. \quad (1.9)$$

By conservation of mass flux, we have

$$\rho_e U_e D^2 = \rho_j U_j D_j^2. \quad (1.10)$$

Thus, by using (1.5), (1.8) to (1.10), we find

$$\frac{D_j}{D} = \left(\frac{\rho_e}{\rho_j} \right)^{\frac{1}{2}} \left(\frac{U_e}{U_j} \right)^{\frac{1}{2}} = \left[\frac{1 + \frac{\gamma-1}{2} M_j^2}{1 + \frac{\gamma-1}{2} M_d^2} \right]^{\frac{1}{2(\gamma-1)}} \left(\frac{M_d}{M_j} \right)^{\frac{1}{2}} \left(\frac{T_e}{T_j} \right)^{\frac{1}{4}} = \left(\frac{M_d}{M_j} \right)^{\frac{1}{2}} \left[\frac{1 + \frac{\gamma-1}{2} M_j^2}{1 + \frac{\gamma-1}{2} M_d^2} \right]^{\frac{\gamma+1}{4(\gamma-1)}}. \quad (1.11)$$

Formula (1.11) was first stated in the work of Tam and Tanna (1982) but without a detailed derivation.

We want to point out that for an overexpanded jet, the jet fluid will encounter shocks immediately downstream of the nozzle exit. However, for moderately overexpanded jets, the shocks are relatively weak. The change in entropy across the weak shocks of these jets is of

higher order in the jump in Mach number. The flow, therefore, does not deviate badly from isentropic flow. For this reason, (1.11) may still be useful for estimating the fully developed jet diameter of moderately overexpanded jets.

Shock containing jets usually emit screech tones (Tam, 1995) driven by a feedback phenomenon. For strongly screeching jets, the flow dynamics are substantially changed by the feedback. Here we consider jets that have only mild screech tones.

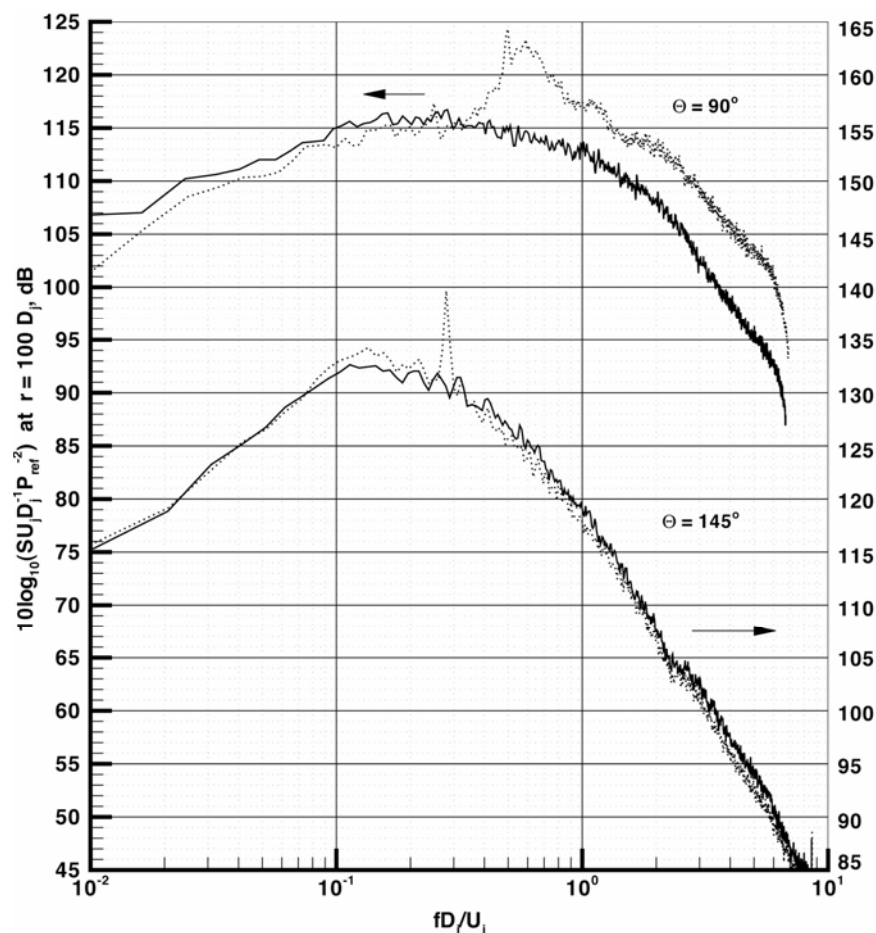


Figure 1.10. Scaling of perfectly and imperfectly expanded supersonic jet noise spectra. $M_j = 1.5$. — $M_d = 1.5$, $D = 1.68$ in.(4.27 cm), ····· $M_d = 1.0$, $D = 1.56$ in.(3.96 cm) $T_r/T_\infty = 2.23$ for inlet angle 90° , $T_r/T_\infty = 1.45$ for inlet angle 145° .

Now as far as jet mixing noise is concerned, D_j , given by (1.11) is the pertinent length scale. Thus the results obtained by dimensional analysis before would apply to even imperfectly expanded supersonic jets if D_j instead of D is used in the scaling formula (1.3). To demonstrate the applicability of scaling formula (1.3) with this modification, we will show that the turbulent

mixing noise of an underexpanded jet can be scaled to that of a perfectly expanded jet by means of (1.3). Figure 1.10 shows two sets of jet noise spectra measured by Seiner (see Tam *et al.* 1996) at fully expanded Mach number 1.5. One set of spectra is from a jet issued from a convergent nozzle ($M_d = 1.0$). The other set is from a nearly perfectly expanded jet ($M_d = 1.5$). As can be seen by using the fully expanded jet diameter D_j provided by (1.11), there is a good collapse of the data. The underexpanded jet has additional broadband shock associated noise at high Strouhal number at $\Theta = 90^\circ$ but not at $\Theta = 145^\circ$. Figure 1.11 shows similar data scaling for Mach 2 jets. In this case, D_j is much larger than D for underexpanded jets. The spectra collapse well using D_j of (1.11) as the length scale. The data level will differ by several dB if D is used instead.

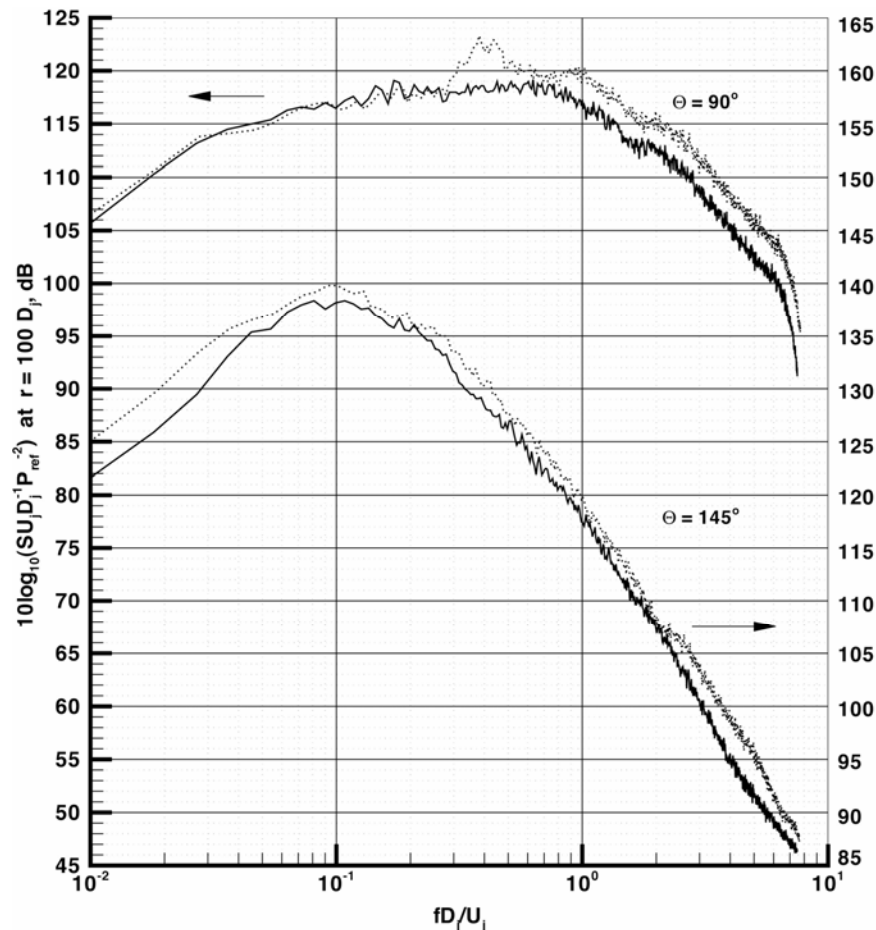


Figure 1.11. Scaling of perfectly and imperfectly expanded supersonic jet noise spectra. $M_j = 2.0$ $T_r/T_\infty = 1.8$. — $M_d = 2.0$, $D = 1.96 \text{ in. (4.99 cm)}$, $M_d = 1.0$, $D = 1.56 \text{ in. (3.96 cm)}$

1.2 Power Law

It has been known since the early days of jet noise research that the noise intensity varies as a high power of the jet velocity. This power law has the support of both theory and experiment. The most celebrated power law is the Lighthill U^8 law. Numerous experiments have been performed for the purposes of verifying the U^8 law. Some measurements indicate that the exponent is close to but not precisely equal to 8. A more general power law is sometimes written in the form,

$$I \propto U_j^n. \quad (1.12)$$

In a recent experiment, Viswanathan (2002) confirmed that jet noise intensity could, indeed, be correlated by a power law of the form (1.12). He found that n depends on jet temperature. It varied from 7.98 to 8.74.

A power law in the form of (1.12) is dimensionally unsatisfactory. In this section, our goal is to express the power law in a dimensionless form and then examine the dependence of its parameters on the dimensionless groups of the input variables.

Let us define the noise intensity (or OASPL, overall sound pressure level), I , for noise radiation in the far field direction θ as,

$$I = \int_0^\infty S(r, \theta, f) df. \quad (1.13)$$

Note: noise intensity defined by (1.13) differs from the traditional definition by a factor of $\rho_\infty a_\infty$. In (1.13) S is the spectral density. Now (1.13) may be rewritten in a dimensionless form as,

$$\frac{I}{p_\infty^2} = \int_0^\infty \frac{S\left(\frac{r}{D_j}, \theta, \frac{fD_j}{U_j}, \frac{U_j}{a_\infty}, \frac{T_r}{T_\infty}\right) U_j}{p_\infty^2 D_j} d\left(\frac{fD_j}{U_j}\right). \quad (1.14)$$

On replacing the integrand by (1.3), (1.14) becomes,

$$\frac{I}{p_\infty^2} = \int_0^\infty \frac{F\left(\frac{U_j}{a_\infty}, \frac{T_r}{T_\infty}, \frac{fD_j}{U_j}, \theta\right)}{\left(\frac{r}{D_j}\right)^2} d\left(\frac{fD_j}{U_j}\right) = \frac{K\left(\frac{U_j}{a_\infty}, \frac{T_r}{T_\infty}, \theta\right)}{\left(\frac{r}{D_j}\right)^2}. \quad (1.15)$$

Experimental observations suggest that the function K may be expressed as a high power of (U_j/a_∞) . That is,

$$\frac{I(r, \theta)}{p_\infty^2} \cong \frac{A \left(\frac{U_j}{a_\infty} \right)^n}{\left(\frac{r}{D_j} \right)^2} \quad (1.16)$$

where A and n are two free parameters of the power law. They depend on the temperature ratio and the direction of radiation; i.e., $A = A(T_r/T_\infty, \theta)$, $n = n(T_r/T_\infty, \theta)$.

The validity of power law in the form of (1.16) can be confirmed experimentally. Figure 1.12 shows a log–log plot of I/p_∞^2 at $r/D = 100.0$ as a function of U_j/a_∞ for jet noise radiated in the 90° direction based on the data of Viswanathan (2002) and Seiner (see Tam *et al.* 1996)). Each of the data sets is for a fixed temperature ratio. The arrow marks the value -80.0 in the vertical axis of Figure 1.12 for the particular curve. It is clear that, to a good degree of approximation, a linear relationship exists in the log–log plot. This validates a power law relationship as given in (1.16). Figure 1.13 shows a similar plot for noise radiated in the 150° inlet angle direction. Again a linear relationship between I/p_∞^2 and U_j/a_∞ exists at each temperature ratio. In addition to the data shown in Figures 1.12 and 1.13, we would like to report that we have examined data at other angles (from 50° to 150°). All of them can be correlated by a power law. We believe this provides strong empirical support for the general validity of (1.16).

The exponent n of power law (1.16), which is the slope of the straight lines in Figures 1.12 and 1.13, varies slightly with jet temperature ratio and the direction of radiation. The same is true with the coefficient A . Figure 1.14 gives the dependence of n on temperature ratio (T_r/T_∞) at a number of directions of radiation. Generally speaking, n is large for larger inlet angle. Its value decreases with increase in temperature ratio. Numerically, n varies from 5.3 to 9.9 and $n = 8$ may be considered an overall averaged value.

The dependence of coefficient A of power law (1.16) on jet temperature ratio is given in Figure 1.15. Just as for exponent n , the value of A is larger for larger inlet angle. Also its value decreases nearly monotonically with increase in temperature ratio.

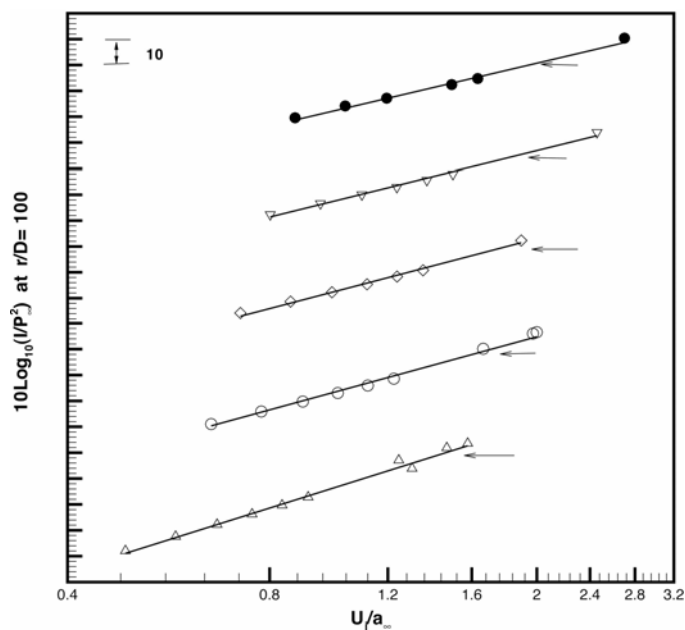


Figure 1.12. Dependence of noise intensity on jet Mach number based on ambient speed of sound. Inlet angle 90° . \leftarrow vertical axis equals to -80.0 for the curve. \bullet , ∇ , \diamond , \circ , \triangle ; $T_r/T_\infty = 1.0, 1.8, 2.2, 2.7, 3.2$. — Power law $A (U_j/a_\infty)^n/(r/D)^2$. Data from Viswanathan (2002) and Seiner (see Tam *et al.*, 1996).

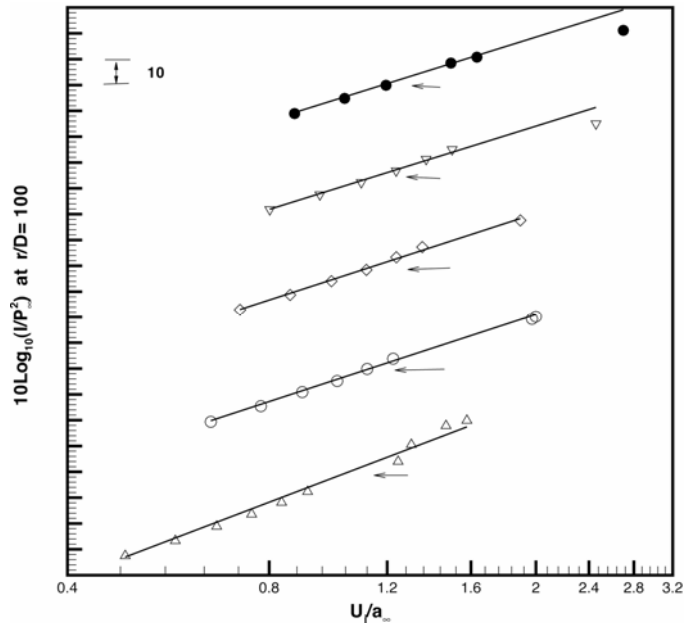


Figure 1.13. Dependence of noise intensity on jet Mach number based on ambient speed of sound. Inlet angle 150° . \leftarrow vertical axis equals to -80.0 for the curve. \bullet , ∇ , \diamond , \circ , \triangle ; $T_r/T_\infty = 1.0, 1.8, 2.2, 2.7, 3.2$. — Power law $A (U_j/a_\infty)^n/(r/D)^2$. Data from Viswanathan (2002) and Seiner (see Tam *et al.*, 1996).

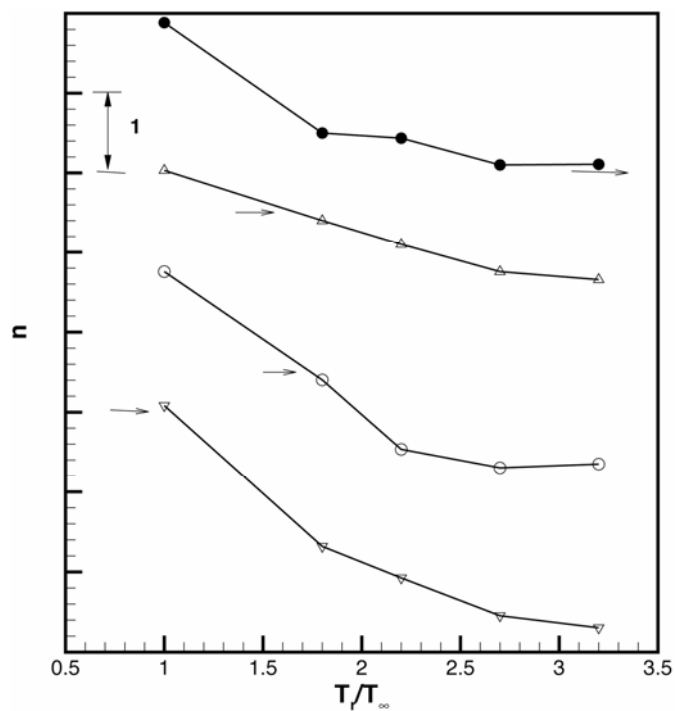


Figure 1.14. Variation of power law exponent with jet temperature ratio. ∇ , \circ , \triangle , \bullet ; inlet angle = 50°, 80°, 120°, 150°. Data from Viswanathan and Seiner.

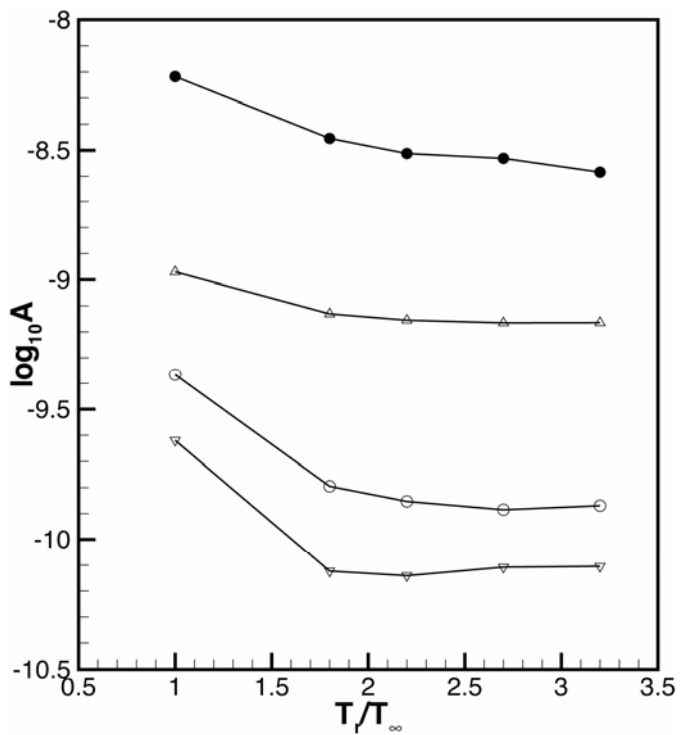


Figure 1.15. Variation of power law proportionality constant with jet temperature ratio. ∇ , \circ , \triangle , \bullet ; inlet angle = 50°, 80°, 120°, 150°. Data from Viswanathan and Seiner.

It is interesting to point out that, as shown in Figures 1.14 and 1.15, n and A decrease monotonically as temperature ratio, T_r/T_∞ , increases. However, both n and A cannot become zero. Thus, it is reasonable to expect that, as temperature ratio becomes sufficiently large, n and A would each independently reach an asymptotic value. Figures 1.14 and 1.15 suggest that at the last data point ($T_r/T_\infty = 3.2$) both curves for n and A are close to their asymptotes. We will call this the “hot-jet” limit. The physical significance of the hot-jet limit is that for jets at high temperature ratio, the noise intensity depends only on jet velocity ratio. Temperature plays no role in jet noise intensity except through its influence on the nozzle exit velocity. This is an unexpected result. Of course, it would require further investigation before one can determine what the hot-jet limit means to the distribution of jet noise sources in the jet plume and on the jet mixing processes.

1.3 The Principal Components of Supersonic Jet Noise

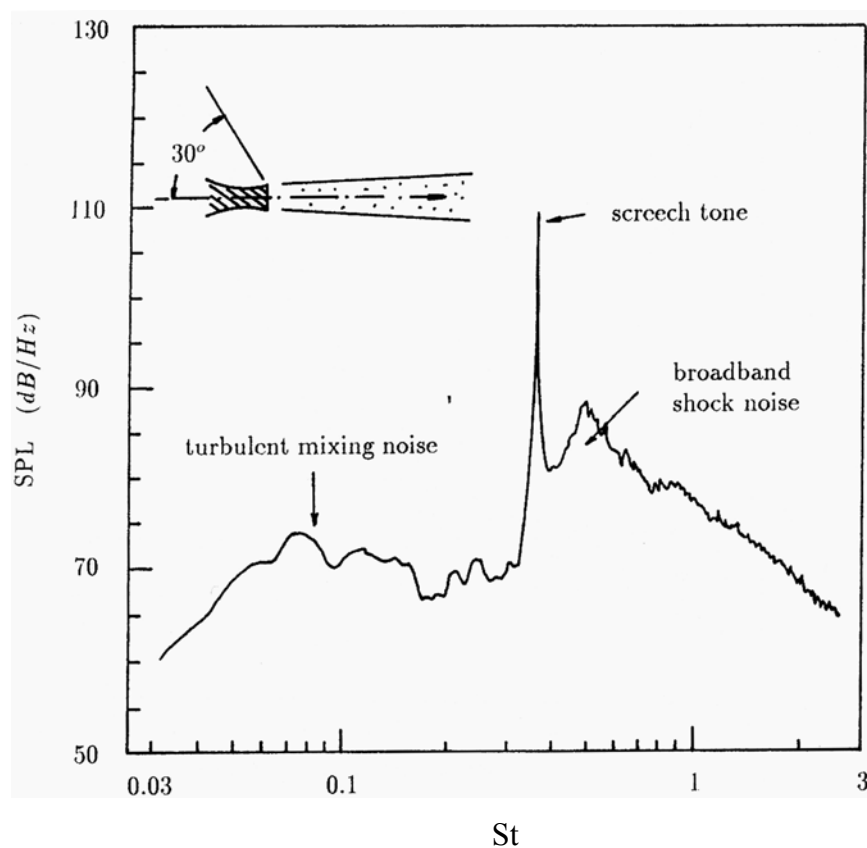


Figure 1.16. Typical far field narrow band supersonic jet noise spectrum (Seiner 1984). Microphone at 30 degrees to nozzle inlet direction.

Except for jets operating at perfectly expanded conditions, the noise of a supersonic jet comprises three basic components. They are the turbulent mixing noise, the broadband shock associated noise and the screech tones. Figure 1.16 shows a typical narrow band noise spectrum of an imperfectly expanded supersonic jet measured by Seiner (1984). Very prominent in this figure is the discrete frequency component or the screech tone at the center of the figure. The appearance of a screech tone is usually accompanied by its harmonics. Sometimes, even the fourth or fifth harmonic can be detected. The low frequency broadband peak of Figure 1.16, to the left of the screech tone, is the turbulence mixing noise component. The high frequency peak, to the right of the fundamental screech frequency, is the broadband shock associated noise. The relative intensity of the three noise components is a strong function of the direction of observation. In the downstream direction of the jet, turbulent mixing noise is the most dominant noise component. In the upstream direction, the broadband shock associated noise is more intense. For circular jets, the screech tones radiate primarily in the upstream direction.

1.3.1 Characteristics of Turbulent Mixing Noise

High quality turbulent mixing noise data in narrowband from nearly perfectly expanded supersonic jets can be found in the literature. Seiner *et al.* (1992) performed very detailed narrow band noise measurements of a Mach 2 jet. The total temperature of the jet varied from 313K to as high as 1534K. Figure 1.17 shows typical noise directivities at a few of the important Strouhal numbers (Strouhal number = fD/U_j , where f , D and U_j are the frequency, nozzle exit diameter and the fully expanded jet velocity, respectively). It is clear from this figure and all the other data that the dominant part of the turbulent mixing noise is radiated into an angular sector of about 45 degrees measured from the jet flow direction or greater than 135 degrees inlet angle. Within this dominant noise sector, the noise spectrum is dominated by a single broadband peak. The peak occurs at a Strouhal number of around 0.1 to 0.25 depending on the jet temperature and Mach number. Outside the dominant noise radiation sector, the noise directivity and spectral characteristics are very different. In the upstream direction, the noise intensity is low and is nearly uniform in direction as shown in Figure 1.17. Furthermore, the noise spectrum is very flat over a large range of Strouhal number. This is the background noise, which is believed to be generated by the fine scale turbulence of the jet flow. The dominant part of the noise, on the other hand, is believed to be generated directly by the large turbulence structures of the jet flow.

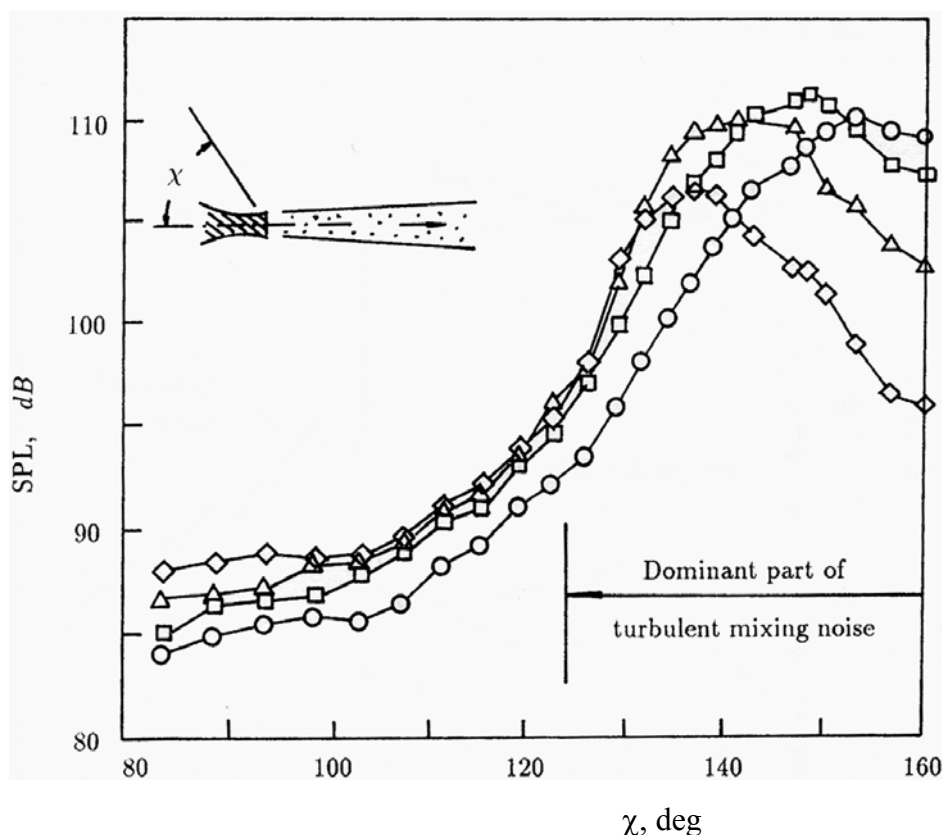


Figure 1.17. Measured noise directivities (Seiner *et al.*, 1992) at selected Strouhal numbers (St) of a Mach 2 jet at total temperature of 500K. \circ $St = 0.067$; \square $St = 0.12$; \triangle $St = 0.20$; \diamond $St = 0.40$.

The intensity as well as the directional and spectral characteristics of the turbulent mixing noise of supersonic jets depends on the jet Mach number and jet to ambient temperature ratio. As jet Mach number increases, the difference in peak noise levels between the dominant part and the background noise increases. However, at a fixed Mach number and Strouhal number, the maximum level of noise radiation does not significantly increase with large increase in jet temperature. The main effect of higher jet temperature is the broadening of the dominant noise sector.

1.3.2 Characteristics of Broadband Shock Associated Noise

When a supersonic jet is operating at an imperfectly expanded condition, regardless of whether the jet is underexpanded or overexpanded, a shock cell structure will form in the jet plume. In the presence of the shock cells, the jet emits additional broadband noise called the

broadband shock associated noise. Broadband shock associated noise was first identified by Harper-Bourne & Fisher (1974). Since then, it has been the subject of a number of experimental investigations; e.g., Tanna (1977), Seiner & Norum (1979, 1980), Seiner & Yu (1982), Norum & Seiner (1982a,b) and Yamamoto *et al.* (1984). These experiments have provided much detailed information on the characteristics of broadband shock associated noise.

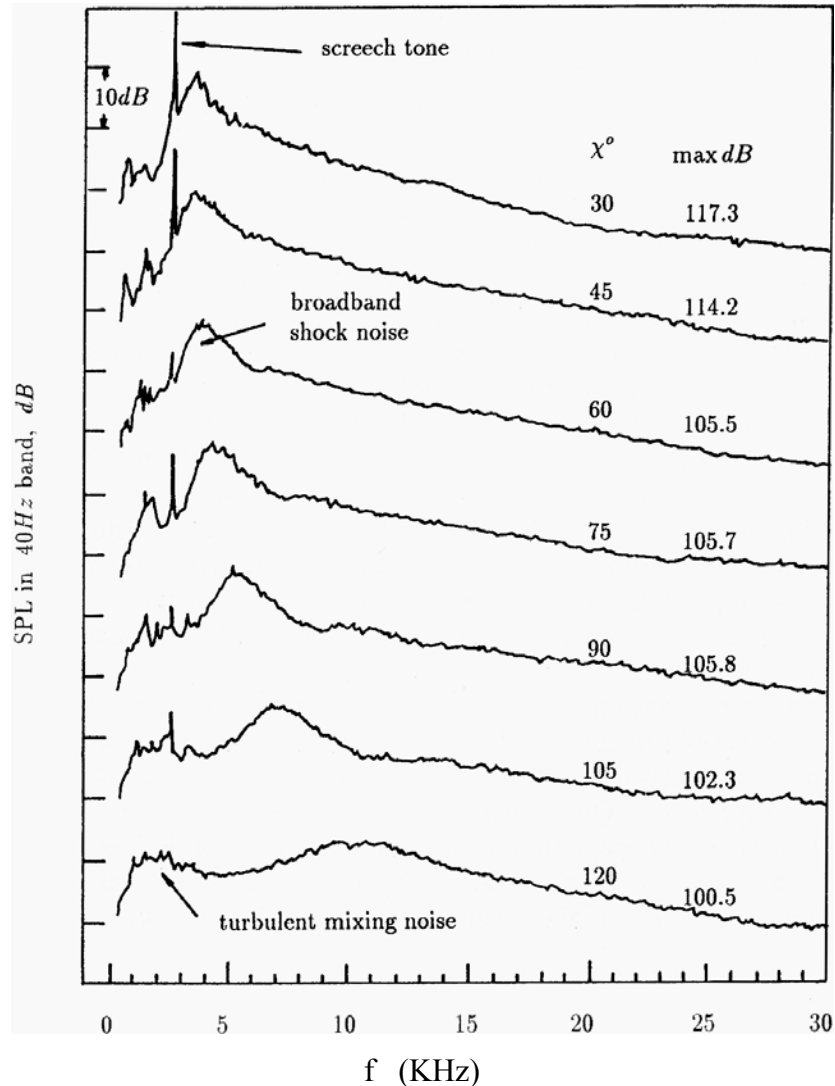


Figure 1.18. Narrow band noise spectra of a Mach 1.67 jet from a *C-D* nozzle with design Mach number 1.5. χ^0 = nozzle inlet angle (Norum & Seiner 1982a).

Figure 1.18 shows typical noise spectra of an imperfectly expanded jet measured by a microphone array at equal distance to the jet nozzle exit at 15° intervals. The maximum intensity of each spectrum is indicated in the figure. The jet emitted a screech tone at a frequency of 3.6KHz. The screech tone can be seen in almost all the spectra. The turbulent mixing noise

contributes to the broadband peak to the left of the screech frequency. The very distinct peak to the right of the screech tone is the broadband shock associated noise. Clearly, this is the dominant noise component in the upstream direction. Several distinct characteristics of broadband shock associated noise can be identified in this figure. First, the frequency corresponding to the peak of the spectrum changes with the direction of radiation. It increases with increasing χ^0 , the inlet angle. Second, each spectrum is made up of several peaks. A second and a third peak can readily be identified in the $\chi^0 = 90$ degree spectrum. Third, the half-width of the spectral peak increases with χ^0 . Thus at large χ^0 the spectral peak is very broad. One very unexpected characteristic is that at a fixed jet Mach number, the maximum noise level at the spectral peak is unaffected by jet temperature. The frequency at which the peak level occurs is, however, shifted to a higher value as jet temperature increases.

1.3.3 Characteristics of Screech Tones

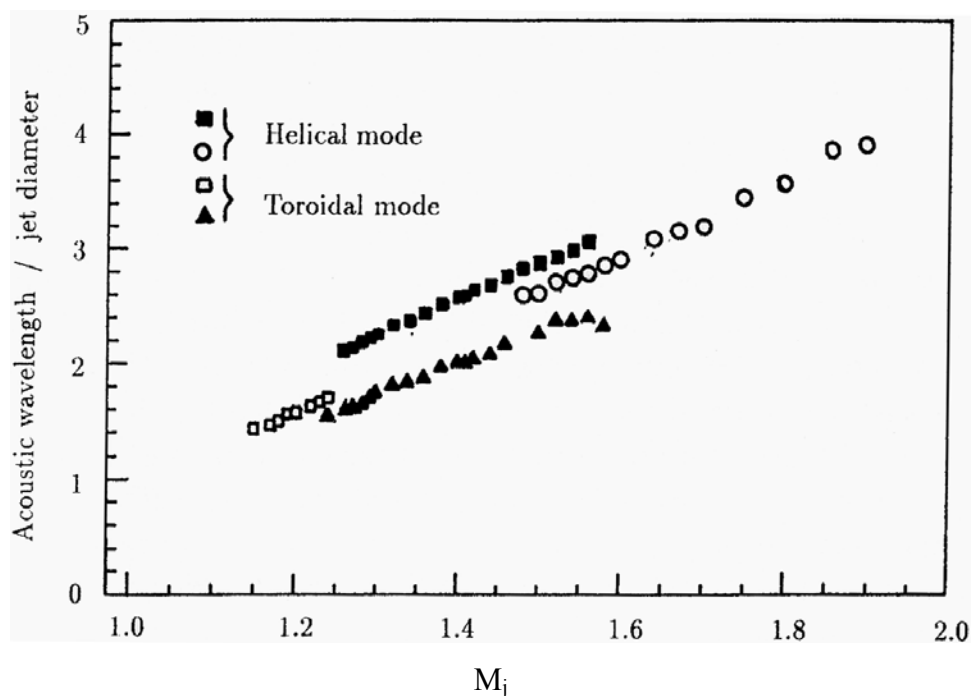


Figure 1.19. Screech modes of axisymmetric supersonic jet from a *C-D* nozzle with design Mach number 1.41 (Seiner *et al.* 1987).

Screech tones from supersonic jets were first observed by Powell (1953a,b). Since then the phenomenon has been studied experimentally by a host of investigators; e.g., Davies & Oldfield (1962), Sherman *et al.* (1976), Westley & Wooley (1969, 1970, 1975), Rosfjord & Toms (1975),

Norum (1983), Seiner *et al.* (1987), Massey *et al.* (1994) and more recently Panda (1998), Panda, Seasholtz (1999), Panda, Raman & Zaman (2003). It is found that the fundamental screech tone radiates primarily in the upstream direction whereas the principal direction of radiation of the second harmonic is at 90 degrees to the jet flow direction (Norum, 1983). When a jet emits strong screech tones the jet flow undergoes strong oscillations. Observations reveal that two types of jet motion could occur. They are the toroidal mode and the helical/flapping mode oscillations. (Note: the superposition of an equal number of left and right helical mode oscillations creates a flapping mode.) With the toroidal mode oscillations, both the jet flow and the acoustic field exhibit axisymmetry. With the flapping mode, the jet oscillates up and down around a flapping plane. The flapping plane may not necessarily be stationary. A slow precession of the flapping plane has been observed.

Figure 1.19 shows the variation of the acoustic wavelength of the screech tones of a supersonic jet issued from a Mach 1.41 convergent-divergent nozzle (Seiner *et al.* 1987) as a function of jet Mach number. Four modes of screech, two toroidal modes and two helical/flapping modes, were observed. At certain jet Mach numbers, the jet emits more than one screech tone (not harmonic of each other). The dominant screech tone mode changes with jet Mach number. This mode switching phenomenon is clearly shown in Figure 1.19. At low Mach number, the screech tones are associated with the toroidal mode. As Mach number increases, there is a switch over to the flapping/helical mode.

The intensities of screech tones are affected by the jet Mach number, the jet temperature, the nozzle lip thickness and the presence of sound reflecting surfaces in the immediate environment of the jet. It is well-known that the intensity of screech tones decreases with increase in jet temperature. This is especially true for low supersonic Mach number jets (see Massey *et al.* 1994). Perhaps because of this, engine designers, generally, have not regarded screech tones as a potential cause of sonic fatigue to jet engines. A thick nozzle lip can act as a good sound reflecting surface. Norum (1983) found that the screech intensity can increase substantially simply by using a thicker lip nozzle. The tone directivity is, however, not altered.

1.4 Turbulent Mixing Noise

There is now a growing acceptance that turbulent mixing noise of high-speed jets consists of two components. They are the noise from the fine scale turbulence and the large turbulence

structures of the jet flow. Laufer *et al.* (1976) used a spherical reflector to measure the noise source along the length of supersonic jets at Mach 1.47, 1.97 and 2.47. They found that the noise source strength distributions of these jets radiating to the maximum noise direction (around 30° to 45° exhaust angles) and to the sideline at 90 degrees were distinctly different. Real time pressure signal measured by an omni directional microphone indicated that the sound radiated to those two directions were also distinctly different. The pressure signal at 90 degrees resembled that of subsonic jets being random but smooth. On the other hand, for the two high Mach number jets, the pressure signal at 37.5 and 45 degrees had shock-like spikes with steep rise time. These distinctive differences, together with the difference in source locations, led Laufer *et al.* to conclude that there were two intrinsically different noise sources. The noise radiated by the two sources had distinctively different directional, spectral and real time characteristics.

Independently, Tam (1995), Tam and Chen (1993), based on the observation of a strong directivity of the radiated sound in the low exhaust angle directions (within a cone of 50 degrees around the jet flow direction) and an almost flat directivity for sound radiating upstream and to the sideline (see Figure 1.17), together with theoretical reasoning of possible noise generation mechanisms, proposed that the dominant part of the noise radiated downstream was from the large turbulence structures while the sideline noise was from the fine scale turbulence of the jet flow. During the last few years, experimental supports are found validating the two mixing noise concepts.

1.4.1 Noise Generation Mechanisms

The fine scale turbulence in a jet flow is quite isotropic. The random turbulent motion creates an effective pressure analogous to the pressure created by the random molecular motion of a gas. The random fluctuating pressure is the source of fine scale turbulence noise. Just as in a gas, the turbulence pressure is quite isotropic. As a result, the radiated sound has a nearly uniform directivity. The directivity is, however, modified by the downstream convection of the fine scale turbulence by the jet mean flow. This convection effect causes more sound to radiate in the direction of motion. In addition, the sound generated by a lump of fine scale turbulence has to traverse the jet mixing layer before radiating to the far field. Because the jet mean flow is non-uniform, the acoustic rays are bent due to refraction. This reduces the intensity of sound radiated downstream.

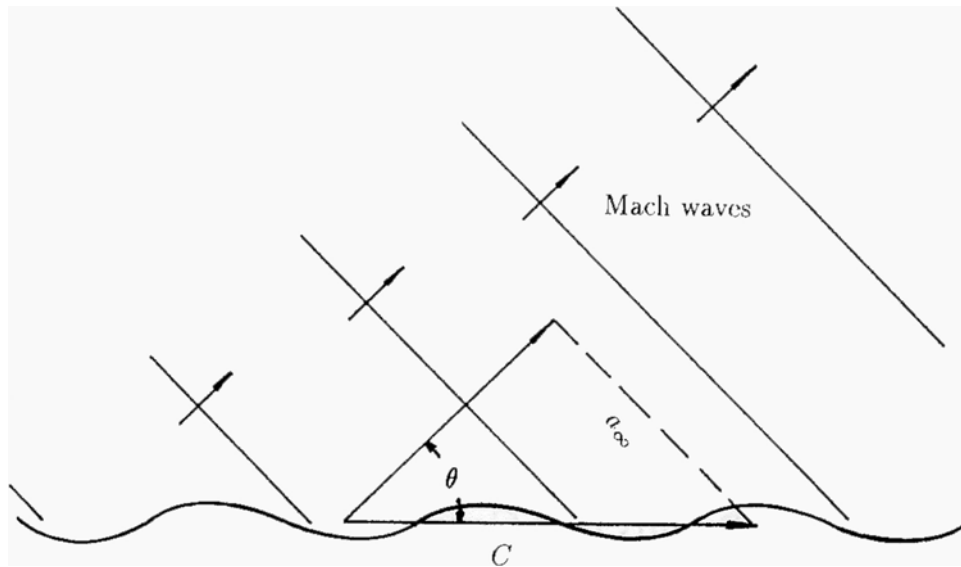


Figure 1.20. Schematic diagram showing Mach wave radiation generated by a wavy surface traveling at supersonic phase velocity.

Let us now examine how sound is generated by the large turbulence structures of supersonic jets. The large turbulence structures may be regarded as a superposition of a spectrum of instability waves of the jet flow. The two are statistically equivalent. Consider an instability wave of a certain azimuthal mode at a given frequency propagating down a jet column. An approximate picture of the physical problem is to regard the instability wave as a wavy wall. The wavy wall has the same wavelength and wave speed as the instability wave. In the case of the wavy wall, it is well-known that if the propagation speed is supersonic relative to the ambient sound speed, intense noise radiation in the form of Mach waves would result as illustrated in Figure 1.20. The wavy wall analogy suggests that the direction of the most intense noise radiation from a supersonic jet can be estimated by using the Mach angle relation based on the speed of the most amplified instability wave of the jet. Further, the Strouhal number at the peak of the radiated noise spectrum must be the same as the Strouhal number of the most amplified instability wave. Tam *et al.* (1992) investigated these relationships and found good experimental confirmation.

Tam & Burton (1984) pointed out that the wavy wall analogy must be modified to account for the growth and decay of the instability wave as it propagated downstream. Near the nozzle exit, the mixing layer of the jet is thin. The large velocity gradient across the shear layer causes the instability wave to have very large growth rate. As the instability wave propagates

downstream the shear layer thickness increases leading to a reduction in mean velocity gradient and hence the growth rate. Eventually at some point downstream the wave becomes damped. Its amplitude decreases as it continues to propagate until it becomes vanishingly small. The growth and decay of the wave amplitude is important to the noise radiation process. For a fixed frequency wave of constant amplitude, the wave spectrum is discrete. With a single wavenumber there is only a single wave speed so that the Mach waves are radiated in a single direction. The growth and decay of the instability wave amplitude lead to a broadband wavenumber spectrum. This results in Mach wave radiation over large angular directions. Furthermore, a single frequency subsonic wave of constant amplitude would not radiate sound according to the Mach wave radiation mechanism. However, with growth and decay of the wave amplitude, a part of the broadband wavenumber spectrum could have supersonic phase velocity. These supersonic phase disturbances will lead to noise radiation.

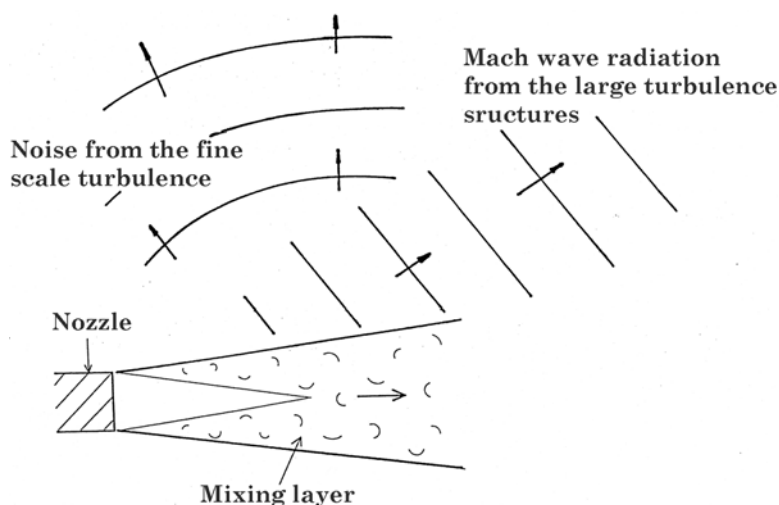


Figure 1.21. Schematic diagram of the directivity of Mach wave radiation and that of the fine scale turbulence.

The Mach wave radiation mechanism discussed above relies on the existence of supersonic phase (relative to ambient sound speed) components. For highly supersonic jets, especially at high temperature, this is an extremely efficient noise generation process. But if the jet speed is subsonic, the efficiency is greatly reduced. Thus for low subsonic jets, the large turbulence structures of the jet flow may not be the most important noise generators. The fine scale turbulence probably is the more dominant source.

Figure 1.21 is a schematic diagram showing the radiation of the two mixing noise components from a high speed jet. Within the Mach cone in the downstream direction, the large turbulence structures' noise is dominant. In the upstream and sideline directions, there is little Mach wave radiation. The dominant noise is from the fine scale turbulence.

1.4.2 Experimental Evidence in Support of Two Turbulent Mixing Noise Components

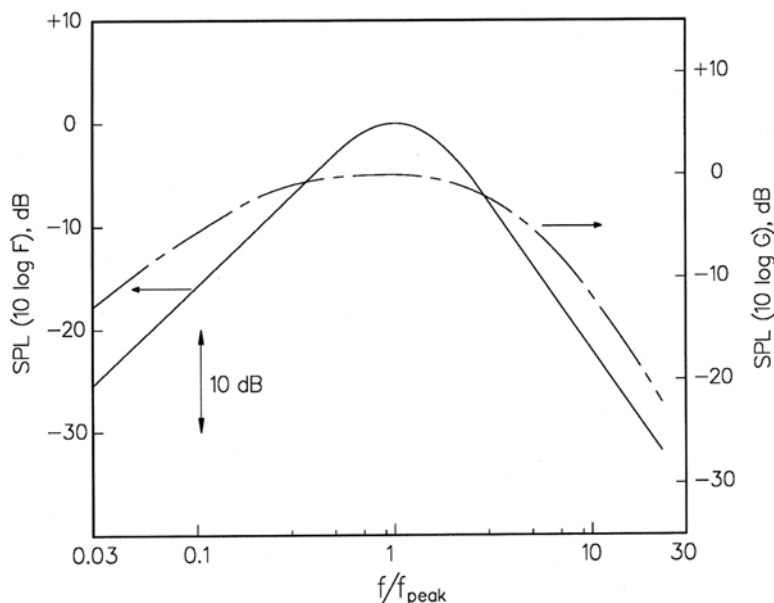


Figure 1.22. Similarity spectra for the two components of turbulent mixing noise. ——— large turbulence structures/instability waves noise; — - — fine scale turbulence noise.

Other than the early work of Laufer *et al.* (1976), an important set of experimental evidence in support of the existence of two turbulent mixing noise components in high speed jets was offered by Tam, Golebiowski and Seiner (1996). They analyzed a very large set of jet noise data from the Jet Noise Laboratory of the NASA Langley Research Center. They reasoned that jet flow and turbulence were known to exhibit self-similarity. It was, therefore, possible that jet noise spectra also possessed similarity characteristics. They identified empirically two similarity spectra that seemingly were capable of fitting all noise spectra in all directions of radiation. The two spectra $F(f/f_{\text{peak}})$ and $G(f/f_{\text{peak}})$ are shown in Figure 1.22. The f_{peak} is the frequency at the spectrum peak. The F -spectrum is the spectrum of the large turbulence structures noise. It fits all jet noise spectra radiated within the Mach cone centered at the jet flow direction when the peak

of the spectrum is aligned with that of the data. This is true regardless of the direction of radiation, the jet Mach number and temperature ratio of the jet. This is demonstrated in Figure 1.23. In this figure, four spectra from two different Mach numbers at several different temperature ratios and directions of radiation are shown to have the same shape as the F -spectrum.

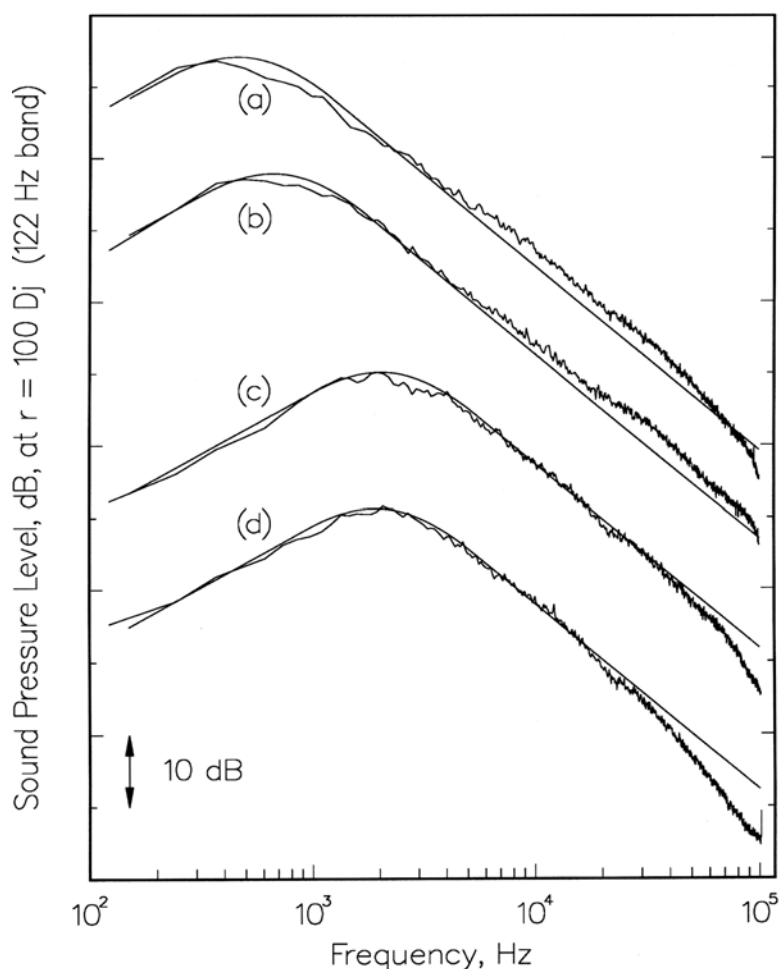


Figure 1.23. Comparison of the similarity spectrum of large turbulence structures/instability waves noise and measurements: (a) $M_j = 2.0$, $T_r/T_\infty = 4.89$, $\chi = 160.1^\circ$, $\text{SPL}_{\text{max}} = 124.7$ dB; (b) $M_j = 2.0$, $T_r/T_\infty = 1.12$, $\chi = 160.1^\circ$, $\text{SPL}_{\text{max}} = 121.6$ dB; (c) $M_j = 1.96$, $T_r/T_\infty = 1.78$, $\chi = 136.6^\circ$, $\text{SPL}_{\text{max}} = 121.0$ dB; (d) $M_j = 1.49$, $T_r/T_\infty = 1.11$, $\chi = 138.6^\circ$, $\text{SPL}_{\text{max}} = 106.5$ dB.

The G -spectrum is the spectrum of the fine scale turbulence noise. It fits all high-speed jet noise spectra radiated to the sideline and upstream directions. That it does fit the measured

spectra regardless of direction, jet Mach number and temperature ratio can be seen in Figure 1.24. There is excellent agreement between the G -spectrum and the measured data. In the transition direction of radiation at which both the large and small scale turbulence noise are important, it is necessary to use a combination of the F and G spectra to fit the measured data. This is illustrated in Figure 1.25.

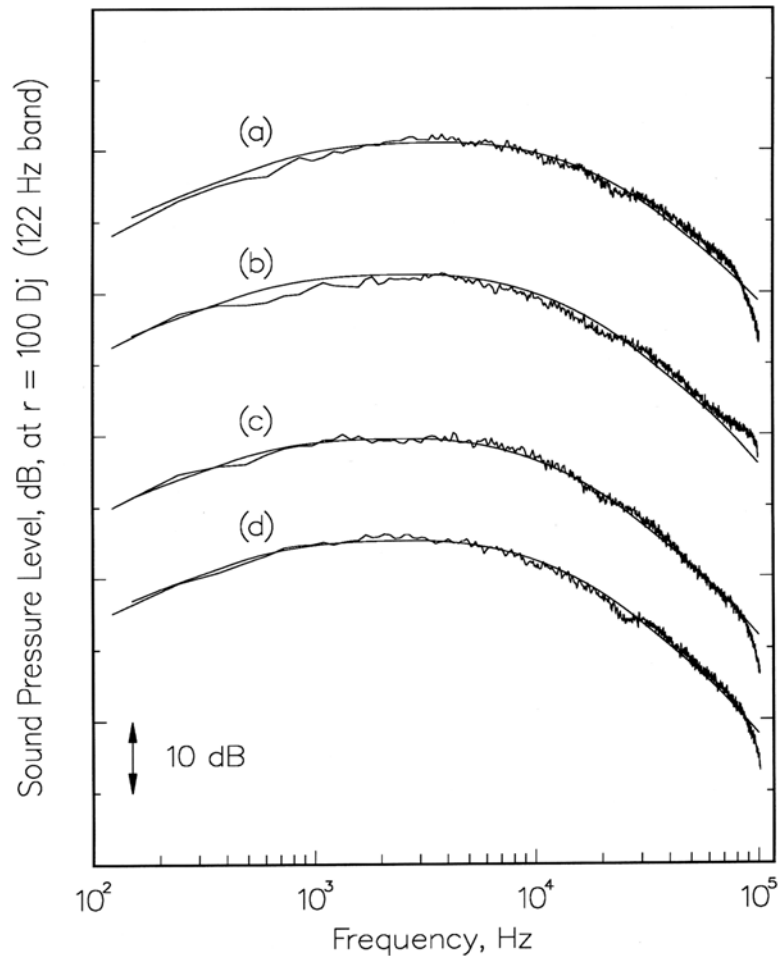


Figure 1.24. Comparison of the similarity spectrum of large turbulence structures/instability waves noise and measurements: (a) $M_j = 1.49$, $T_r/T_\infty = 2.35$, $\chi = 92.9^\circ$, $\text{SPL}_{\text{max}} = 96.0$ dB; (b) $M_j = 2.0$, $T_r/T_\infty = 4.89$, $\chi = 83.8^\circ$, $\text{SPL}_{\text{max}} = 107.0$ dB; (c) $M_j = 1.96$, $T_r/T_\infty = 0.99$, $\chi = 83.3^\circ$, $\text{SPL}_{\text{max}} = 95.0$ dB; (d) $M_j = 1.96$, $T_r/T_\infty = 0.98$, $\chi = 120.2^\circ$, $\text{SPL}_{\text{max}} = 100.0$ dB.

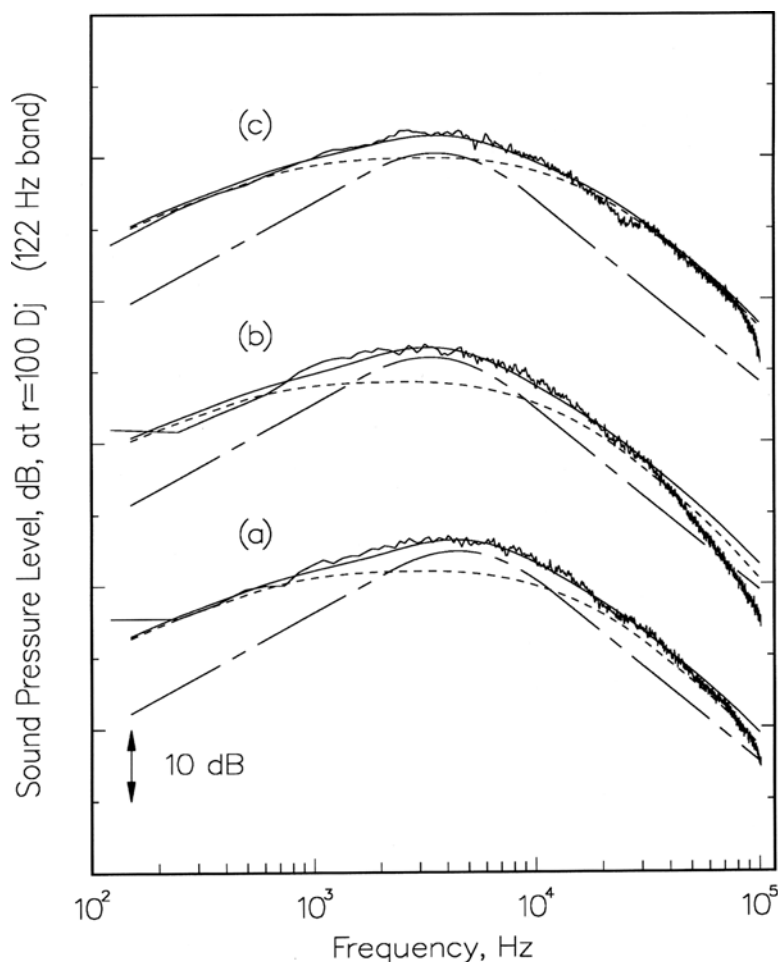


Figure 1.25. Comparison of the sum of the similarity spectrum of both large and fine scale turbulence and measurements at intermediate direction of radiation. — — — large turbulence structures noise; - - - fine scale turbulence noise; ——— total: (a) $M_j = 2.0$, $T_r/T_\infty = 4.89$, $\chi = 160.1^\circ$, $SPL_{\max} = 124.7$ dB; (b) $M_j = 2.0$, $T_r/T_\infty = 1.12$, $\chi = 160.1^\circ$, $SPL_{\max} = 121.6$ dB; (c) $M_j = 1.96$, $T_r/T_\infty = 1.78$, $\chi = 136.6^\circ$, $SPL_{\max} = 121.0$ dB

Aside from the NASA Langley Research Center data, Tam (1998) examined the noise spectra of supersonic jets issuing from simple elliptic, rectangular and plug nozzles and found that their spectra also conformed to the similarity spectra. Tam and Zaman (2000) analyzed the noise spectra of cold subsonic jets from nonaxisymmetric and tabbed nozzles. They discovered that the spectral shapes from these jets had the same shape as the similarity spectra. Dahl and Papamoschou (2000) reported that the spectra from supersonic coaxial jets could also be represented by the two similarity spectra. Most recently, Viswanathan (2000, 2004)

demonstrated convincingly that these two spectra also were good fits to the measured spectra of hot subsonic and supersonic jets over a fairly large range of jet operating conditions.

Since the 1960's there have been many attempts to measure directly the sources of jet mixing noise. The use of hot wire and similar instruments led to flow interference and has doomed many early efforts. Recently, Panda *et al.* (2003) succeeded in measuring the density and velocity fluctuations inside a jet by means of Rayleigh scattering. By means of this technique, they were able to measure two-point space-time correlations between the turbulent fluctuations at a point inside the jet flow and the acoustic pressure measured by a far field microphone. They found that when the microphone was at 90 degrees to the jet flow direction, there was very little correlation. However, when the microphone was moved to a lower exhaust angle, e.g., 30 to 40 degrees, there was significant correlation. This set of correlation data is in full agreement with the existence of two noise sources, the large and fine scale turbulence. The fine scale turbulence is random and spatially uncorrelated. Each source occupies a small volume producing a small amount of sound. Since a far field microphone receives noise from all sources, the correlation of its pressure signal with the motion of a blob of fine scale turbulence would be statistically insignificant. This is the case of noise radiating to the sideline. The situation is totally different for a microphone located at, say, 30° from the jet exhaust direction. The noise in this direction is generated by the large turbulence structures of the jet. In other words, the noise source is spatially coherent over a large volume of the jet flow. The fluctuations at a point are a good representation of the fluctuations of the entire coherent source. Thus, it is no mystery that there is strong correlation of the single source point fluctuations with far field sound.

1.4.3 Prediction of Fine Scale Turbulence Noise from High-Speed Jets

An accurate prediction theory for fine scale turbulence noise from high-speed jets has recently been developed by Tam and Auriault (1999). The Tam and Auriault theory is semi-empirical. This is so because the turbulence input to the theory is not from first principle. There is no first principle turbulence theory at this time. In their theory, the source of noise is the random fluctuations of the turbulent kinetic energy of fine scale turbulence. The turbulence intensity, turbulence length and time scales are given by the $k - \varepsilon$ turbulence model. The level of empiricism of the theory is at about the same level as the $k - \varepsilon$ model.

The original Tam and Auriault theory was developed for cold to moderate temperature jets. It was found that for hot jets, the standard $k - \varepsilon$ turbulence model is inadequate. Tam and Ganesan (2004) proposed a modification to the $k - \varepsilon$ model to include the effect of density gradient arising from non-uniform to temperature distribution. This improvement of the $k - \varepsilon$ model allows Tam, Pastouchenko and Viswanathan (2005) to extend the Tam and Auriault theory to very high temperature jets. Let \mathbf{x} denote the location of a far field microphone. With respect to a spherical polar coordinate system centered at the nozzle exit with the polar axis pointing in the direction of flow, \mathbf{x} has the coordinates (R, Θ, ϕ) where R is the radial distance, and Θ and ϕ are the polar and azimuthal angle. The radiated noise spectral density is given by,

$$S(\mathbf{x}, \omega) = \frac{4\pi^3}{(\ln 2)^{\frac{3}{2}}} \int \int \int_{V_{\text{jet}}} \frac{\Gamma\left(\nu + \frac{1}{2}\right)}{\Gamma(\nu)} \left(\frac{\hat{q}_s^2}{c^2}\right) \frac{1}{\tau_s} \frac{|p_a(\mathbf{x}_2, \mathbf{x}, \omega)|^2 e^{-\frac{\omega^2 \ell_s^2}{\bar{\mu}^2 4(\ln 2)}}}{\left[1 + \omega^2 \tau_s^2 \left(1 - \frac{\bar{u}}{a_\infty} \cos \Theta\right)^2\right]^{\nu + \frac{1}{2}}} d\mathbf{x}_2 \quad (1.17)$$

where V_{jet} is the volume of the jet plume. In (1.17), $\Gamma(\nu)$ is the Gamma function; $\hat{q}_s = \frac{2}{3} \bar{\rho} k_s$, k_s is the intensity of the kinetic energy of fine scale turbulence per unit volume; ℓ_s and τ_s are the corresponding length and time scales; ω is the angular frequency; and $p_a(\mathbf{x}_2, \mathbf{x}, \omega)$ is the adjoint Green's function that accounts for the impedance and refraction effects of the jet flow. The term c is an empirical constant. The spectral density $S(\mathbf{x}, \omega)$ is per unit angular frequency ω . On converting to decibel per Strouhal number (fD_j/u_j) based on fully expanded jet velocity, u_j , and diameter, D_j , the spectral density of the sound field at (R, Θ, ϕ) is

$$S\left(R, \Theta, \phi, \frac{fD_j}{u_j}\right) = 10 \log \left[\frac{4\pi S(\mathbf{x}, \omega)}{p_{\text{ref}}^2 \left(\frac{D_j}{u_j}\right)} \right] \quad (1.18)$$

where p_{ref} is the reference pressure of the decibel scale. It is to be noted that, for $\nu = \frac{1}{2}$, (1.17) and (1.18) reduced to the spectral density formulas of Tam and Auriault.

The noise spectrum formula (1.17) contains four parameters, namely, \hat{q}_s^2/c^2 , ℓ_s , τ_s and ν . For cold to moderate temperature jets, explicit dependence of these parameters on the $k - \varepsilon$ turbulence model is given in Tam and Auriault. For hot axisymmetric jets, the density gradient parameter is $(1/\rho)(d\rho/dr)$. By assuming that the density parameter is small, its first order effect may then be represented by a perturbation term. That is, it may be represented by an additional term that is linear in $(1/\rho)(d\rho/dr)$. On balancing the dimensions using k and ε (k and ε are the only two parameters available in the $k - \varepsilon$ model for dimensional adjustment), Tam *et al.* (2005) proposed the use of the following formulas,

$$\nu = \frac{1}{2} + \begin{cases} c_\eta \frac{k^{3/2}}{\varepsilon} \frac{1}{\rho} \left| \frac{d\rho}{dr} \right| & (1.19(a)) \\ 0 & (1.19(b)) \end{cases}$$

$$\frac{\hat{q}_s^2}{c^2} = A^2 q^2 + \begin{cases} B \frac{k^{3/2}}{\varepsilon} \frac{1}{\rho} \left| \frac{d\rho}{dr} \right| q^2 ; q = \frac{2}{3} \bar{\rho} k & (1.20(a)) \\ 0 & (1.20(b)) \end{cases}$$

$$l_s = c_l \frac{k^{3/2}}{\varepsilon} + \begin{cases} c_{l\rho} \frac{k^3}{\varepsilon^2} \frac{1}{\rho} \left| \frac{d\rho}{dr} \right| & (1.21(a)) \\ 0 & (1.21(b)) \end{cases}$$

$$\tau_s = c_\tau \frac{k}{\varepsilon} + \begin{cases} c_{\tau\rho} \frac{k^{5/2}}{\varepsilon^2} \frac{1}{\rho} \left| \frac{d\rho}{dr} \right| & (1.22(a)) \\ 0 & (1.22(b)) \end{cases}$$

In (1.19) to (1.22) the (a) formulas are to be used when $d\bar{u}/dr$ and $d\rho/dr$ have opposite signs. The (b) formulas are to be used when they have the same sign. The reason for this is due to the effect of density difference on the Kelvin-Helmholtz instability in the shear layer of the jet. Tam and Ganesan (2004) have pointed out that enhanced mixing arising from density effect occurs only when the lighter fluid is moving. The values of k and ε in these formulas are found by the extended $k - \varepsilon$ turbulence model in the mean flow computation.

For nonaxisymmetric jets, (1.19) to (1.22) may be generalized by replacing $|d\rho/dr|$ by $|(\nabla \bar{u}) \cdot (\nabla \rho)| / |\nabla \bar{u}|$ and that density gradient correction is incorporated only if $(\nabla \bar{u}) \cdot (\nabla \rho)$ is negative. Here $\nabla \bar{u}$ is taken as the reference direction as far as density gradient effect is concerned.

(14) to (17) contained four unknown constants. They are c_η , B , $c_{l\rho}$ and $c_{t\rho}$. The recommended values of these constants are,

$$\begin{aligned} A &= 0.755, & c_l &= 0.256, & c_\tau &= 0.233 \\ c_\eta &= 2.1599, & B &= 0.806, & & \\ c_{l\rho} &= -0.026, & c_{t\rho} &= -0.2527 & & \end{aligned}$$

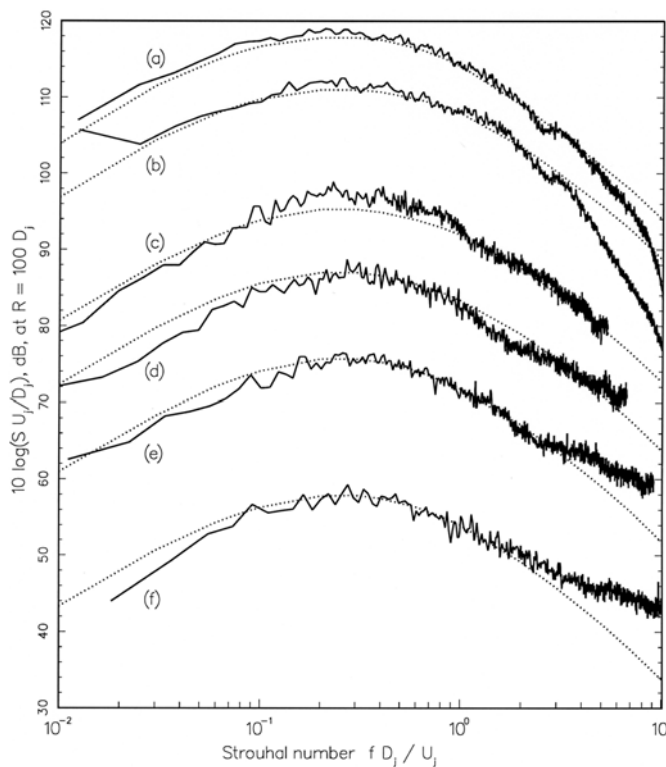


Figure 1.26(a). Cold jet noise spectra at $\Theta = 60^\circ$, $T_r/T_\infty = 1.0$. (a) $M_j = 2.0$, (b) $M_j = 1.49$, (c) $M_j = 0.9$, (d) $M_j = 0.7$, (e) $M_j = 0.5$, (f) $M_j = 0.3$. — experiments, Seiner (in Tam, Golebiowski & Seiner, 1996) and Norum & Brown (1993); \cdots (1.17).

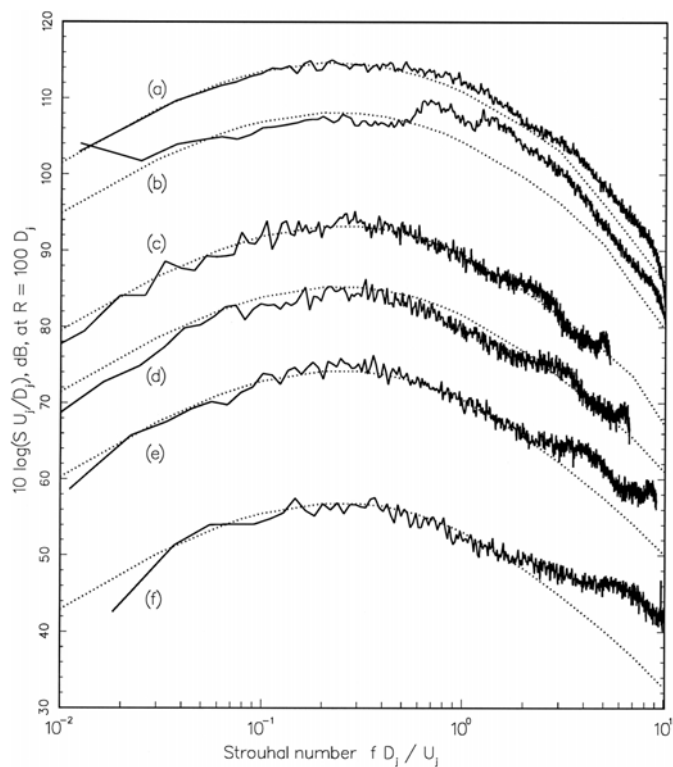


Figure 1.26(b). Cold jet noise spectra at $\Theta = 90^\circ$, $T_r/T_\infty = 1.0$. — experiments, \cdots (1.17)

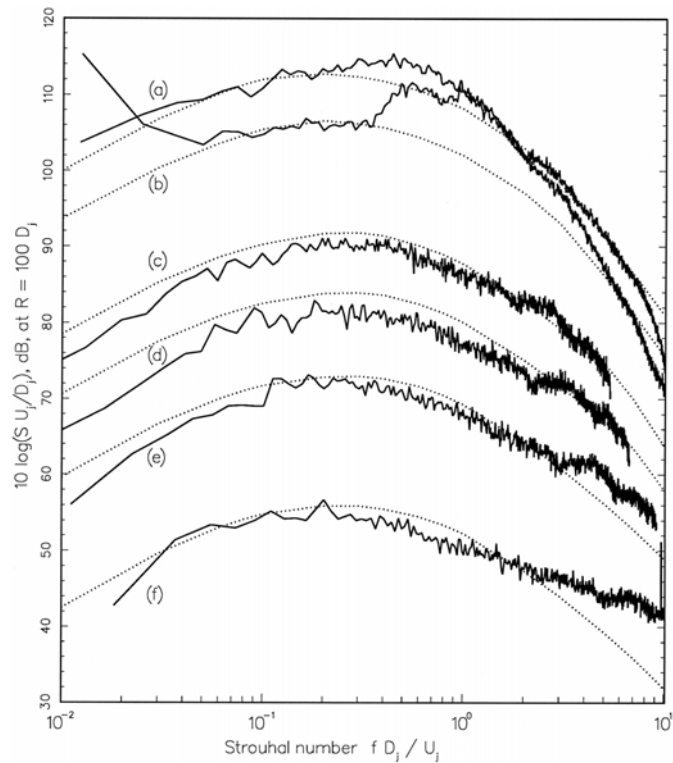


Figure 1.26(c). Cold jet noise spectra at $\Theta = 120^\circ$, $T_r/T_\infty = 1.0$. — experiments, \cdots (1.17).

Figure 1.26 shows comparisons of the computed fine scale turbulence noise spectra by Tam and Auriault (1999) and the experimental data of Seiner (see Tam, Golebiowski and Seiner, 1996) and Norum and Brown (1993). Figures 1.26(a), 1.26(b) and 1.26(c) show the noise spectra at 60° , 90° and 120° for cold jets with Mach number ranging from 0.3 to 2.0. Notice that the frequency range spreads over 3 decades. The sound pressure level increases by 60 dB from a Mach 0.3 jet to a Mach 2.0 jet. That there is good agreement over such a large range of frequency and sound pressure level indicate that the theory must contain the essential physics of the generation and propagation of fine scale turbulence noise.

Figures 1.27(a) and 1.27(b) show comparisons between calculated and measured noise spectra at inlet angle 83° and 93° for a hot Mach 2 jet. The data are from the NASA Langley Research Center jet noise data bank of Seiner. The spectra at three temperatures are shown in these figures. Temperature ratio $T_r/T_a = 4.89$ is the highest known temperature ratio at which accurate jet noise data have been measured.

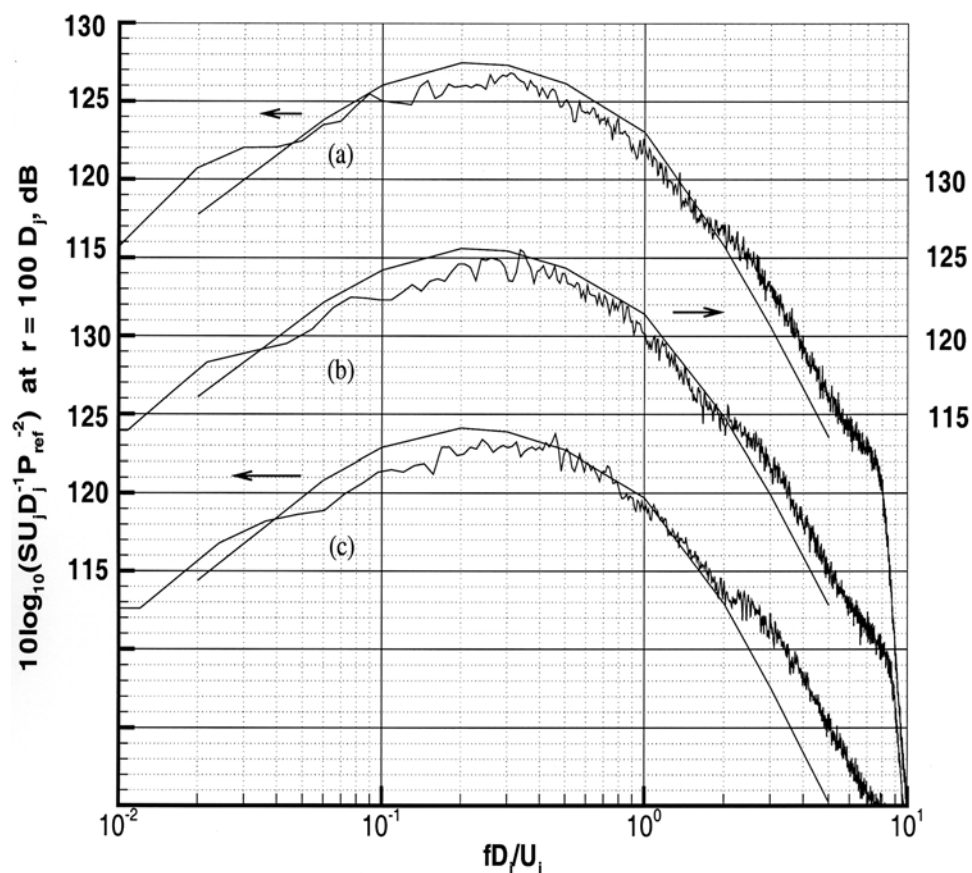


Figure 1.27(a). Comparisons between calculated noise spectra and experiment. $M_j = 2.0$, inlet angle = 83° . (a) $T_r/T_a = 4.89$, (b) $T_r/T_a = 4.08$, (c) $T_r/T_a = 3.28$.

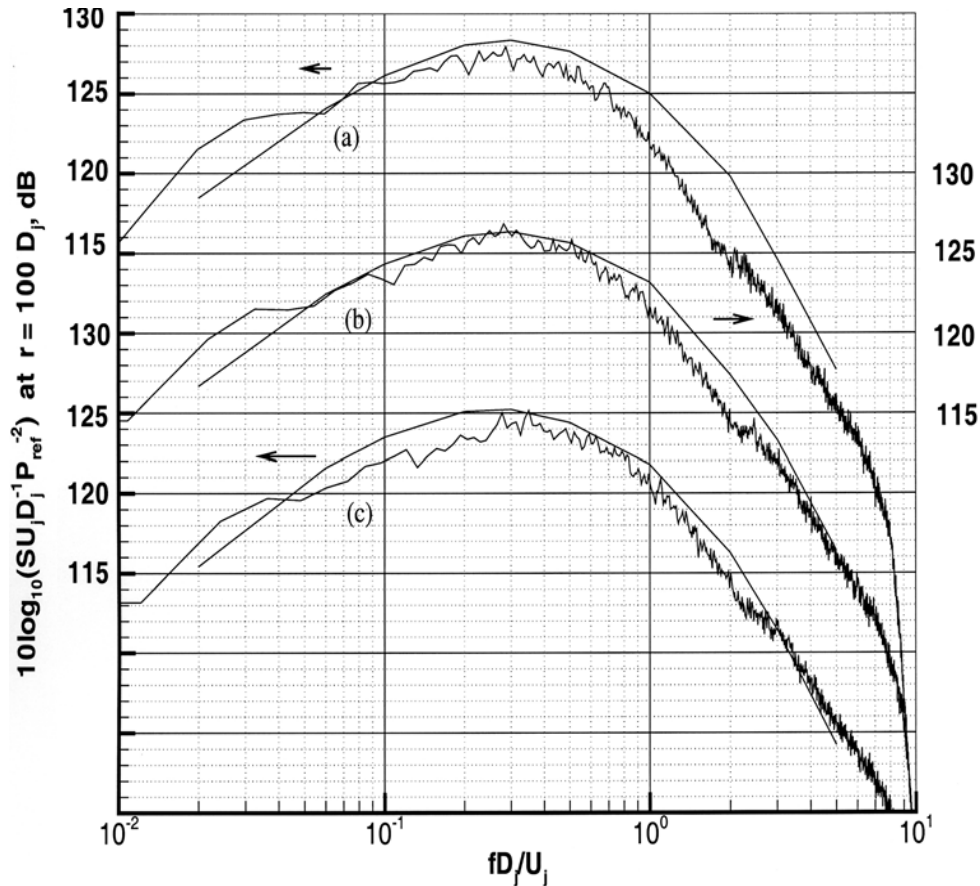


Figure 1.27(b). Comparisons between calculated noise spectra and experiment. $M_j = 2.0$, inlet angle = 93° . (a) $T_r/T_a = 4.89$, (b) $T_r/T_a = 4.08$, (c) $T_r/T_a = 3.28$.

1.5 Broadband Shock Associated Noise

Broadband shock associated noise and screech tones are generated only when a quasi-periodic shock cell structure is present in the jet plume. It will be shown that the quasi-periodicity of the shock cells plays a crucial role in defining the characteristics of both the broadband and discrete frequency shock noise. The importance of the quasi-periodicity of the shock cells to broadband shock associated noise was first recognized by Harper-Bourne & Fisher (1974) in their pioneering work on this subject. They made use of the quasi-periodicity to explain some of the prominent characteristics of this noise component discussed earlier.

1.5.1 Shock Cell Structure

The shock cell structure of an imperfectly expanded supersonic jet is formed by oblique/normal shocks and expansion fans. These shocks and expansion fans are generated at the

nozzle lip because of the mismatch of the static pressures inside and outside the jet. For an underexpanded jet an expansion fan is initiated at the nozzle lip. The fan is necessary, for it allows the static pressure to decrease gradually to that of the ambient condition. For an overexpanded jet an oblique shock would form at the nozzle lip region. In passing through the shock the static pressure of the gas increases abruptly to match that outside the jet. The expansion fan or shock, once formed, propagates across the jet flow until it impinges on the mixing layer on the other side. Since the flow outside the jet is stationary or subsonic any shock or expansion fan is not allowed. The impinging shock or expansion fan is, therefore, reflected back into the jet plume. The reflection process is repeated many times downstream until the shock/expansion fan is dissipated by turbulence. It is these repeated reflections of the shock/expansion fan by the mixing layer of the jet which give rise to the quasi-periodic shock cells. From this point of view, the shock cell structure may be regarded as disturbances trapped inside the jet by the mixing layer surrounding the jet column. In other words, one may consider the jet flow as behaving like a waveguide for the disturbances which form the shock cell.

Prandtl (1904) appeared to be the first to analyze the shock cell of a supersonic jet. He used a linear vortex sheet jet model and developed a partial solution to estimate the shock cell spacing. The complete vortex sheet shock cell solution for slightly imperfectly expanded jets was given later by Pack (1950). This solution has a simple form in cylindrical coordinates (r, ϕ, x) . Let p_s be the pressure disturbance associated with the shock cells, then

$$p_s = \sum_{i=1}^{\infty} A_i \Phi_i(r) \cos(\kappa_i x) \quad (1.23)$$

where $A_i = 2\Delta p / \sigma_i$, $\Phi_i(r) = J_0(2\sigma_i r) / J_1(\sigma_i)$

$$J_0(\sigma_i) = 0, \quad \kappa_i = \frac{2\sigma_i}{D_j (M_j^2 - 1)^{1/2}}; \quad i = 1, 2, 3, \dots$$

Here, Δp is the static pressure difference inside and outside the jet at the nozzle exit. J_0 and J_1 are the Bessel functions of order 0 and 1. D_j is the fully expanded jet diameter and M_j is the jet Mach number. For a supersonic jet issuing from a convergent-divergent nozzle of design Mach number

M_d ($M_d = 1.0$ for a convergent nozzle) at fully expanded Mach number M_j , the fully expanded jet diameter D_j is related to the nozzle exit diameter D by,

$$\frac{D_j}{D} = \left(\frac{M_d}{M_j} \right)^{1/2} \left[\frac{1 + \frac{\gamma-1}{2} M_j^2}{1 + \frac{\gamma-1}{2} M_d^2} \right]^{\frac{\gamma+1}{4(\gamma-1)}}$$

where γ is the ratio of specific heats. Equation (1.23) may be considered as a decomposition of the shock cell structure into the waveguide modes of the jet flow. Here A_i , Φ_i and κ_i are the amplitude, eigenfunction or mode shape and wavenumber of the i^{th} waveguide mode. The shock cell spacing, L_s , is given by the longest wavelength ($n = 1$); i.e.,

$$L_s \cong \frac{2\pi}{\kappa_1} = \pi (M_j^2 - 1)^{1/2} \frac{D_j}{\sigma_1}. \quad (1.24)$$

Obviously, the vortex sheet shock cell model is not valid except near the nozzle exit, where the mixing layer of the jet is thin. Tam *et al.* (1985) extended the linear shock cell solution to jets with realistic mean flow profile using the method of multiple-scales expansion. Figure 1.28 shows a comparison between their calculated shock cell pressure distribution and the measurements of Norum & Seiner (1982a). On considering that the model is linear, the agreement between calculation and measurement is remarkably good especially in terms of the gross features such as the shock cell spacing and amplitude.

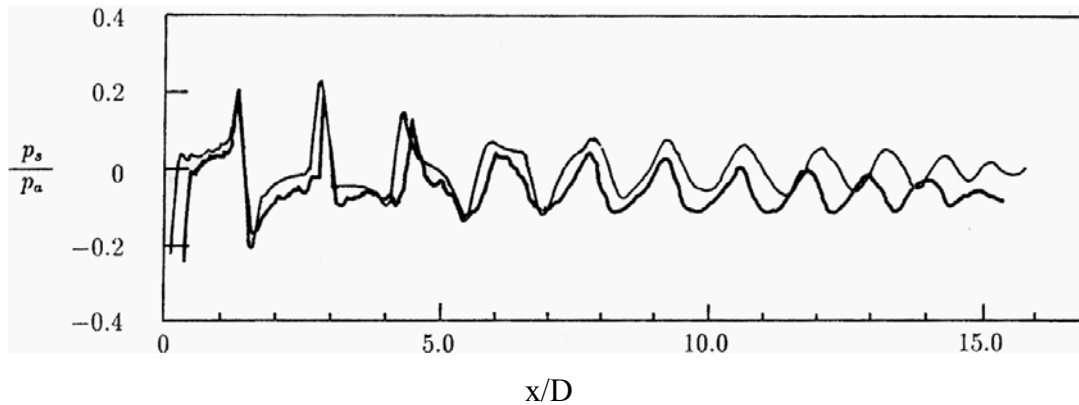


Figure 1.28. Comparison between calculated and measured shock cell axial pressure distribution at $r/D = 0.38$, $M_j = 1.82$, $M_d = 2.0$. Dark line = calculation, lighter line = measurement.

Dash *et al.* (1975), Seiner *et al.* (1975), Abdol-Hamid & Wilmoth (1989) and others have attempted to calculate the shock cells in highly imperfectly expanded supersonic jets numerically. They found that a good turbulence model was essential to a good prediction. However, for strongly screeching jets, all methods failed to capture the rapid decay of the shock cells.

Tam (1990) examined the extensive shock cell measurements of Norum & Seiner (1982a) and found that for moderately imperfectly expanded supersonic jets the first shock was very strong. However, downstream of the strong first shock, the shock cell structure resembled that of a weakly imperfectly expanded jet. Based on this observation, he suggested the use of the linear shock cell solution to model even the shock cells of moderately imperfectly expanded jets (not valid for the first shock, which is unimportant as far as broadband shock associated noise is concerned). He developed a semi-empirical formula by which the initial amplitude of the linear shock cells could be estimated.

1.5.2 Noise Generation Mechanism

Broadband shock associated noise is generated by the weak interaction between the downstream propagating large turbulence structures of the jet flow and the quasi-periodic shock cell structure during the passage of the former through the latter. It is interesting to see how such interaction could lead to the radiation of sound waves in the upstream directions and possess characteristics as described earlier. For simplicity, a one-dimensional model of the large turbulence structures-shock cell interaction is used to explain the noise generation process. A complete three-dimensional analysis can be found in the work of Tam (1987).

Let u_t be the velocity fluctuation associated with the large turbulence structures/instability waves. Within the one-dimensional model it may be represented mathematically by a traveling wave of the form

$$u_t = \text{Re} \left[A e^{i(kx - \omega t)} \right] \quad (1.25)$$

where $\text{Re}[\]$ is the real part of $[\]$. k and ω are the wavenumber and frequency of the wave disturbance. A is the amplitude. If u_c is the convection velocity of the large turbulence structures/instability waves, then $k = \omega/u_c$. Now, in one dimension, the velocity fluctuation, u_s ,

associated with the i^{th} waveguide mode of the shock cells may be represented by a spatially periodic function. Without loss of generality, let

$$u_s = B \cos \kappa_i x = \frac{B}{2} \left(e^{i\kappa_i x} + e^{-i\kappa_i x} \right) \quad (1.26)$$

where k_i is the i^{th} shock cell wavenumber and B is the amplitude. The corresponding shock cell spacing is equal to $2p/k_i$.

The interaction between the downstream propagating large turbulence structures/instability waves and the shock cells will give rise to disturbances consisting of product terms of equations (1.25) and (1.26). The interaction term most relevant to broadband shock associated noise is given by the product of u_t and the second term on the right side of (1.26). It is

$$\text{Re} \left\{ \frac{AB}{2} \exp \left[i \left((k - \kappa_i) x - \omega t \right) \right] \right\}. \quad (1.27)$$

(1.27) represents a traveling wave with wave number $(k - k_i)$. If k_i is slightly larger than k , then the phase speed $C = \omega/(k - k_i)$ of the interaction wave is negative and supersonic. According to the wavy wall analogy (see Figure 1.20) it would immediately lead to Mach wave radiation in the upstream direction.

The direction of radiation q is related to the phase speed C and the ambient sound speed a_∞ by the Mach wave relation; i.e.,

$$\frac{a_\infty}{C} = \frac{a_\infty (k - \kappa_i)}{\omega} = \cos \theta. \quad (1.28)$$

Now, in terms of shock cell spacing $L_i = 2p/k_i$, turbulence convection velocity u_c and frequency $f = \omega/2p$, (1.28) may be rewritten as

$$f = \frac{u_c}{L_i \left(1 - \frac{u_c \cos \theta}{a_\infty} \right)}. \quad (1.29)$$

As noted by Tam & Tanna (1982), (1.29) gives the relationship between the spectral peak frequencies and the direction of radiation of broadband shock associated noise. This characteristic property was discussed before and can be seen in the data of Figure 1.18. Since the shock cells can be considered as composed of a number of waveguide modes, (1.29) implies that the total noise spectrum is made up of a superposition of many spectral peaks. The spectral peak frequencies can be calculated by (1.29).

The above one-dimensional model illustrated the crucial noise generation processes of broadband shock associated noise. Basically this noise component is generated by the constructive scattering of the large turbulence structures of the jet flow by the stationary quasi-periodic shock cells in the jet plume. Since the shock cells can be conceived as made up of a superposition of waveguide modes of different wavelengths, each mode scatters off sound in a preferred direction. This results in a multi-peak noise spectrum as well as the observed directional dependence of the spectral peak frequency.

1.5.3 Stochastic Model Theory

In a series of papers (1987, 1990, 1991b, 1992), Tam developed a semi-empirical stochastic model theory for the prediction of broadband shock associated noise. In formulating the theory, Tam divided the flow variables into four components, namely, the mean flow, the large turbulence structures/instability waves, the shock cells and the disturbances arising from the interaction between the large turbulence structures/instability waves and the shock cells. The last of the four components contained the broadband shock associated noise. Tam showed that this component could be found by solving a nonhomogeneous boundary value problem. The nonhomogeneous terms were the product terms of the large turbulence structures/instability waves and the shock cells. Tam (1987) solved this problem formally. However, to make use of the formal solution for noise prediction, extensive numerical computations were required. To avoid such lengthy computations, Tam introduced a similarity spectrum to approximate the disturbances generated by the turbulence shock cell interaction. The similarity spectrum was based on the assumption that the noise source spectrum (the large turbulence structures) had no

intrinsic length and time scales. When this is true the spectrum must be a function of fx/U_j where f is the frequency, x is the downstream distance and U_j is the fully expanded jet velocity. The semi-empirical theory of Tam contains four parameters, two of which can, in principle, be calculated by means of the instability wave theory. The unknown parameters were determined empirically by Tam (1987, 1990).

Let u_c , u_j and u_f be the convection velocity of the instability waves, the jet velocity, and the flight velocity, respectively. If T_r is the total temperature of the jet and T_∞ is the ambient temperature, then u_c may be estimated by the following formula:

$$\frac{u_c}{u_j} = \begin{cases} \left[0.7 - 0.06 \left(\frac{T_r}{T_\infty} - 1.0 \right) \right] \left(1 - \frac{u_f}{u_j} \right) + \frac{u_f}{u_j}, & \frac{T_r}{T_\infty} > 1 \\ 0.7 + 0.3 \frac{u_f}{u_j}, & \frac{T_r}{T_\infty} < 1 \end{cases} \quad (1.30)$$

The half-width, L , of the similarity noise source may be estimated by the empirical formula,

$$L = \frac{3.3 \left(\frac{x_c}{8.0} \right) \left[1.0 + \left(1.114 - 0.36 \frac{T_j}{T_\infty} \right) M_f \right]}{D_j} \quad (1.31)$$

where x_c , the core length of the jet, can be calculated by

$$\frac{x_c}{D_j} = \begin{cases} 4.3 + 1.2 M_j^2, & T_j > T_\infty \\ 4.3 + 1.2 \left[M_j^2 + \left(1 - \frac{T_j}{T_\infty} \right) \right], & T_j < T_\infty \end{cases} \quad (1.32)$$

where T_j is the temperature of the jet, and D_j is the fully expanded jet diameter related to the nozzle exit diameter D by

$$\frac{D_j}{D} = \left\{ \frac{1 + \left[\frac{(\gamma-1)}{2} \right] M_j^2}{1 + \left[\frac{(\gamma-1)}{2} \right] M_d^2} \right\}^{\frac{(\gamma+1)}{4(\gamma-1)}} \left(\frac{M_d}{M_j} \right)^{\frac{1}{2}} \quad (1.33)$$

where M_d is the nozzle design Mach number. The shock cell spacing, L_m , of hot jets is related to wavenumber k_m by $L_m = 2\pi/k_m$. The wave number of the m^{th} shock cell waveguide mode k_m may be calculated by,

$$k_m(\text{hot jet at } M_f) = \frac{k_m(\text{cold jet at } M_f = 0)}{1.0 + \left(0.812 - \frac{0.254T_j}{T_\infty} \right) M_f} \quad (1.34)$$

with the parameters of the shock cell structure determined. A broadband shock associated noise power spectrum formula for hot supersonic jets in flight in the nozzle fixed coordinates is derived by Tam (1995) as,

$$\begin{aligned} S_{R \rightarrow \infty}(R, \psi, f) = & \frac{\bar{c} L^2 \bar{A}^2 A_j \rho_\infty^2 a_\infty^4 M_j^2}{R^2 (1 - M_f^2 \sin^2 \psi) f \left(\frac{f D_j}{u_j} \right) \left\{ 1 + \left[\frac{(\gamma-1)}{2} \right] M_j^2 \right\}} \\ & \times \left\{ \sum_{m=1}^N \frac{1}{\sigma_m^2 J_1^2(\sigma_m)} \cdot \exp \left[- \left(\frac{f_m}{f} - 1 \right)^2 \cdot \left(1 + M_c \frac{M_f (1 - M_f^2 \sin^2 \psi)^{\frac{1}{2}} + \cos \psi}{(1 - M_f^2)(1 - M_f^2 \sin^2 \psi)^{\frac{1}{2}}} \right)^2 \left(\frac{u_j}{u_c} \right)^2 \frac{L^2}{2 \ln 2} \right] \right\} \end{aligned} \quad (1.35)$$

where $\bar{c} = 2.65 \times 10^{-4} S_0$ ($S_0 = 0.35$), $A_j = \pi D_j^2/4$, and a_∞ is the ambient speed of sound. J_1 is the Bessel function of order one, and σ_m is the m^{th} zero of the Bessel function of order zero. In (1.35) the factor $f D_j/u_j$ in the denominator is to be replaced by S_0 whenever it is less than S_0 and

$$f_m = \frac{\frac{u_c k_m}{(2\pi)}}{1 + M_c \left\{ \frac{\left[M_f (1 - M_f^2 \sin^2 \psi)^{\frac{1}{2}} + \cos \psi \right]}{\left[(1 - M_f^2)(1 - M_f^2 \sin^2 \psi)^{\frac{1}{2}} \right]} \right\}} \quad (1.36)$$

In formulating the broadband shock associated noise theory it has always been assumed that the convergent-divergent nozzle of M_d is perfectly manufactured. That is, when operating at a fully expanded Mach number $M_j = M_d$, there is no shock cell structure in the jet plume. In practice this is not always true, especially for hot jets. Because of various nozzle imperfections, a residual shock cell structure invariably exists so that even when the jet is operating nominally at the design Mach number, there is still broadband shock associated noise. To account for this deviation from an ideal condition, one may incorporate empirically a residue shock cell strength ε in the parameter \bar{A}^2 of (1.35) as follows:

$$\bar{A}^2 = \begin{cases} \frac{\left[\frac{(M_j^2 - M_d^2)^2 + \varepsilon}{\left[1 + \frac{\gamma-1}{2} M_d^2\right]^2} \right] \left(\frac{D}{D_j}\right)^2}{1 + 3 \left[\frac{(M_j^2 - M_d^2)}{\left(1 + \frac{\gamma-1}{2} M_d^2\right)} \right]^3} & \text{(underexpanded jets)} \\ \frac{\left[\frac{(M_j^2 - M_d^2)^2 + \varepsilon}{\left[1 + \frac{\gamma-1}{2} M_d^2\right]^2} \right]}{1 + 6 \left[\frac{(M_d^2 - M_j^2)}{\left(1 + \frac{\gamma-1}{2} M_d^2\right)} \right]^5} & \text{(overexpanded jets)} \end{cases} \quad (1.37)$$

where $\varepsilon = 0$ corresponds to a C-D nozzle without imperfections. Based on a number of numerical test cases, it is found that a value of $\varepsilon = 0.03$ gives generally satisfactory results compared with experimental measurements. It should be noted that the residual shock cell strength is important only when the jet is operating closed to its nominal condition.

Extensive comparisons between the semi-empirical noise prediction formula and experimental measurements have been carried out. For all the cases compared, agreement good enough for engineering application was found. This was true regardless of whether the jet was hot or cold and whether the jet was underexpanded or overexpanded. In these tests, the nozzle design Mach number and the fully expanded jet Mach number covered the range of 1.0 to slightly over 2.0. Figure 1.29 shows typical calculated noise spectra and the corresponding experimental measurements. As can be seen, except for the dips at small inlet angle directions, there is good agreement between the calculated and the measured spectra.

The semi-empirical theory is also capable of predicting the near field broadband shock associated noise. This is important from the standpoint of sonic fatigue since structures near the tail part of a jet aircraft are exposed to constant broadband shock associated noise radiation. Calculated near field noise contours and their comparisons with the measurements of Yu (1970) are provided in the work of Tam (1987). The contour shapes and distributions are shown to agree well with measurements.

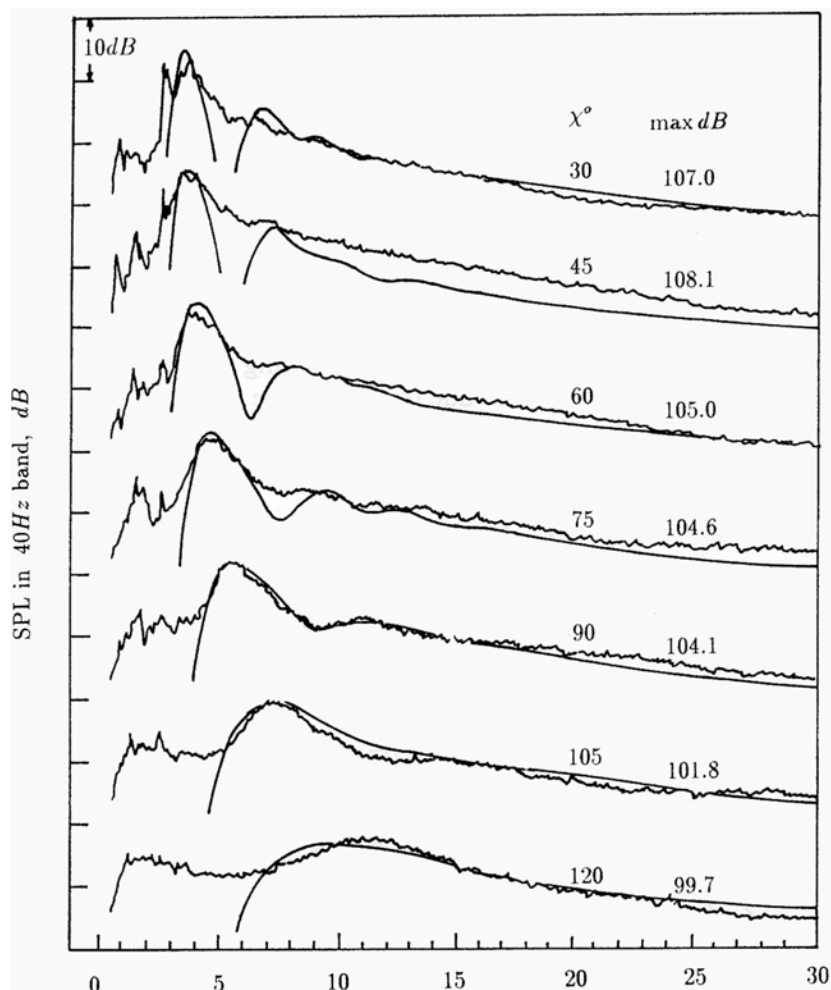


Figure 1.29. Comparisons between calculated broadband shock noise spectra and measurements of Norum & Seiner (1982a). $M_j = 1.67$, $M_d = 1.0$

The original effort in developing semi-empirical broadband shock associated noise prediction method was primarily for circular jets. Later Tam and Reddy (1996) extended the approach to rectangular jets. The change in geometry requires modification to the shock cell model as well as to the large turbulence structures/instability wave model. An extra parameter, namely, the aspect

ratio of the jet, has to be introduced. The predictions of the extended theory were shown to agree fairly well with measurements. However, the data base is limited. Further testing of the semi-empirical theory would provide added confidence in its accuracy.

1.6 Screech Tones

Screech tones are very sensitive to changes in the surrounding environment. This makes them somewhat unpredictable. For instance, Norum (1983) found that the screech intensity increased by 10dB when a thin lip nozzle was replaced by one with a thicker lip. Moreover, it has been reported by Seiner *et al.* (1986) that the flapping plane of a screeching jet was found, for unknown reasons, to have rotated by almost 90 degrees when the same experiment was repeated a month later in the same facility by the same investigators.

1.6.1 Tone Generation Mechanism

Powell (1953a,b) was the first to report the observation of screech tones. He correctly suggested that it was an acoustic feedback phenomenon. Over the years, our understanding of the details of the screech feedback loop has undergone significant changes. Figure 1.30 shows the present day view of the various components of the feedback loop. Near the nozzle lip where the jet mixing layer is thin and most receptive to external excitation, acoustic disturbances impinging on this area excite the intrinsic instability waves of the jet flow. The amplitude of the excited instability is small near the nozzle exit. However, as the instability wave propagates downstream it extracts energy from the mean flow and grows rapidly in amplitude. After propagating a distance of four to five shock cells, the instability wave, having acquired a large enough amplitude, interacts with the quasi-periodic shock cells in the jet plume. The unsteady interaction generates acoustic radiation. For the same reason as in the case of broadband shock associated noise, the acoustic radiation is primarily in the upstream direction as illustrated in Figure 1.30. The feedback acoustic waves propagate upstream outside the jet. Upon reaching the nozzle lip region, they excite the shear layer of the jet leading to the generation of new instability waves. In this way, the feedback loop is closed.

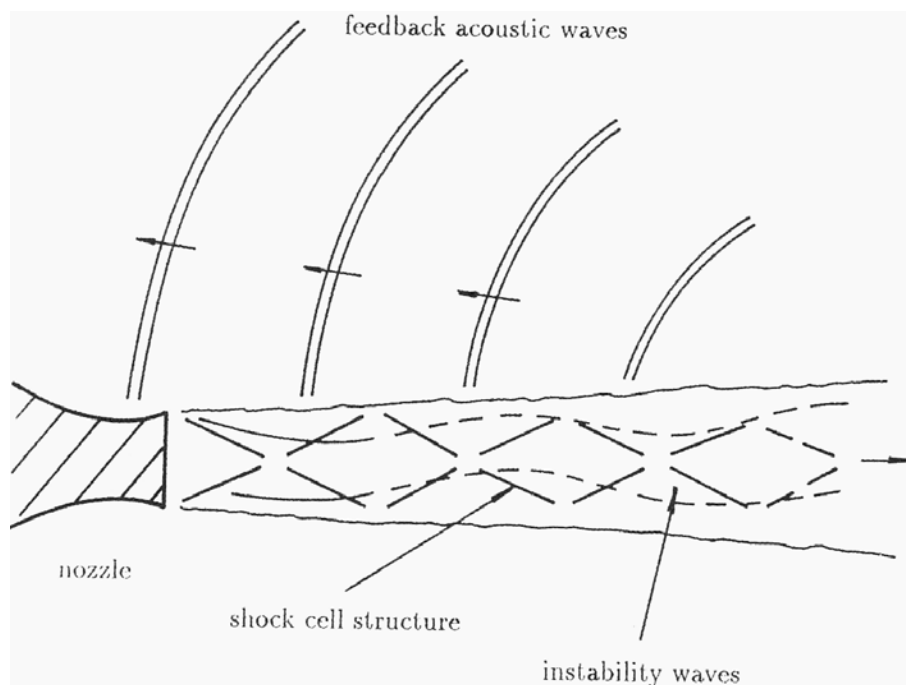


Figure 1.30. Schematic diagram of the screech tone feedback loop.

1.6.2 Fundamental Screech Tone Frequency

Tam *et al.* (1986) suggested that the weakest link of the screech feedback loop is at the nozzle lip where feedback acoustic waves excite the instability wave. Their contention is that unless the acoustic waves are sufficiently strong, the excitation process will not be able to generate instability waves at a large enough amplitude (above the background noise) to maintain the feedback loop. To maintain the feedback process, it is, therefore, essential that the direction of maximum acoustic radiation generated by the passage of the instability wave through the shock cells of the jet be in the direction of the nozzle lip. The relation between the sound frequency and the direction of radiation is given by (1.29). By setting $\theta = \pi$, we achieve a formula by which the fundamental screech frequency can be estimated. By adapting the empirical results of $u_c \cong 0.7U_j$ (U_j = fully expanded jet velocity) and the shock cell spacing at four to five shock cells downstream to be about 20% smaller than that given by the vortex sheet shock cell model (1.24), Tam *et al.* (1985) derived the following screech tone frequency formula for a jet of Mach number M_j .

$$\frac{f_s D_j}{U_j} = 0.67 (M_j^2 - 1)^{\frac{1}{2}} \left[1 + 0.7 M_j \left(1 + \frac{\gamma - 1}{2} M_j^2 \right)^{-\frac{1}{2}} \left(\frac{T_r}{T_\infty} \right)^{\frac{1}{2}} \right]^{-1} \quad (1.38)$$

where f_s is the fundamental screech frequency. T_r is the total temperature of the jet and T_∞ is the ambient temperature. D_j is the fully expanded jet diameter (see equation 1.33).

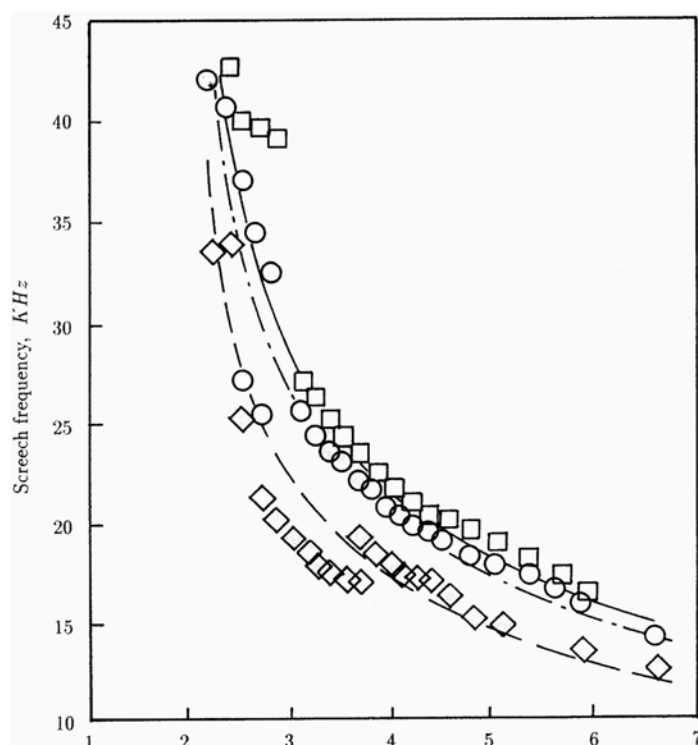


Figure 1.31. Comparisons between measured and calculated screech tone frequencies at different total temperature T_r .

measured	calculated	T_r °C
◇	-----	18
○	— · — · —	323
□	—————	529

Figure 1.31 shows a comparison between (1.38) and the measurements of Rosfjord & Toms (1975) at three jet temperatures. In the experiment a convergent nozzle ($M_d = 1.0$) was used. The agreement between prediction and measurements is quite good. It is better at high temperature and high pressure ratio.

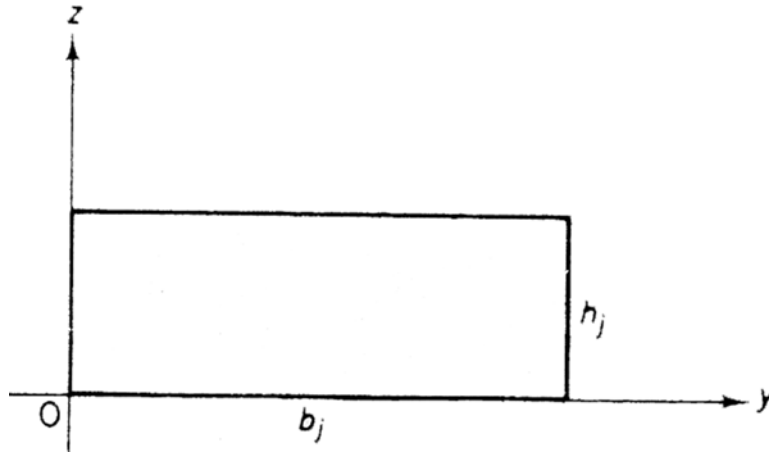


Figure 1.32. Rectangular jet with aspect ratio h_j/b_j .

Tam (1988) used similar ideas to derive a screech frequency formula for rectangular jets. Consider a vortex sheet bounded rectangular jet with fully expanded width, b_j , and height, h_j , as shown in Figure 1.32. For weak shocks, the governing equations are the linearized Euler equations.

$$\rho_i \nabla \cdot \mathbf{v} + u_j \frac{\partial p}{\partial x} = 0 \quad (1.39(a))$$

$$\rho_i u_j \frac{\partial \mathbf{v}}{\partial x} = -\nabla p \quad (1.39(b))$$

$$p = a^2 \rho. \quad (1.39(c))$$

By elimination, a single governing equation for p is

$$\nabla^2 p - M_j^2 \frac{\partial^2 p}{\partial x^2} = 0 \quad (1.40)$$

where M_j is the Mach number. At the vortex sheet, linearized form of the dynamic boundary condition (pressure balance) yields

$$p = 0 \quad \text{at the vortex sheet.} \quad (1.41)$$

It will be assumed that the pressure at the nozzle exit, p_e , is uniform across the entire cross section of the jet and differs from the ambient pressure, p_a , by an amount Δp . It will further be assumed that at the nozzle exit the flow velocity is paralleled to the x -axis or the direction of jet flow. Thus the initial conditions for the shock cell solution at the nozzle exit $x = 0$ are,

$$p = \Delta p \quad \text{and} \quad v_y = v_z = 0. \quad (1.42)$$

The solution of (1.40) satisfying boundary condition (1.41) and nozzle exit condition (1.42) is

$$p(x, y, z) = \sum_{n=1}^{\infty} \sum_{m=1}^{\infty} \frac{4\Delta p}{nm\pi^2} (1 - \cos n\pi) (1 - \cos m\pi) \sin \frac{n\pi y}{b_j} \sin \frac{m\pi z}{h_j} \cos k_{nm}x \quad (1.43)$$

where

$$k_{nm} = \left(\frac{n^2}{b_j^2} + \frac{m^2}{h_j^2} \right)^{\frac{1}{2}} \frac{\pi}{(M_j^2 - 1)^{\frac{1}{2}}}, \quad n, m = 1, 2, 3, \dots \quad (1.44)$$

The smallest eigenvalue or wave number is k_{11} . Thus the shock cell spacing L_s is equal to

$$L_s = \frac{2\pi}{k_{11}} = 2(M_j^2 - 1)^{\frac{1}{2}} \frac{h_j}{\left(1 + \frac{h_j^2}{b_j^2} \right)^{\frac{1}{2}}}. \quad (1.45)$$

If $h_j/b_j < 1/4$, then (1.45) may be approximated by

$$L_s = 2(M_j^2 - 1)^{\frac{1}{2}} h_j, \quad (1.46)$$

which is the shock cell spacing of a two-dimensional jet with thickness h_j .

To compare (1.46) with experiments, it is necessary to relate the fully expanded jet width b_j and height h_j to the nozzle exit dimensions. Tam and Tanna (1982) pointed out that the effective size of a fully expanded supersonic jet is not the same as that at the nozzle exit. The difference is a function of jet operating conditions and could sometimes be significant. To account for the size difference let A_d and A_j be the cross-sectional area of a jet at the nozzle exit and that of the fully expanded jet, M_d and M_j be the nozzle design Mach number and the fully expanded Mach number. From one-dimensional gas dynamics, it is easy to see that A_j and A_d are related by (see the derivation provided by Tam (2005)),

$$\left(\frac{A_j}{A_d}\right)^2 = \frac{M_d^2}{M_j^2} \left[\frac{1 + \frac{\gamma-1}{2} M_j^2}{1 + \frac{\gamma-1}{2} M_d^2} \right]^{\frac{\gamma+1}{\gamma-1}}. \quad (1.47)$$

Let b and h be the nozzle exit dimensions; then, by assuming the differences between the width and height of the fully expanded jet and b and h are small, it is simple to find,

$$\frac{h_j}{h} = \left[\frac{A_j}{A_d} - 1 \right] \frac{b}{h+b} + 1 \quad (1.48(a))$$

$$\frac{b_j}{b} = \left[\frac{A_j}{A_d} - 1 \right] \frac{h}{h+b} + 1. \quad (1.48(b))$$

In the case $b \gg h$, the shock cell spacing as given by (1.46), (1.47) and (1.48) reduces to,

$$\frac{L_s}{h} = 2 \left(M_j^2 - 1 \right)^{\frac{1}{2}} \left[\frac{1 + \frac{\gamma-1}{2} M_j^2}{1 + \frac{\gamma-1}{2} M_d^2} \right]^{\frac{\gamma+1}{2(\gamma-1)}} \frac{M_d}{M_j}. \quad (1.49)$$

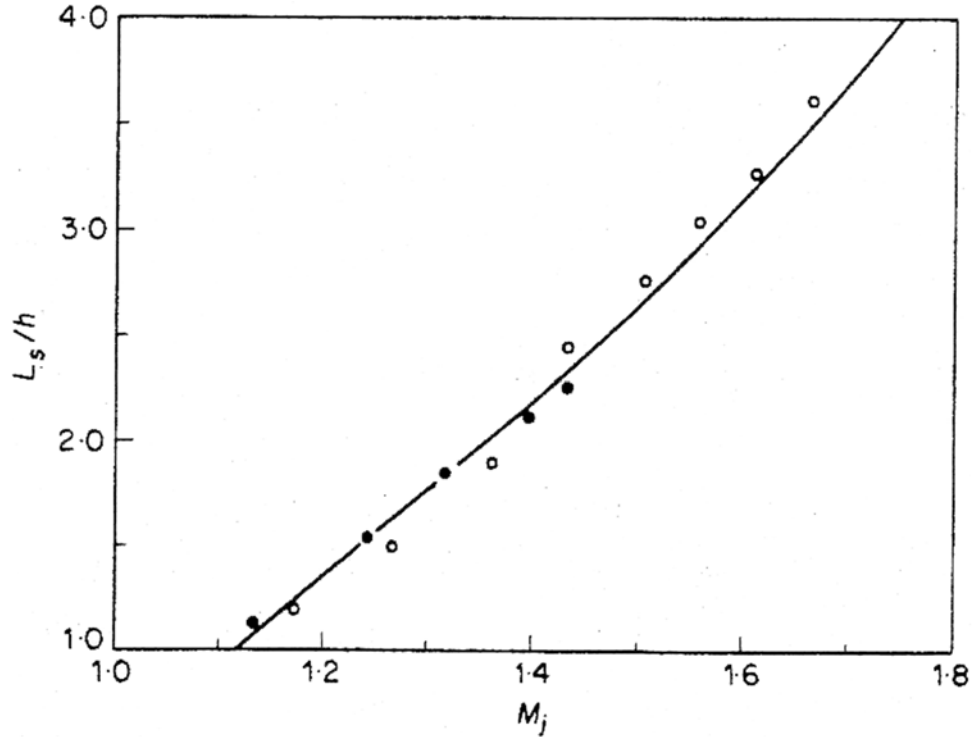


Figure 1.33. Comparison between measured and calculated shock cell spacings of rectangular jets. ●, Powell (1953), $b/h = 5.83$; ○, Hammit (1961), $b/h = 12.75$; —, (1.46)

Figure 1.33 shows comparisons between (1.49) and the measured data of Powell (1953c) and Hammit (1961). There is good agreement over a wide range of jet Mach number.

According to the weakest line screech feedback tone model of Tam, Seiner and Yu (1986), the screech frequency may be obtained by setting $\Theta = \pi$ and $L_s = L_{11}$ in (1.29). This gives the following screech tone frequency formula for rectangular jets.

$$\frac{fL}{u_j} = \frac{\frac{u_c}{u_j} \left[\left(\frac{h_j}{b_j} \right)^2 + 1 \right]^{\frac{1}{2}}}{2 \left(1 + \frac{u_c}{a_\infty} \right) (M_j^2 - 1)^{\frac{1}{2}}} \left\{ \frac{\left[1 + \frac{\gamma-1}{2} M_j^2 \right]^{\frac{\gamma+1}{2(\gamma-1)}}}{1 + \frac{\gamma-1}{2} M_d^2} \frac{M_d}{M_j} - 1 \right\} \frac{b}{b+h} + 1 \quad (1.50)$$

For cold choked jets ($M_d = 1.0$) with large aspect ratio (1.50) simplifies to,

$$\frac{fL}{u_j} = \frac{0.7 \left(\frac{1 + \frac{\gamma-1}{2}}{1 + \frac{\gamma-1}{2} M_j^2} \right)^{\frac{\gamma+1}{2(\gamma-1)}} M_j}{2(M_j^2 - 1)^{\frac{1}{2}} \left[1 + \frac{0.7 M_j}{\left(1 + \frac{\gamma-1}{2} M_j^2 \right)^{\frac{1}{2}}} \right]} \quad (1.51)$$

$u_c/u_j \cong 0.7$ has been used to derive (1.51).

Figure 1.34 shows a comparison of the numerical results of (1.51) and the experimental measurements of Raman (1996). There is excellent agreement between predictions and measurements over the Mach number range of $1.1 < M_j < 1.8$.

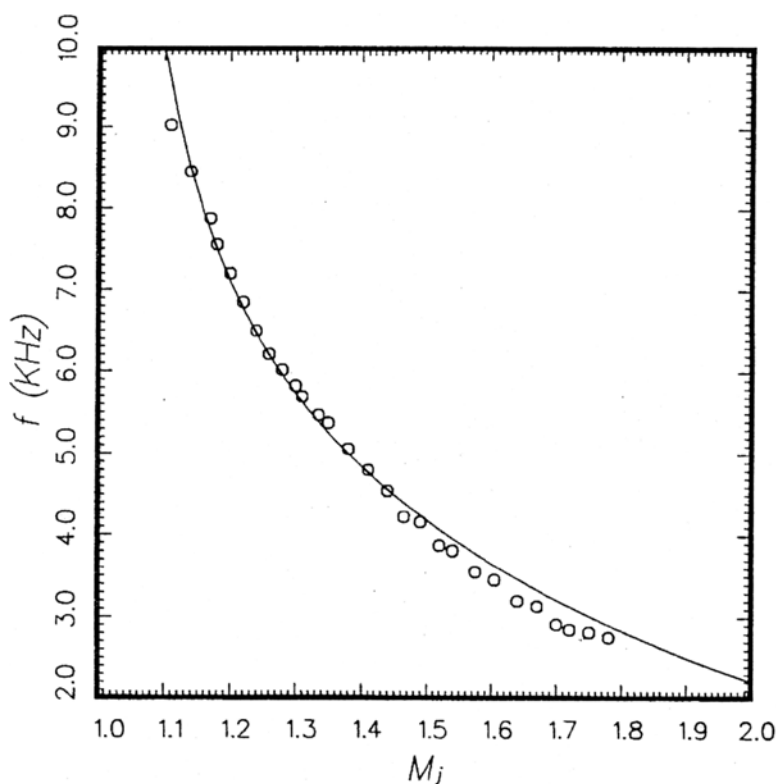


Figure 1.34. Variation of the screech frequency with fully expanded jet Mach number for a supersonic jet from a convergent rectangular nozzle; aspect ratio = 5, regular exit geometry: O, measurements and —, theory.

Some military jets use beveled rectangular nozzles as shown in Figure 1.35. The shock cell structure of jets issuing from this type of nozzle is highly complex. However, beyond the most downstream edge of the nozzle, the shock cell structure is quasi-periodic. This is the region where the feedback acoustic waves of the screech feedback loop are generated. The physical situation is very similar to that of a jet with regular straight nozzle exit. The major difference lies in that the dominant wave guide modes that make up the quasi-periodic shock cell structure are not necessarily the lowest-order modes. Moreover, it is possible that more than one mode is dominant.

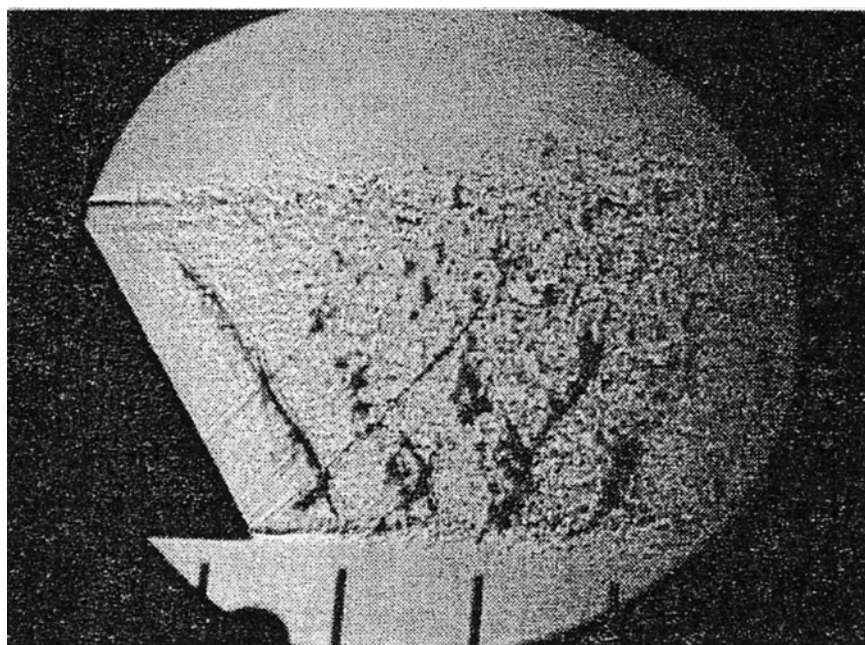


Figure 1.35. Spark Schlieren image of the shock cell structure of a Mach 1.4, aspect ratio 5, rectangular jet from a single-beveled convergent nozzle.

As far as screech tone feedback loop is concerned, the weakest link theory is still applicable. However, one expects the resulting screech tones to be more complex. This is because they are related to the higher-order modes; also, more than one feedback loop may be operating at the same time. On following the weakest link theory, Tam, Shen and Raman (1997) proposed that the screech frequencies can be calculated by replacing L_i in (1.29) by $2\pi/k_{nm}$ where k_{nm} are given by (1.44). For large aspect ratio jets ($b_j \gg k_j$) only the $m = 1$ modes are relevant. On restricting consideration to $m = 1$ modes, the following screech frequency formula is obtained:

$$f_n = \frac{0.55u_j}{2\pi \left[1 + \left(\frac{0.55u_j}{a_\infty} \right)^2 \right]^{\frac{1}{2}}} \left(\frac{n^2}{b_j^2} + \frac{1}{h_j^2} \right)^{\frac{1}{2}} \frac{\pi}{(M_j^2 - 1)^{\frac{1}{2}}} \quad (1.52)$$

where $n = 1, 2, 3, \dots$.

The screech frequencies of supersonic jets from beveled rectangular nozzles have been measured by Raman (1996). The frequency as a function of jet Mach number has a fairly complex pattern. Figure 1.36 shows the measured screech tone frequencies as a function of the jet Mach number for a supersonic jet from a single-beveled convergent rectangular nozzle. The data do not seem to form a continuous curve. There are frequency jumps at several jet Mach numbers. Also shown are the screech frequencies of (1.52) with spanwise mode number $n = 1, 2, 3$, and 4. As can be seen, the data correlate well with the theoretical frequency curves over the entire range of measured Mach numbers. Figure 1.37 shows a comparison of the measured screech frequencies and the frequencies of (1.52) for rectangular jets from a double-beveled convergent nozzle. The screech frequencies agree well with the $n = 5$ and 6 frequency curves.

Figure 1.38 shows the variation of the screech frequency with Mach number for the supersonic jet from a C-D rectangular nozzle with a regular exit geometry. Based on his spanwise phase data, Raman was able to identify three distinct screech modes. Their frequencies fit very well with the frequencies of the $n = 1, 3$, and 5 modes of (1.52). Figure 1.39 provides the measured screech frequency jet Mach number relation of the supersonic jet from a single-bevelled C-D rectangular nozzle. According to the phase data there are three modes; i.e., modes I, IIIA, and IIIB. Also shown are the screech frequency curves for $n = 1, 2, 3$, and 4 modes according to (1.52). The data appear to agree well with the frequency curves of the $n = 1, 2$, and 4 modes. Finally, Figure 1.40 shows the measured screech frequency variation with jet Mach number of a supersonic jet from a C-D double-beveled rectangular nozzle. Two modes have been identified. Their frequencies are in reasonable agreement with the $n = 6$ and 7 frequency curves of (1.52).

Equation (1.52) predicts many screech frequency bands. However, not all of the tones of the frequency bands are excited. It is believed that the selection of the excited frequencies is determined largely by two factors. These are the spatial growth rates of the instability waves of the jet flow and the strength of the waveguide modes of the shock cell structure.

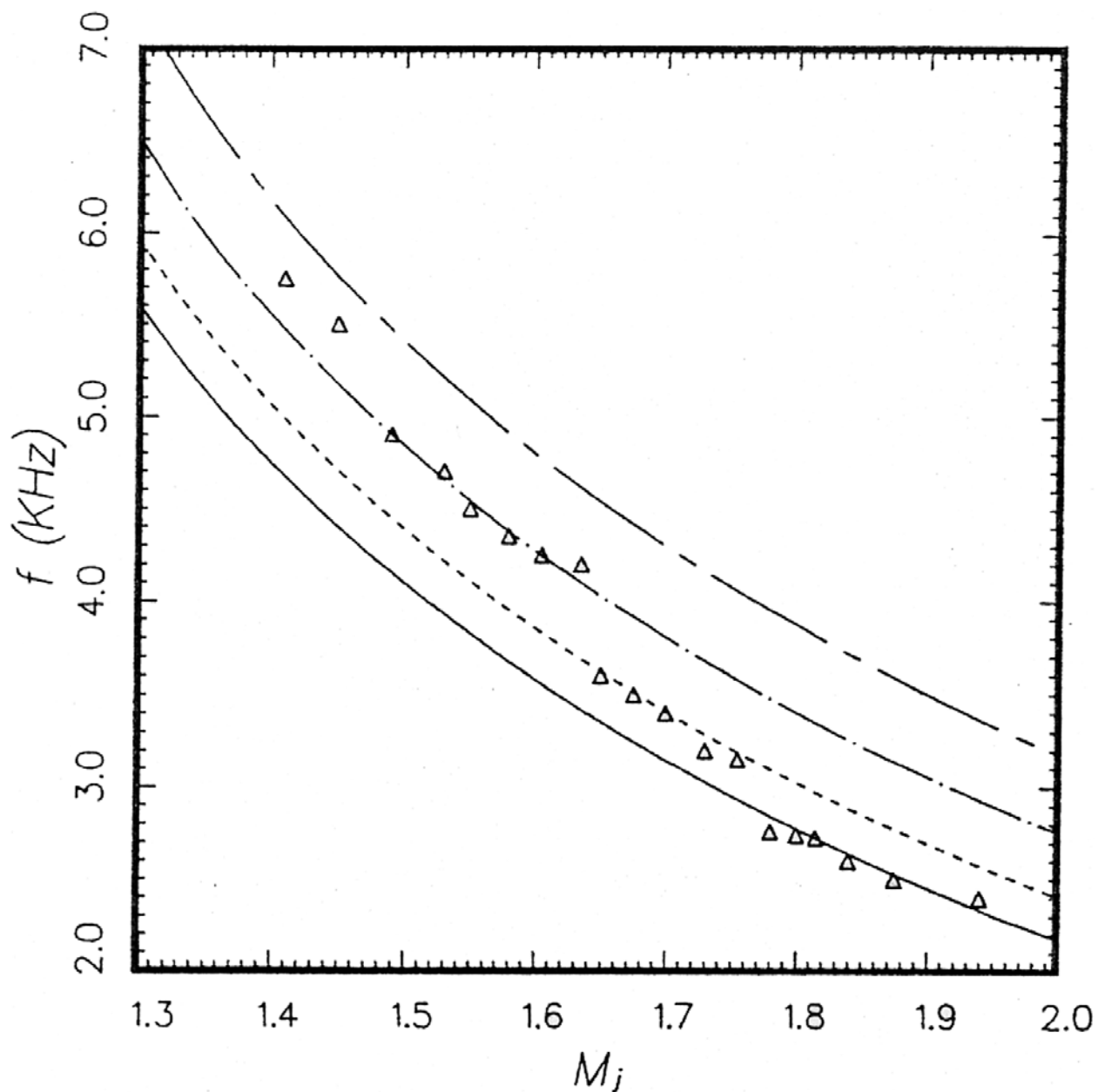


Figure 1.36. Variation of the screech frequencies with fully expanded jet Mach number for a supersonic jet from a convergent rectangular nozzle with aspect ratio = 5, single-beveled exit geometry: Δ , measurements. (1.52): —, $n = 1$; ----, $n = 2$; — · —, $n = 3$; and — — —, $n = 4$.

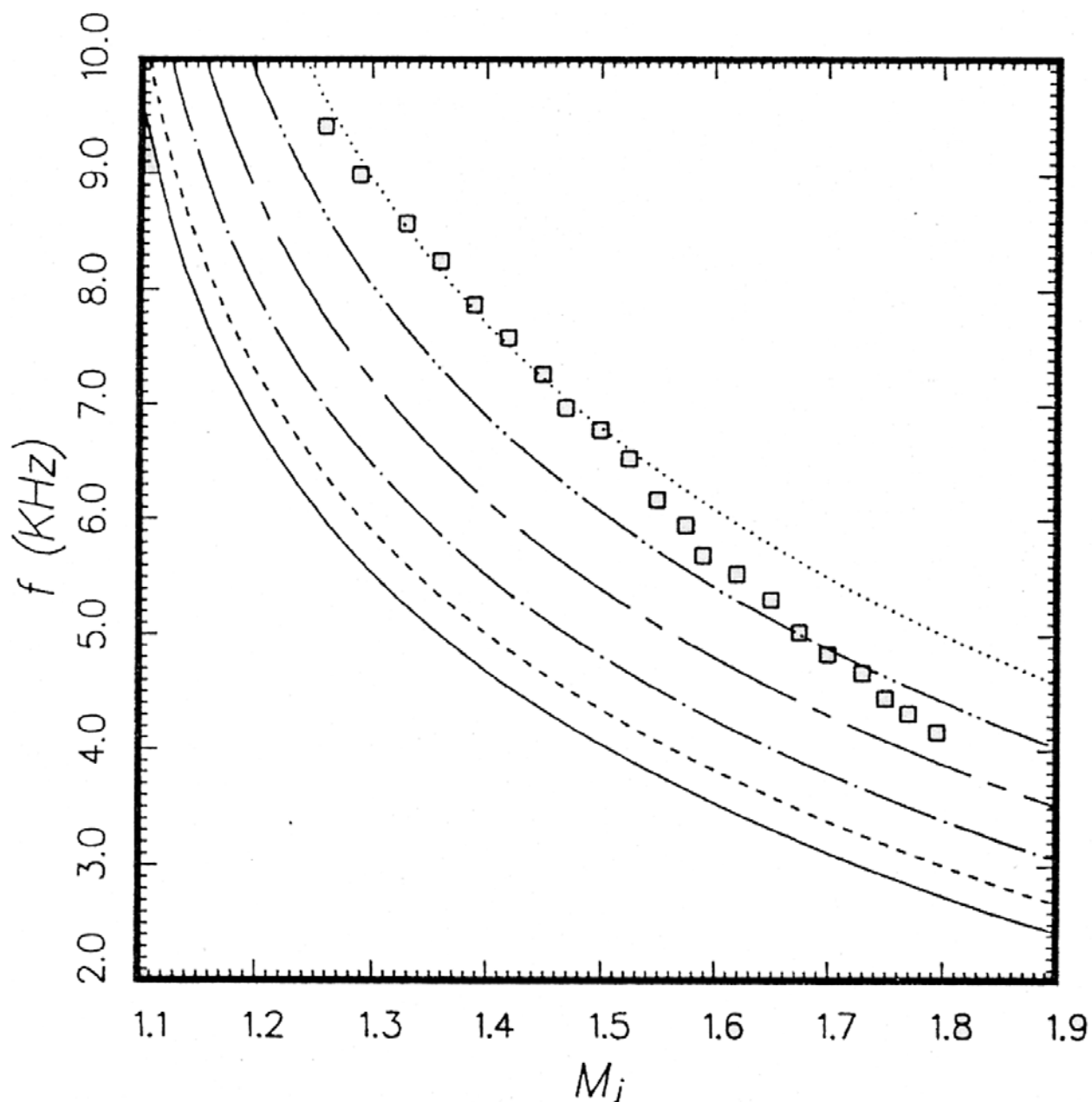


Figure 1.37. Variation of the screech frequencies with fully expanded jet Mach number for a supersonic jet from a convergent rectangular nozzle with aspect ratio = 5, double-beveled exit geometry: \square , measurements. (1.52): —, $n = 1$; ---, $n = 2$; — · —, $n = 3$; — — —, $n = 4$; — · · —, $n = 5$; and · · · · ·, $n = 6$.

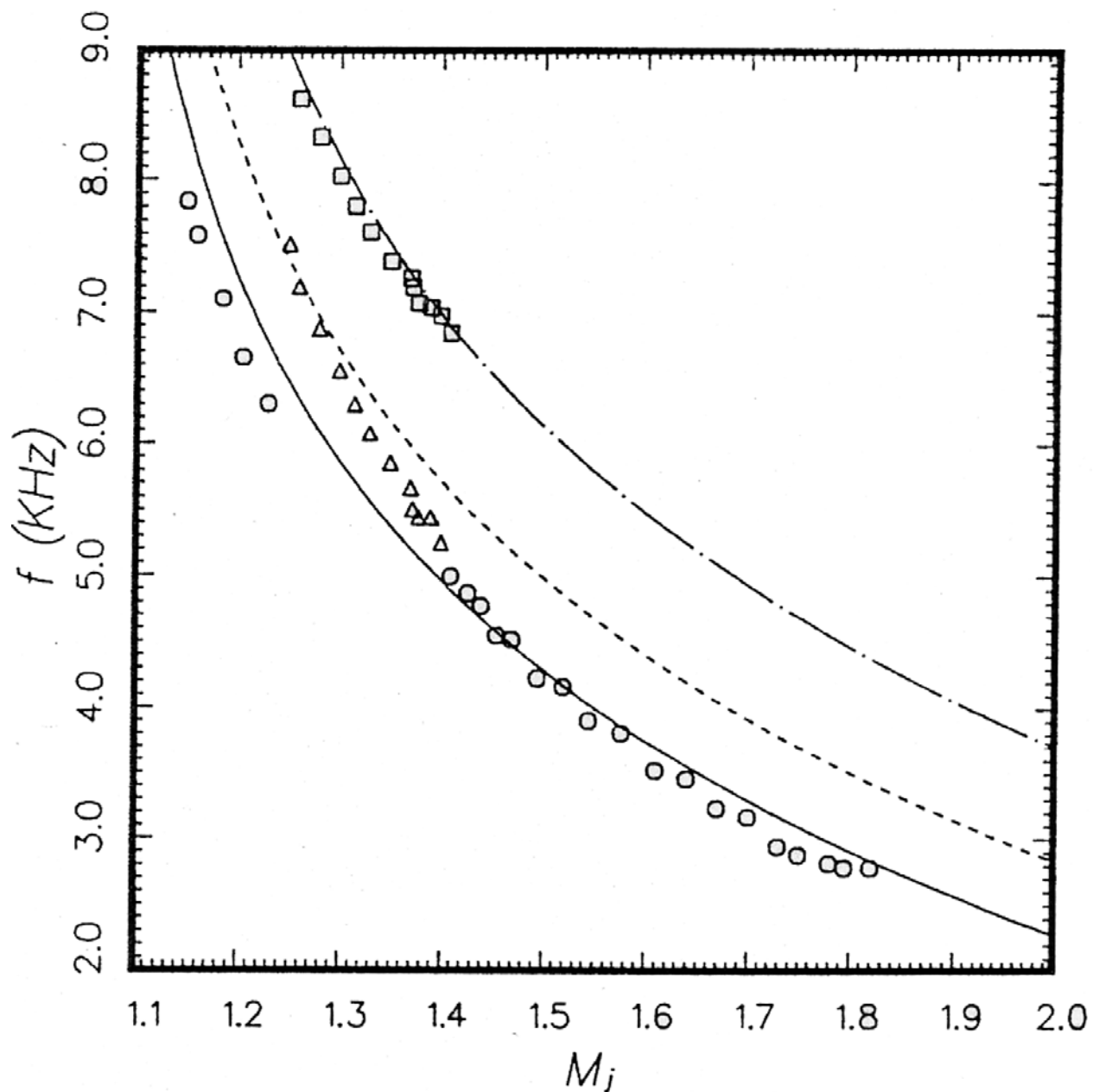


Figure 1.38. Variation of the screech frequencies with fully expanded jet Mach number for a supersonic jet from a convergent-divergent rectangular nozzle with aspect ratio = 5, $M_d = 1.4$, and regular exit geometry. Measurements: O, mode II; \triangle , mode I2; and \square , mode II. (1.52): —, $n = 1$; ---, $n = 3$; — · —, $n = 5$.

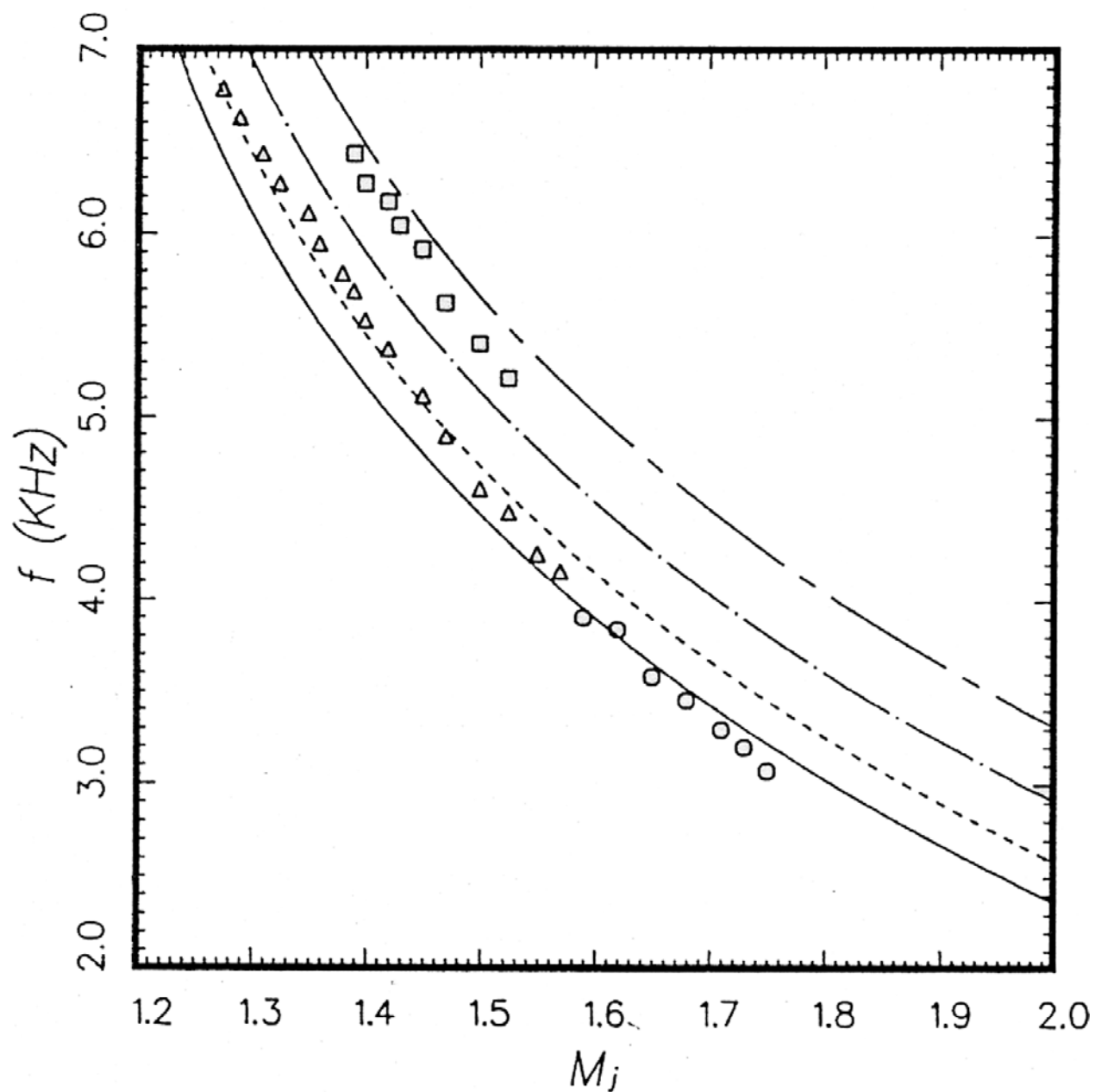


Figure 1.39. Variation of the screech frequencies with fully expanded jet Mach number for a supersonic jet from a convergent-divergent rectangular nozzle with aspect ratio = 5, $M_d = 1.4$, and single-beveled exit geometry. Measurements: \circ , mode I; \triangle , mode IIIA; and \square , mode IIIB. (1.52): —, $n = 1$; ---, $n = 2$; — · —, $n = 3$; and — — —, $n = 4$.

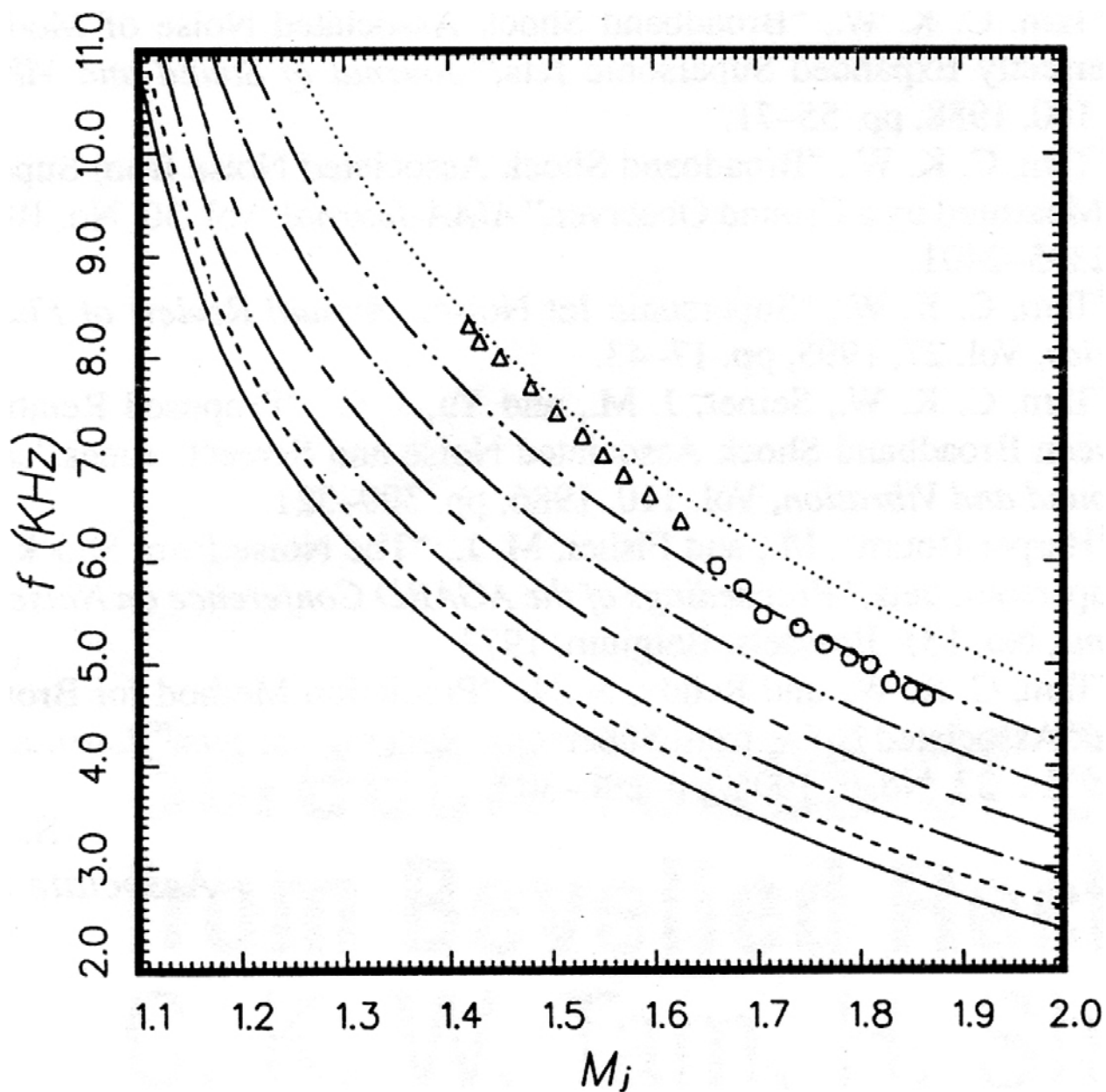


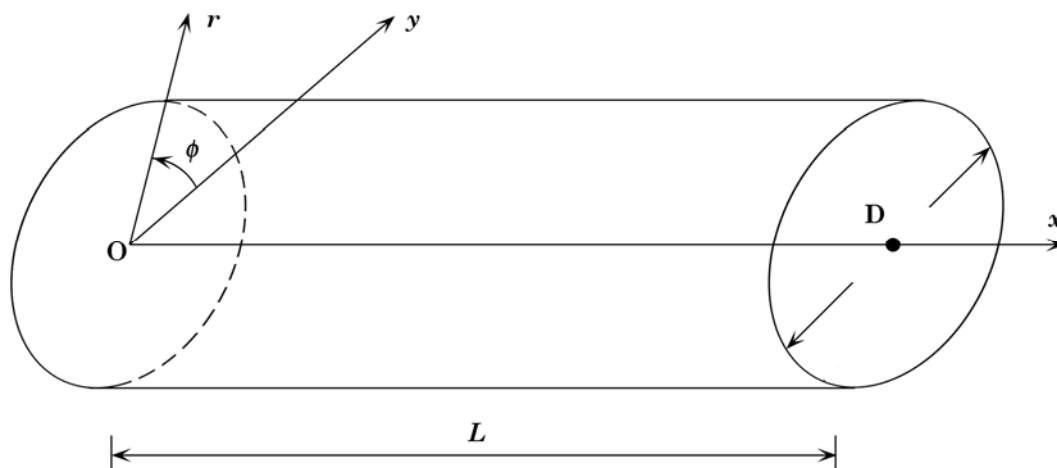
Figure 1.40. Variation of the screech frequencies with fully expanded jet Mach number for a supersonic jet from a convergent-divergent rectangular nozzle with aspect ratio = 5 and double-beveled exit geometry. Measurements: \circ , mode I and \triangle , mode II. (1.52): $---$, $n = 6$ and \cdots , $n = 7$.

Chapter 2. The Acoustic Environment Formed by a Test Cell

An engine test cell, invariably, provides a confined environment for acoustic waves. The constant reflections of acoustic waves by the solid walls and opened ends of an engine test cell lead to the formation of standing waves. These standing waves, often referred to as normal modes, allow the accumulation of wave energy. This results in large amplitude oscillations and resonances. For test cells with relatively simple geometry, the resonance frequencies can be found analytically. If the geometry is significantly complicated, CAA methods may have to be used.

2.1 Ejector Type Engine Test Cells

Ground level test cells are effectively large ejectors with open ends. The geometry may be circular or rectangular as shown in Figure 2.1.



(a) Cylindrical geometry

Figure 2.1. Ejector type ground level engine test cells.

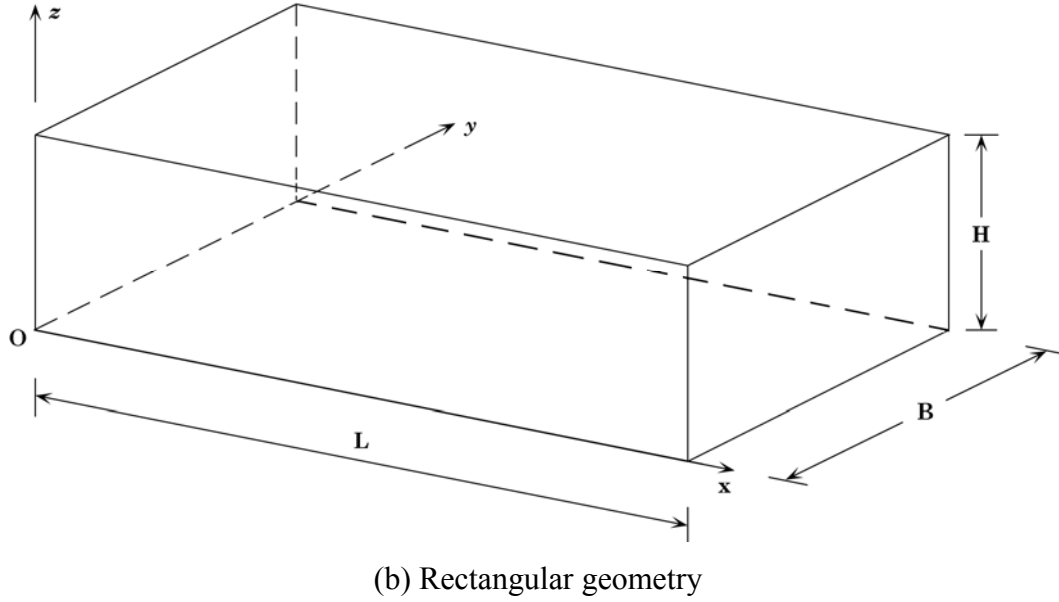


Figure 2.1. Ejector type ground level engine test cells.

Let us assume that there is a uniform mean flow, u_0 , in the axial or the x -direction. The governing equations for the acoustic disturbances are the linearized Euler equations.

$$\rho_0 \left(\frac{\partial \mathbf{V}}{\partial t} + u_0 \frac{\partial \mathbf{V}}{\partial x} \right) = -\nabla p \quad (2.1)$$

$$\frac{\partial p}{\partial t} + u_0 \frac{\partial p}{\partial x} + \gamma p_0 \nabla \cdot \mathbf{V} = 0 \quad (2.2)$$

where ρ_0 , p_0 are the density and pressure of the mean flow and γ is the ratio of specific heats of the gas. Upon eliminating \mathbf{V} , the governing equation for p is,

$$\left(\frac{\partial}{\partial t} + u_0 \frac{\partial}{\partial x} \right)^2 p - a_0^2 \nabla^2 p = 0 \quad (2.3)$$

where $a_0 = (\partial p_0 / \partial \rho_0)^{1/2}$ is the speed of sound.

2.1.1 Cylindrical Test Cells

For cylindrical test cells, the natural coordinates to use are the cylindrical coordinates (r, ϕ, x) as shown in Figure 2.1. Equation (2.3) becomes,

$$\left(\frac{\partial}{\partial t} + u_0 \frac{\partial}{\partial x}\right)^2 p - a_0^2 \left(\frac{\partial^2 p}{\partial r^2} + \frac{1}{r} \frac{\partial p}{\partial r} + \frac{1}{r^2} \frac{\partial^2 p}{\partial \phi^2} + \frac{\partial^2 p}{\partial x^2} \right) = 0. \quad (2.4)$$

The normal mode solutions have the form,

$$p(r, \phi, x, t) = \text{Re} \left\{ \hat{p}(r) e^{i(kx + m\phi - \omega t)} \right\} \quad (2.5)$$

where $\text{Re}\{ \}$ is the real part of k , the axial wave number and m , an integer, is the azimuthal mode number; ω is the angular frequency. Substitution of (2.5) into (2.4) gives,

$$\frac{d^2 \hat{p}}{dr^2} + \frac{1}{r} \frac{d\hat{p}}{dr} + \left[\frac{(\omega - u_0 k)^2}{a_0^2} - k^2 - \frac{m^2}{r^2} \right] \hat{p} = 0. \quad (2.6)$$

The solution of (2.6), which is bounded at $r = 0$ is,

$$\hat{p} = A J_m \left[\left(\left(\frac{(\omega - u_0 k)^2}{a_0^2} - k^2 \right)^{\frac{1}{2}} \right) r \right] \quad (2.7)$$

where $J_m()$ is the m^{th} order Bessel function.

The boundary condition at the cylindrical surface is $V_r = 0$. By (2.1), this is equivalent to,

$$r = \frac{D}{2}, \quad \frac{d\hat{p}}{dr} = 0. \quad (2.8)$$

Let λ_{mn} be the n^{th} zero of the derivative J'_m ; i.e.,

$$J'_m(\lambda_{mn}) = 0, \quad n = 1, 2, 3, \dots \quad (2.9)$$

Thus, substitution of solution (2.7) into boundary condition (2.8) yields

$$\left[\left(\frac{(\omega - u_0 k)}{a_0} \right)^2 - k^2 \right]^{\frac{1}{2}} \frac{D}{2} = \lambda_{mn}$$

or

$$(1 - M_0^2)k^2 + 2M_0 \frac{\omega}{a_0 k} + \left(\frac{4\lambda_{mn}^2}{D^2} - \frac{\omega^2}{a_0^2} \right) = 0 \quad (2.10)$$

where $M_0 = u_0/a_0$ is the mean flow Mach number. Equation (2.10) relates k and ω . Such a relationship is called the dispersion relation. Dispersion relation governs wave propagation in a duct.

On solving (2.10) for k , one finds two solutions. They are,

$$k_{mn}^{\pm} = \frac{-M_0 \frac{\omega}{a_0} \pm \left[\frac{\omega^2}{a_0^2} - \frac{4\lambda_{mn}^2}{D^2} (1 - M_0^2) \right]^{\frac{1}{2}}}{(1 - M_0^2)} \quad (2.11)$$

where $m = 0, 1, 2, \dots$; $n = 1, 2, 3, \dots$. By (2.5), (2.7) and (2.11) the full solution is,

$$p(r, \phi, x, t) = \text{Re} \left\{ J_m \left(\frac{2\lambda_{mn} r}{D} \right) e^{im\phi - \omega t} \left[A_{mn} e^{ik_{mn}^+ x} + B_{mn} e^{ik_{mn}^- x} \right] \right\}. \quad (2.12)$$

Now, at the two open ends of the test cell, the perturbation pressure is small. Thus the appropriate boundary conditions are

$$x = 0, \quad x = L, \quad p = 0. \quad (2.13)$$

On imposing (2.13) on (2.12), it is straightforward to find,

$$B_{mn} = -A_{mn} \quad (2.14a)$$

and

$$e^{i(k_{mn}^+ - k_{mn}^-)L} = 1. \quad (2.14b)$$

The solution of (2.14b) is

$$(k_{mn}^+ - k_{mn}^-)L = 2\pi\ell, \quad \ell = 1, 2, \dots$$

By (2.11), this condition when written out in full is,

$$\frac{2 \left[\frac{\omega^2}{a_0^2} - \frac{4\lambda_{mn}^2}{D^2} (1 - M_0^2) \right]^{\frac{1}{2}} L}{(1 - M_0^2)} = 2\pi\ell.$$

Upon solving for ω , the normal mode frequencies are found to be,

$$\omega_{\ell,m,n} = a_0 (1 - M_0^2)^{\frac{1}{2}} \left[\frac{\ell^2 \pi^2}{L^2} + \frac{4\lambda_{mn}^2}{D^2} \right]^{\frac{1}{2}}. \quad (2.15)$$

2.1.2 Rectangular Test Cells

For test cells with a rectangular geometry of dimensions W by H by L as shown in Figure 2.1, a similar analysis as above leads to a dispersive relation in the form

$$(1 - M_0^2)k^2 + 2M_0 \frac{\omega}{a_0} k + \left[\left(\frac{n^2}{W^2} + \frac{m^2}{H^2} \right) \pi^2 - \frac{\omega^2}{a_0^2} \right] = 0 \quad (2.16)$$

where n and m are integers. The resonance (normal mode) frequencies are,

$$\omega_{\ell,m,n} = \left(\frac{n^2}{W^2} + \frac{m^2}{H^2} + \frac{\ell^2}{L^2} \right) \pi a_0 (1 - M_0^2)^{\frac{1}{2}} \quad (2.17)$$

where ℓ is an integer except zero.

2.2 High-Altitude Engine Test Cells

A high-altitude engine test cell forms a closed environment by itself. The geometry of some altitude test cells is fairly complex. The acoustic resonance frequencies of these test cells cannot

be written out in simple analytical forms. They can, however, be found computationally by CAA methods.

In some high-altitude test cells, a circular diffuser piece as shown in Figure 2.2 is sometimes used. Such a diffuser has resonance frequencies of its own. They can be found as follows.

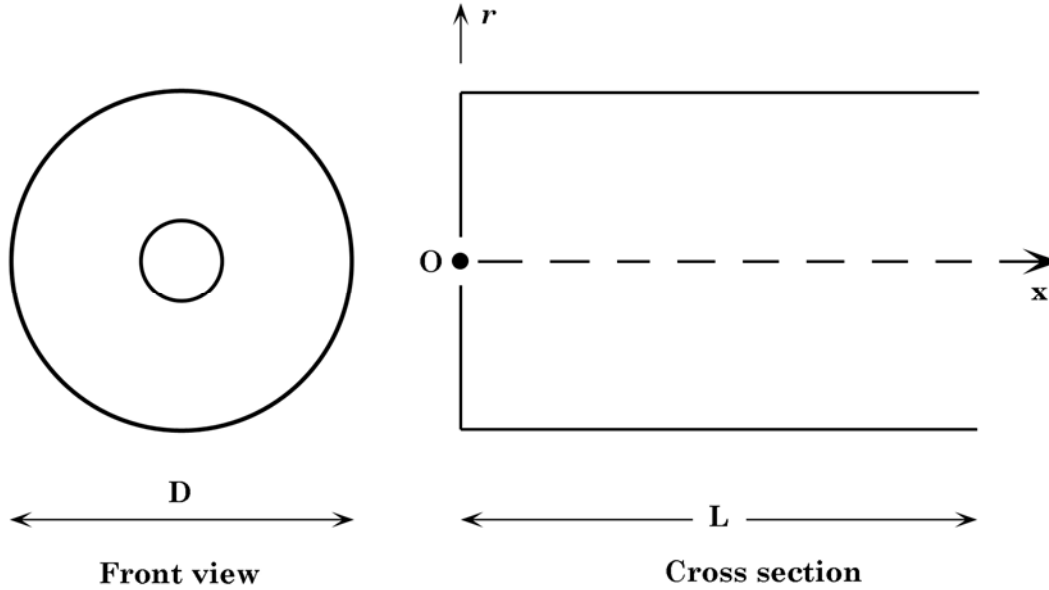


Figure 2.2. Schematic diagram of a diffuser with one open end and one nearly closed end.

Let us approximate the diffuser as a short cylindrical shell with one open and one closed end. The solution inside the cylindrical diffuser is still given by (2.12). But now, the end conditions are,

$$x = L, \quad p = 0, \quad (\text{open end}) \quad (2.18)$$

$$x = 0, \quad \frac{dp}{dx} = 0, \quad (\text{closed end}). \quad (2.19)$$

Upon imposing boundary condition (2.18) on (2.12) it is easy to find

$$A_{mn} e^{ik_{mn}^+ L} + B e^{ik_{mn}^- L} = 0. \quad (2.20)$$

Similarly, the imposition of boundary condition (2.19) on (2.12) gives

$$k_{mn}^+ A_{mn} + k_{mn}^- B_{mn} = 0.$$

By means of this relation and (2.20), it is straightforward to find,

$$k_{mn}^+ e^{-ik_{mn}^+ L} = k_{mn}^- e^{-ik_{mn}^- L} \quad (2.21)$$

With one end closed, the effective mean flow velocity should be small. Thus it is reasonable to set $M_0 = 0$ in calculating k_{mn}^\pm . This leads to

$$k_{mn}^+ = -k_{mn}^- = \left[\frac{\omega^2}{a_0^2} - \frac{4\lambda_{mn}^2}{D^2} \right]^{\frac{1}{2}}. \quad (2.22)$$

Thus (2.21) becomes

$$k_{mn}^+ \left[1 + e^{i \left[\frac{\omega^2}{a_0^2} - \frac{4\lambda_{mn}^2}{D^2} \right]^{\frac{1}{2}} L} \right] = 0. \quad (2.23)$$

The solution of (2.23) is

$$\left(\frac{\omega^2}{a_0^2} - \frac{4\lambda_{mn}^2}{D^2} \right)^{\frac{1}{2}} L = (2\ell + 1)\pi$$

where ℓ is an integer. On solving for ω , it is found,

$$\omega_{\ell,m,n} = a_0 \left[\frac{(2\ell + 1)^2 \pi^2}{L^2} + \frac{4\lambda_{mn}^2}{D^2} \right]^{\frac{1}{2}}. \quad (2.24)$$

$\omega_{\ell mn}$ as given by (2.24) are the normal mode frequencies of the cylindrical diffuser. They are also the acoustic resonance frequencies

Chapter 3. Interaction Noise

The insertion of a jet inside an engine test cell may lead to noise and tones that are generated by the coupling of the jet to the acoustic environment of the test cell. Such interaction could lead to resonances and super resonance. The energy source of these resonances is primarily the instabilities of the jet flow. These instabilities are excited by the acoustic modes of the test cell. The excitation process is generally referred to as receptivity. Jets are unstable only over a band of frequencies. The growth rate of instability waves at different frequencies within the band can vary significantly. When the most amplified instability wave frequency matches that of a duct mode of the test cell, very high amplitude resonance, called super resonance, could occur. This is most undesirable and destructive. It may render severe damage to the test facility.

3.1 Instabilities of High-Speed Jets

A jet is intrinsically unstable. That is, small perturbations imposed on a jet will have the natural tendency to grow to a substantial amplitude. A comprehensive study of the instabilities of high-speed jets has been carried out by Tam and Hu (1989). They found that these jets could support three families of instability waves. These instabilities have been observed by Oertel (1979, 1980, 1982). The three families of instabilities are the Kelvin-Helmholtz instability, the supersonic and subsonic instability waves. The supersonic and subsonic instability waves propagate with phase velocities that are supersonic and subsonic relative to ambient speed of sound. Of importance to engine test cell applications are the Kelvin-Helmholtz instability waves. These instability waves play a crucial role in providing energy to drive the feedback loop of jet screech tones, in the generation of Mach wave radiation and broadband shock noise, and in providing an energy source responsible for the occurrence of many engine test cell resonances.

Before embarking on an analysis of the instability wave modes of high-speed jets, it is found useful first to examine physically why these jets can support three distinct families of waves. Ackeret (see Liepmann & Puckett, 1947; Papamoschou & Roshko, 1986) was the first to provide a physical explanation of the mechanism responsible for the Kelvin-Helmholtz instability in a thin shear layer. Here it will be shown that Ackeret's physical argument can be extended to the

case of high-speed jets to explain why these jets can sustain three classes of waves. For the sake of completeness, Ackeret's explanation of the Kelvin-Helmholtz instability mechanism will be briefly reviewed.

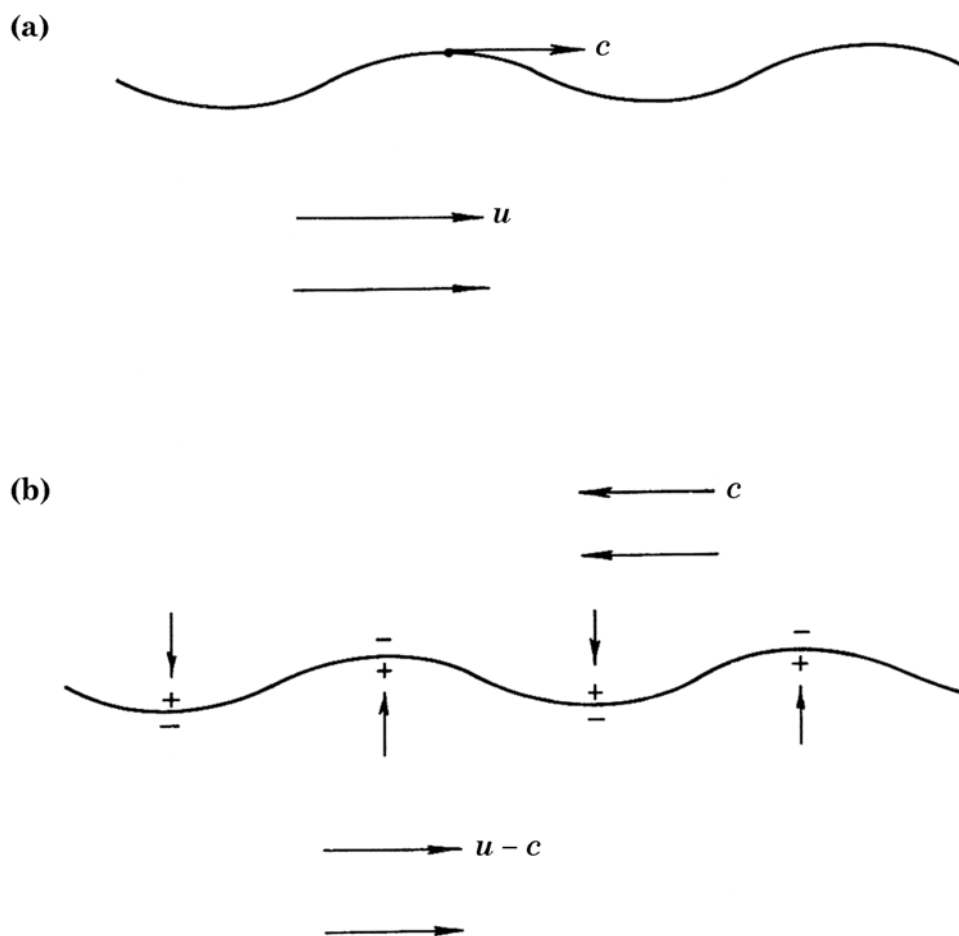


Figure 3.1. Kelvin-Helmholtz instability mechanism at a subsonic Mach number. +, high pressure region; -, low pressure region. (a) Stationary frame of reference. (b) Wave frame of reference.

Consider a two-dimensional vortex sheet separating a fluid at rest and a fluid moving at a subsonic velocity U . It will be assumed that the vortex sheet is deformed by a Kelvin-Helmholtz wave with a phase velocity c as shown in Figure 3.1(a). Ackeret suggested that one should view the flow, not in the stationary frame of reference, but in a moving frame traveling with the phase velocity c of the wave. In this wave frame the flow is as shown in Figure 3.1(b). Now for the flow above the vortex sheet, the vortex sheet may be regarded as a wavy wall. So within a quasi-

steady approximation, the flow is that of a uniform flow past a wavy wall. The solution of this problem is well known (see, e.g., Liepmann & Roshko, 1957, Ch. 8). At subsonic Mach number the pressure is lowest at the crests of the wavy wall and highest at the troughs. Similar consideration may also be applied to the flow below the vortex sheet. Again, the pressure is lowest at the crests and highest at the troughs. Since the crests and troughs interchange on the two sides of the vortex sheet, the result is that a net pressure imbalance would exist across the thin mixing layer in the quasi-steady approximation. This pressure imbalance is in phase with the vortex-sheet displacement and hence would tend to increase its amplitude leading to the well-known Kelvin-Helmholtz instability.

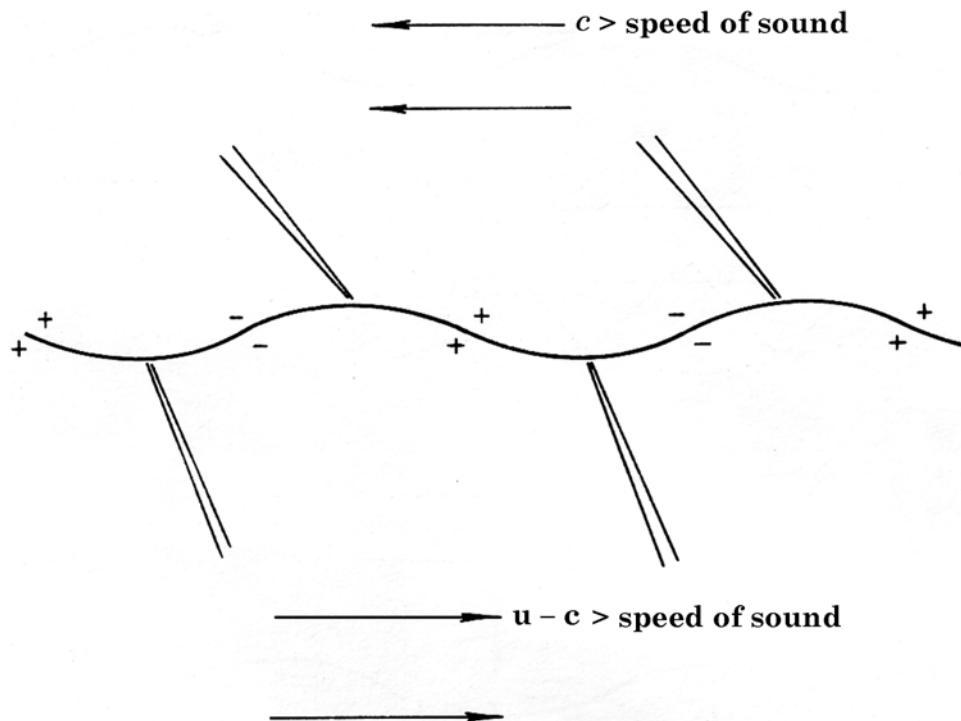


Figure 3.2. Pressure distribution on the two sides of a vortex sheet layer at supersonic convective Mach numbers as viewed in the wave frame of reference. +, high pressure region; -, low pressure region.

Now suppose the Mach number of the flow is highly supersonic so that in the wave frame of reference the flows on the two sides of the vortex sheet are supersonic as shown in Figure 3.2. For supersonic flow over a wavy wall it is known that the pressure distribution is no longer in phase but rather 90° out of phase with the displacement of the wall. This results in identical

pressure distribution on both sides of the vortex sheet. The net effect is that the wave becomes neutrally stable. This is in agreement with the prediction of Miles (1958) using hydrodynamic stability theory.

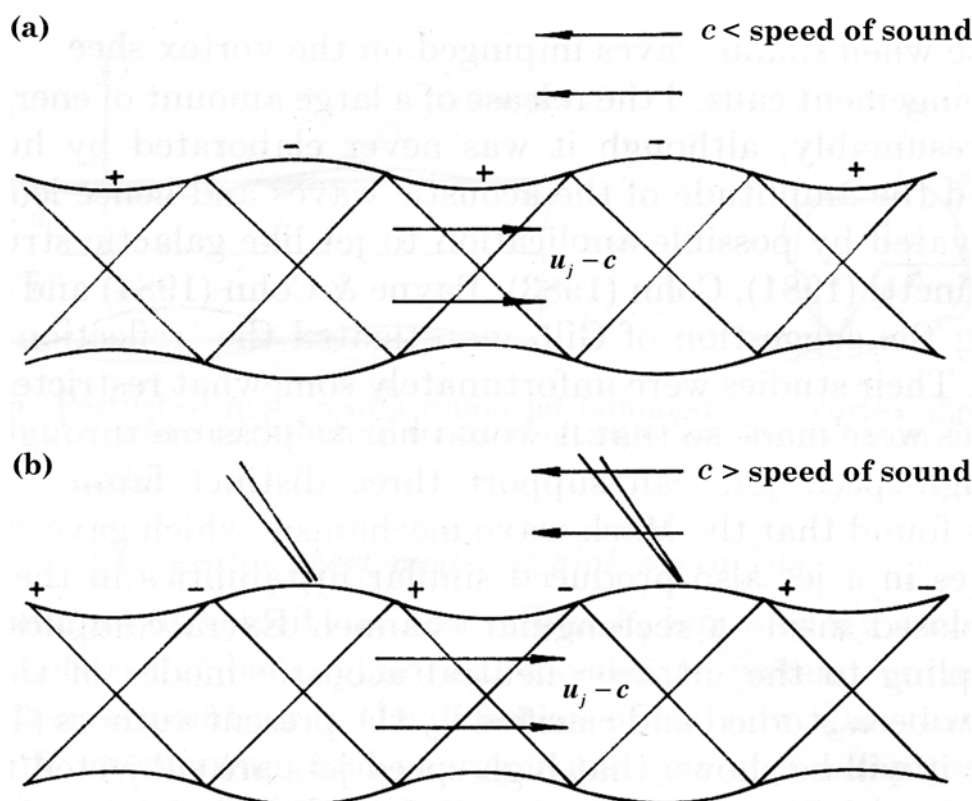


Figure 3.3. Pressure distribution on the outside surface of a cylindrical wavy vortex sheet jet as viewed in the wave frame of reference. Also shown is the Mach wave system inside the jet. (a) Subsonic flow outside. (b) Supersonic flow outside.

For circular jets the situation is somewhat different. The cylindrical vortex sheet that bounds the jet also tends to reflect acoustic disturbances that impinge on it. Thus, acoustic disturbances could be trapped inside the jet bouncing back and forth, forming a periodic Mach wave system as shown in Figure 3.3. The condition under which such a Mach wave system can exist is that in the wave frame of reference, the flow inside the jet is supersonic. Since acoustic disturbances can propagate upstream (the phase velocity c of the wave is negative in this case) or downstream (c is positive) relative to the flow of the jet, this type of Mach wave system exists in supersonic as well as subsonic jets as long as $u_j - c$ is greater than the speed of sound where u_j is the jet

velocity. Of course, for subsonic jets c would have to be negative, namely, the wave is an upstream propagating wave. The pressure distribution associated with a Mach wave system inside a cylindrical wavy wall can easily be calculated. It is easy to show that, depending on the wavelength, the pressure distribution may be 180° out of phase with the radial vortex-sheet displacement. The wave speed c may, however, be subsonic or supersonic relative to the ambient gas. Let us first consider the case of subsonic waves. In the wave frame of reference, the ambient flow is subsonic. The pressure distribution associated with subsonic flow outside a wavy cylinder is 180° out of phase with the radial displacement of the cylindrical wavy wall. Thus, by suitable choice of the wavelength of the Mach wave system, pressure balance on the two sides of the thin mixing layer of the jet is possible (see Figure 3.3(a)). This implies that the vortex-sheet jet can support a family of neutral waves. For supersonic jets it can be shown that if the effect of finite mixing-layer thickness is included, this family of waves is actually unstable. Clearly, with subsonic phase velocity relative to the ambient gas, the amplitudes of these waves must decay exponentially in the radial direction outside the jet. In other words, the disturbances associated with this family of waves are confined mainly inside the jet. These subsonic waves are the third family of waves observed by Oertel (1980). To distinguish the waves of this family from the other two, there will be referred to as the subsonic (instability) waves.

For very high-speed jets, the phase velocity, c , of the Mach wave system may become supersonic relative to the ambient gas. In this case, the flow is supersonic both inside and outside the jet with respect to the wave frame as shown in Figure 3.3(b). The pressure distribution associated with a steady supersonic flow over a cylindrical wavy wall can be easily determined. On comparing the pressure distribution formulae inside and outside the cylindrical vortex sheet, it is evident that pressure balance is impossible regardless of the choice of wavelength. Hence, unlike the case of subsonic waves, no neutral waves are possible. Further, it is easy to show that for certain wavelengths a pressure imbalance, which is in phase with the vortex-sheet, displacement is possible. The net result is that with the internal Mach wave system a highly supersonic jet can sustain a family of instability waves with supersonic phase velocities. With supersonic phase velocity relative to the ambient gas, the instability wave will generate a Mach-wave-like near field as discussed by Tam (1971) and Chan & Westley (1973).

In the past, numerous studies of the Kelvin-Helmholtz instability waves of compressible jets have been carried out. References to some of these works can be found in Michalke (1984), Tam

& Burton (1984), Zaninetti (1986, 1987) and others. Most of these investigations, however, focused primarily on the Kelvin-Helmholtz instability in subsonic and low supersonic jets. In this primer, a vortex-sheet jet model as well as a more realistic jet model with continuous velocity profile and finite shear-layer thickness will be considered. Experience indicates that the simpler vortex-sheet model can usually provide reasonably good estimates of the phase velocity of an instability wave. But for the purpose of calculating accurately the growth rate of the wave, a finite-thickness jet model is necessary.

3.1.1 Vortex-Sheet Model of High-Speed Jets

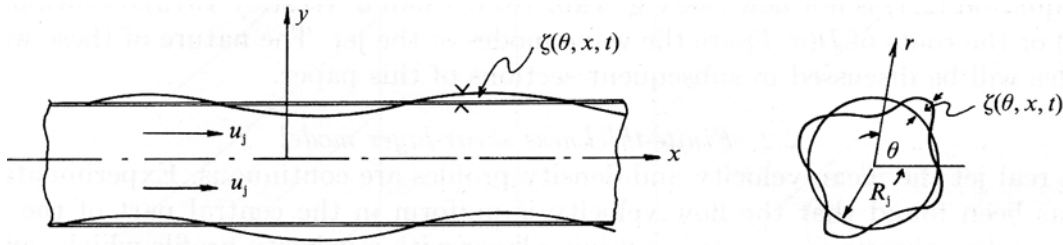


Figure 3.4. Perturbed motion of a round jet bounded by a vortex sheet.

Consider a supersonic jet of velocity u_j and radius R_j bounded by a vortex sheet as shown in Figure 3.4. Let (r, θ, x) be a cylindrical coordinate system centered at the axis of the jet with the x -axis pointing in the direction of the flow. On starting from the linearized continuity, momentum and energy equations of a compressible inviscid fluid, it is straightforward to find that the pressure associated with small-amplitude disturbances superimposed on the mean flow inside and outside the jet, p_i and p_o , are governed by the wave and convective wave equation, respectively.

$$\frac{\partial^2 p_o}{\partial t^2} - a_o^2 \nabla^2 p_o = 0 \quad (r \geq R_j), \quad (3.1)$$

$$\left(\frac{\partial}{\partial t} + u_j \frac{\partial}{\partial x} \right)^2 p_i - a_j^2 \nabla^2 p_i = 0 \quad (r \leq R_j), \quad (3.2)$$

where a_o and a_j (subscripts o and j denote physical quantities outside and inside the jet) are the speeds of sound outside and inside the jet. Let $\zeta(\theta, x, t)$ be the radial displacement of the vortex sheet. The dynamic and kinematic boundary conditions at the vortex sheet $r = R_j$ are

$$p_i = p_o, \quad (3.3)$$

$$-\frac{1}{\rho_o} \frac{\partial p_o}{\partial r} = \frac{\partial^2 \zeta}{\partial t^2}, \quad (3.4)$$

$$-\frac{1}{\rho_j} \frac{\partial p_i}{\partial r} = \left(\frac{\partial}{\partial t} + u_j \frac{\partial}{\partial x} \right)^2 \zeta. \quad (3.5)$$

It is straightforward to find that separable solutions of the above equations and boundary conditions that also satisfy the boundedness condition at $r = 0$ and $r \rightarrow \infty$ are

$$\begin{pmatrix} p_o \\ p_i \end{pmatrix} = \begin{pmatrix} H_n^{(1)}(i\eta_o r) \\ \frac{H_n^{(1)}(i\eta_o R_j) Y_n(i\eta_i r)}{J_n(i\eta_i R_j)} \end{pmatrix} e^{i(kx + n\theta - \omega t)}, \quad (3.6)$$

where $\eta_o = (k^2 - \omega^2 / a_o^2)^{1/2}$, $\eta_i = ((\omega - u_j k)^2 / a_j^2 - k^2)^{1/2}$. The branch cuts of η_o and η_i are taken to be

$$-\frac{1}{2}\pi < \arg \eta_o \leq \frac{1}{2}\pi, \quad 0 \leq \arg \eta_i < \pi.$$

The wave number and angular frequency k and ω are related by the eigenvalue relation

$$D(\omega, k) \equiv \frac{i\eta_o}{\rho_o \omega^2} J_n(\eta_i R_j) H_n^{(1)'}(i\eta_o R_j) - \frac{\eta_i}{\rho_j (\omega - u_j k)^2} H_n^{(1)}(i\eta_o R_j) Y_n'(\eta_i R_j) = 0, \quad (3.7)$$

(' = derivative).

Equation (3.7) is not new (see, e.g.; Tam, 1971; Chan & Westley, 1973). Solutions of (3.7) or the roots of $D(\omega, k)$ are the wave modes of the jet. The nature of these wave modes will be discussed later.

3.1.2 Finite Thickness Shear Layer Model

In a real jet the mean velocity and density are continuous. Experimentally it has been found that the flow velocity is uniform in the central part of the jet. Surrounding this uniform core is a mixing layer with a velocity profile that can be closely approximated by a half-Gaussian function (see, e.g.; Troutt & McLaughlin, 1982). Thus, the mean velocity profile in the core region of the jet will be taken as

$$\bar{u} = \begin{cases} u_j, & r < h, \\ u_j \exp\left[-(\ln 2)\left(\frac{r-h}{b}\right)^2\right], & r \geq h, \end{cases} \quad (3.8)$$

in the present calculation. In (3.8) h is the radius of the uniform core and b is the half-width of the jet mixing layer. The parameters h and b are related by the condition of conservation of momentum flux

$$\int_0^\infty \bar{\rho} \bar{u}^2 r \, dr = \frac{1}{2} \rho_j u_j^2 R_j^2. \quad (3.9)$$

The mean density $\bar{\rho}$ is related to the mean velocity \bar{u} by the Crocco's relation (Prandtl number is assumed to be unity).

It is easy to show, starting from the linearized equations of motion for an inviscid, non-conducting compressible fluid, that the equation governing the perturbation pressure p is (see, e.g., Tam & Burton, 1984)

$$p(r, \theta, x, t) = \hat{p}(r) \exp[i(kx + n\theta - \omega t)], \quad (3.10)$$

$$\frac{d^2 \hat{p}}{dr^2} + \left[\frac{1}{r} - \frac{1}{\bar{\rho}} \frac{d\bar{\rho}}{dr} + \frac{2k}{\omega - \bar{u}k} \frac{d\bar{u}}{dr} \right] \frac{d\hat{p}}{dr} + \left[\frac{(\omega - \bar{u}k)^2}{\bar{a}^2} - \frac{n^2}{r^2} - k^2 \right] \hat{p} = 0, \quad (3.11)$$

where $\bar{a} = (\gamma p_o / \bar{\rho})^{1/2}$. The locally parallel flow approximation has been invoked in deriving (3.11). This equation, together with the boundedness condition at $r=0$ and $r \rightarrow \infty$ form an eigenvalue problem for $\omega = \omega(k)$ or $k = k(\omega)$. The eigenvalue can be determined by integrating this equation numerically. Details of the numerical procedure may be found in Tam & Burton (1984) and will not be elaborated here. To initiate the iteration cycle of the numerical procedure the solution of the vortex-sheet jet model may be used.

3.1.3 Existence of Three Families of Wave Solutions

The branch points of the function η_o and η_i of (3.6) for a given real value of k in the complex ω -plane are,

$$\omega = \pm k a_o, \quad \omega = k a_j \left(\frac{u_j}{a_j \pm 1} \right), \quad (3.12)$$

respectively. The branch cuts of these functions are shown in Figure 3.5. The significance of the branch points is that regions of the complex ω -plane to the left of the left-hand branch point represent waves for which the flow has supersonic convective Mach number. Convective Mach number is defined as the Mach number of the flow measured in the moving frame of the wave. It is straightforward to show that for every point in this region of Figure 3.5(b) the supersonic convective Mach number relationship $u_j - \omega_r/k > a_j$ holds ($\omega = \omega_r + i\omega_i$), where subscripts r and i denote real and imaginary parts. Similarly, for every point to the left of the left-hand branch point of $i\eta_o$ in Figure 3.5(a), which is for the static environment outside the jet, the inequality $|\omega_r/k| > a_o$ applies.

It is also easy to show that points in the region of the complex ω -plane to the right of the right-hand branch points in Figure 3.5 again represent waves for which the convective Mach number of the flow is supersonic. In this case the inequalities are,

$$\frac{\omega_r}{k - u_j} > a_j, \quad \frac{\omega_r}{k} > a_o,$$

inside and outside the jet, respectively. The remaining region of the complex ω -plane, namely, the vertical strip between the two branch points, represents waves having subsonic convective Mach numbers.

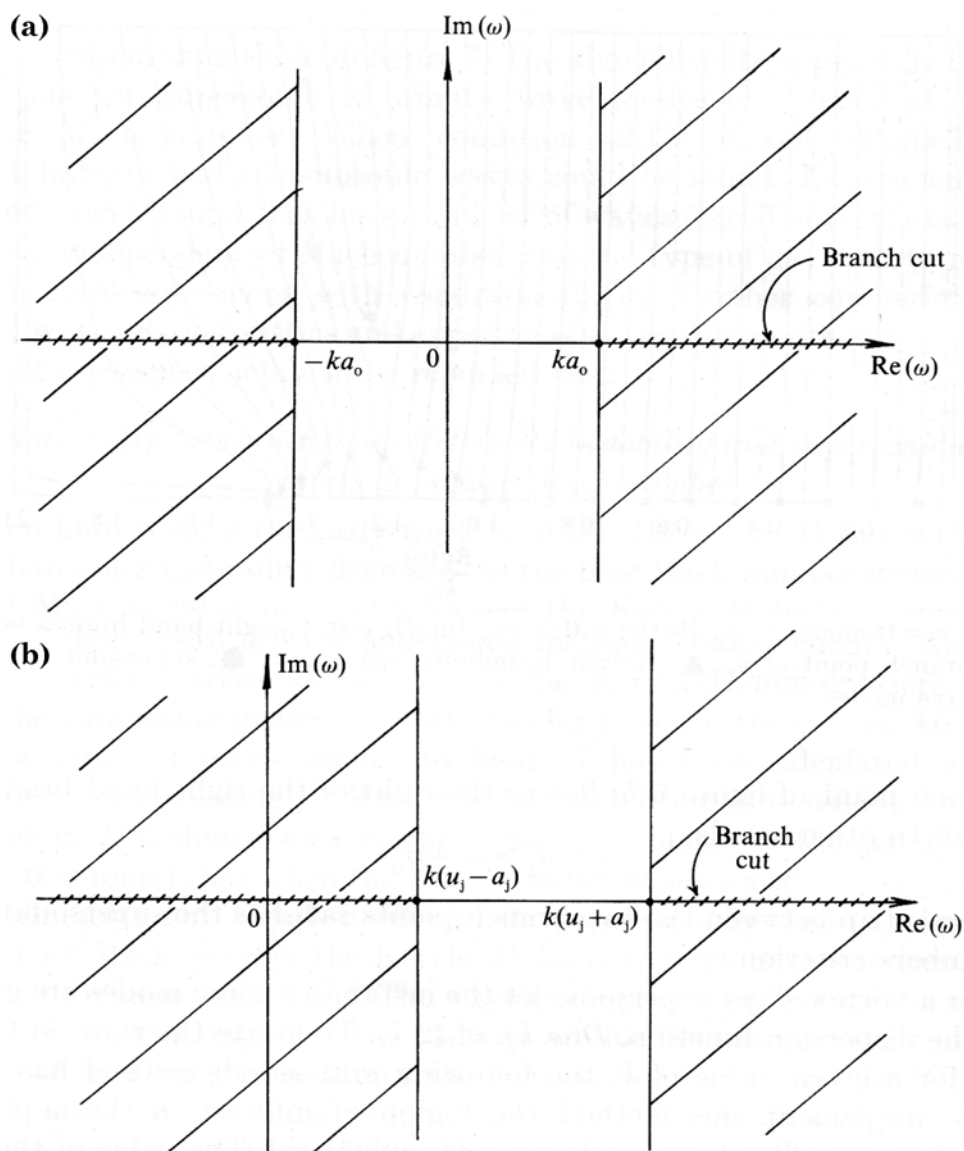


Figure 3.5. Branch cuts of (a) $i\eta$ and (b) η_1 in the complex ω -plane for a supersonic jet. Shaded areas are regions with supersonic convective Mach number.

According to the instability mechanism described in the previous section, supersonic instability waves exist in a jet only if the convective Mach numbers (for the flow inside and

outside the jet) are supersonic. In terms of the complex ω -plane, this is possible only if the jet Mach number is highly supersonic such that the left-hand branch point of Figure 3.5(b) lies to the right of the right-hand branch point of Figure 3.5(a). In other words,

$$u_j > a_j + a_o. \quad (3.13)$$

The vertical strip between the two branch points satisfies the supersonic convective Mach numbers criterion.

Now for a vortex-sheet supersonic jet the instability wave modes are given by the zeros of the dispersion function, $D(\omega, k)$, of (3.7). To locate the zeros in the complex ω -plane for a given value of k , the following grid-search method has been found useful. To implement this method the region of interest in the ω -plane is first subdivided into small subregions by a rectangular grid. The values of the dispersion function $D(\omega, k)$ of (3.7) are calculated at each grid point. A plotting subroutine is then called that performs a two-dimensional interpolation of this set of values and constructs the two families of curves $\text{Re}(D) = 0$ and $\text{Im}(D) = 0$. The intersection of these curves provides a first estimate of the locations of the zeros of D . These values are then refined by applying Newton's iteration method.

Figure 3.6 shows a typical example of the zeros of the dispersion function $D(\omega, k)$ found by the grid-search method for a high supersonic jet. In this example, the axisymmetric waves ($n = 0$) of a Mach number 4.0 cold jet are considered. The wave number kR_j has been set to be equal to 15.0 in the calculation. It is evident in this figure that there are three families of zeros, or wave modes. The isolated zero with the largest temporal growth rate is the familiar Kelvin-Helmholtz instability. Immediately below the Kelvin-Helmholtz zero is a family of zeros lying in the vertical strip (with $\text{Im}(\omega) > 0$) between the right-hand branch point of $i\eta_o$ and the left-hand branch point of η_i . These are the supersonic instability waves. To the left of the supersonic instability waves is another family of zeros. These zeros lie on the real ω -axis between the two branch points $\omega/k = \pm a_0$. These waves, therefore, have subsonic phase velocity relative to the ambient speed of sound. They are the subsonic waves. For non-axisymmetric wave modes with $n = 1, 2, 3, \dots$, maps similar to Figure 3.6 have been constructed by the grid-search method. Again they exhibit three sets of wave modes resembling those in Figure 3.6. The above results

apply to hot jets as well. For hot jets, the supersonic instability wave modes exist even at a much lower supersonic Mach number. When condition (3.13) is not satisfied, only the Kelvin-Helmholtz and the subsonic waves could be found. Experimentally, Oertel (1979, 1980, 1982) found that his second set of waves (the W waves) exist only when $u_j > a_j + a_o$, independent of Mach number and the type of gas used to form the jet. This is in total agreement with condition (3.13).

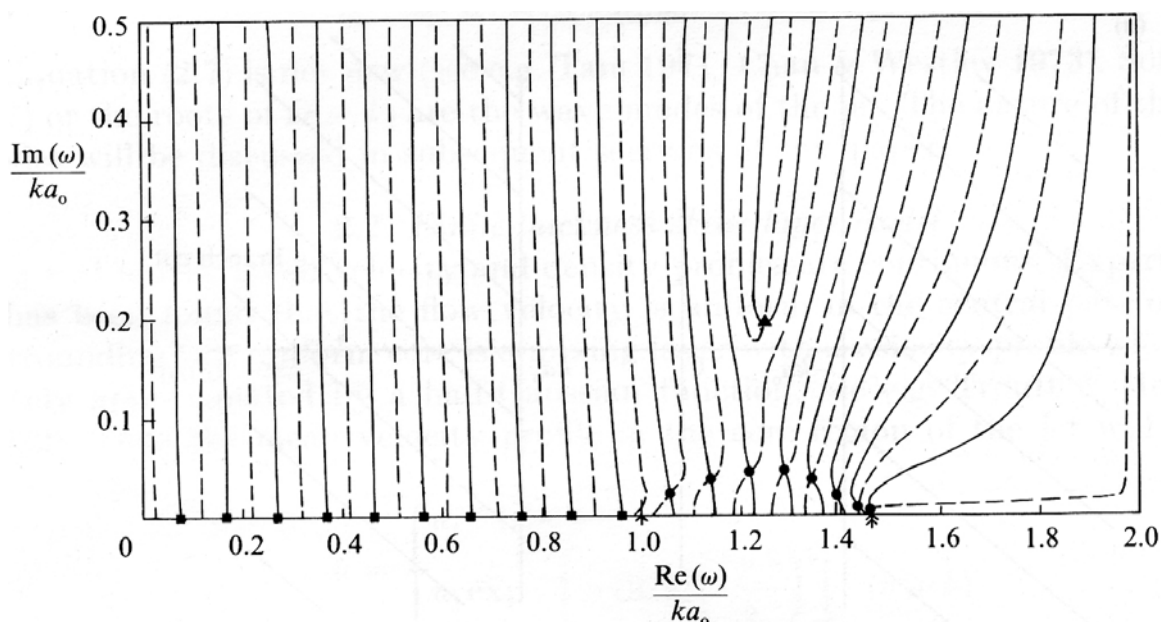


Figure 3.6. Zeros of the dispersion function $D(\omega, k)$ in the complex ω -plane. $M_j = 4.0$, cold jet, $kR_j = 15.0$, $n = 0$ mode. —, $\text{Re}(D) = 0$; ---, $\text{Im}(D) = 0$. \uparrow , right-hand branch point of η_o , \uparrow , right-hand branch point of η_1 . \blacktriangle , Kelvin-Helmholtz instability; \bullet , Supersonic instabilities; \blacksquare , Subsonic wave modes.

3.2 Resonances

Resonances occur when there is a build-up of intense oscillations at a discrete frequency. This is possible when two criteria are met. First, there is a mechanism to trap acoustic energy in the system at the particular frequency. Second, there must be a source of energy that feeds into the system. For an engine test cell, the normal modes of the system allow energy to be kept in the system. Energy at frequencies other than the normal mode frequencies are leaked out or radiated away. Thus, the normal mode frequencies are the possible resonance frequencies. But in order

for resonance to occur, energy at the resonance frequency must be supplied to the system. In the case of engine test cells, a good source of energy is the instabilities of the jet flows. However, jet instabilities are confined to restricted bands of frequencies. Hence, engine test cell resonance tones can be observed when there is an overlap between a frequency band of the jet instability wave and the normal mode frequencies of the test cell. Since a test cell may have infinitely many normal modes, it follows that resonance does not occur at all normal mode frequencies; only at those that lie within the unstable frequency range of the jet flow.

For long ducts, the dispersion relation of the duct modes is given by (2.10) for a circular duct and (2.11) for rectangular ducts. These duct modes have a propagation speed equal to the group velocity $d\omega/dk$. The group velocity can be found by differentiating the dispersion relation with respect to k . Thus, for a circular duct, the dispersion relation and group velocity for the duct modes are,

$$(1 - M_0^2)k^2 + 2M_0 \frac{\omega}{a_0} k + \left(\frac{4\lambda_{mn}^2}{D^2} - \frac{\omega^2}{a_0^2} \right) = 0, \quad (3.14)$$

$$\frac{d\omega}{dk} = - \frac{a_0 \left[(1 - M_0^2)k + \frac{M_0 \omega}{a_0} \right]}{\left(\frac{M_0 k - \omega}{a_0} \right)}. \quad (3.15)$$

The duct modes with zero group velocity have the significance that they will not propagate away once they are generated. Energy fed into these modes will, therefore, stay locally. Their amplitude could build up into violent oscillations if there is a continuous input of energy. Thus, these wave modes may also lead to resonance.

By setting $d\omega/dk = 0$, it is easy to find from (3.15),

$$k = - \frac{M_0 \omega}{a_0 (1 - M_0^2)}. \quad (3.16)$$

However, k and ω of a duct mode are related by the dispersion relation (3.14). Hence, on substituting (3.16) into (3.14), it is simple to find the frequencies of the zero group velocity resonances. They are,

$$\omega = 2a_0(1 - M_0^2)^{\frac{1}{2}} \frac{\lambda_{mn}}{D}. \quad (3.17)$$

Similarly, for long rectangular ducts, the zero group velocity resonance frequencies are,

$$\omega = a_0(1 - M_0^2)^{\frac{1}{2}} \pi \left(\frac{n^2}{W^2} + \frac{m^2}{H^2} \right)^{\frac{1}{2}}. \quad (3.18)$$

3.3 Receptivity

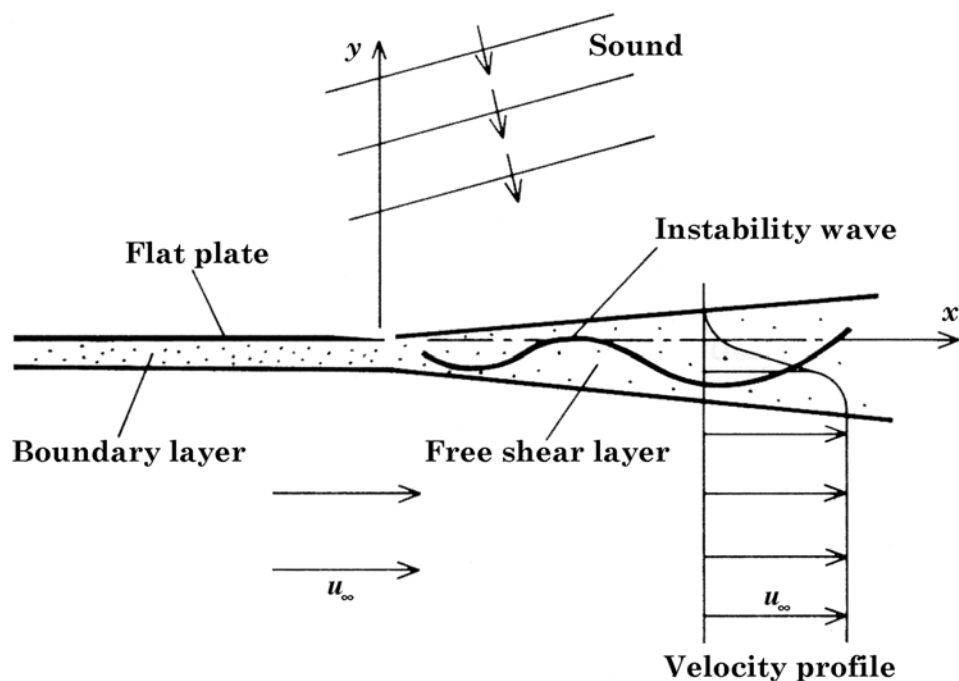


Figure 3.7. Excitation of shear layer instability waves by sound.

In the literature, there are a number of experimental and theoretical investigations (e.g.: Ahuja *et al.*, 1982, 1984) aiming specifically at obtaining a fundamental understanding of the processes by which external sound waves excite the intrinsic instability waves in shear flows. These studies were motivated by possible applications of the acquired knowledge to separated flow control by sound (Ahuja *et al.*, 1982, 1984) tone excited jets and shear layers (Tam, 1978; Ahuja *et al.*, 1982; Bechert, 1983; Lepicovsky *et al.*, 1982; and Tam *et al.*, 1985) and sound-instigated boundary layer instability and transition (Shapiro, 1977; Murdock, 1980). The purpose of the discussion here is to provide a simple physical picture of the excitation processes or receptivity. The simple physical picture described here should complement the mathematical theory developed in Tam (1978), Tam and Morris (1985) and Tam (1981).

Let us consider the excitation of the instability waves of a two-dimensional free shear layer by sound as shown in Figure 3.7. For convenience, the two-dimensional free shear layer may be regarded to form downstream of the trailing edge of a flat plate. Under normal circumstances, the nature and physical characteristics of the acoustic waves and the shear layer instability waves are so different that the two types of waves do not interact with each other at all. In other words, in the case of Figure 3.7 one expects that part of the incident acoustic waves will be transmitted through the two-dimensional free shear layer and part of it will be reflected back, but no excitation of the intrinsic instability waves would take place. In order that coupling of the two waves would occur as the sound waves pass through the shear layer, certain physical prerequisites must be satisfied. The necessary conditions are as follows: (1) matching of the frequencies of the incident sound wave and the excited instability wave; (2) matching of the phase velocities (in the flow direction) of the two waves. The first condition is easy to understand since it is natural to expect the excited instability wave to have the same frequency as the incident sound wave. To understand the second condition it is best to consider an observer traveling with the instability wave. If the phase velocities of the waves are different than in the moving frame of reference the observer will see the sound wave travel past by him. During half a period the sound wave amplitude is positive and the other half period is negative. The net result is that over a period of oscillation any interaction between the two waves will be cancelled out to zero. The situation is totally different, however, if the two waves travel with exactly the same phase speed in the flow direction. No cancellation would take place and the two waves would have a long time to communicate and to interact with each other. It is to be noted that the phase

velocity of a wave is equal to the frequency divided by the wave number. Therefore, necessary condition (2) may be restated in terms of the wave numbers; that is, to excite the instability waves of a flow by sound there must be a matching of the wave numbers of the two kinds of waves.

Let us now pursue these necessary conditions further to see under what circumstances they can be fulfilled. In general, the pressure, p_i , associated with an instability wave of frequency ω (see Figure 3.7) may be represented by

$$p_i(x, y, t) = f(y) e^{i(\alpha_i x - \omega t)}, \quad (3.19)$$

where α_i is the wave number and $f(y)$ is the amplitude distribution across the shear layer. Similarly the pressure field of the incident sound wave, p_s , may be represented by

$$p_s(x, y, t) = B g(y) e^{i(\alpha_s x - \omega t)}, \quad (3.20)$$

where α_s is the wave number (in the x -direction) and B is the amplitude of the sound wave. Here $g(y)$ is included to allow for possible variation of the incident sound wave amplitude and phase in the y -direction. Under normal conditions, α_i and α_s are very different, and thus the phase velocities of the waves are also very different, and there should be very little interaction between the two waves. Now if the amplitude B of the sound wave is not a constant but varies rapidly in the x -direction, the situation changes drastically. Instead of (3.20) the expression for the sound pressure, p_s , becomes

$$p_s(x, y, t) = B(x) e^{i(\alpha_s x - \omega t)} g(y) = \int_{-\infty}^{\infty} \tilde{B}(k) e^{i[(k + \alpha_s)x - \omega t]} dk g(y). \quad (3.21)$$

In (3.21) $\tilde{B}(k)$ is the Fourier transform of the spatially varying amplitude $B(x)$. As can easily be seen, the sound wave may be regarded as a superposition of many wave components with the wave number $(k + \alpha_s)$. The wave number spectrum is no longer discrete (see Figure 3.8(a)) as in the case of constant amplitude. It is broadband as depicted in Figure 3.8(b). With rapid enough

amplitude variation the wave number spectrum of the incident sound wave could be very broad; broad enough to overlap the wave number of the instability wave. When this occurs, as is shown in Figure 3.8(b), the necessary conditions for the excitation of the shear layer instability wave are met and strong coupling of the two types of waves is expected.

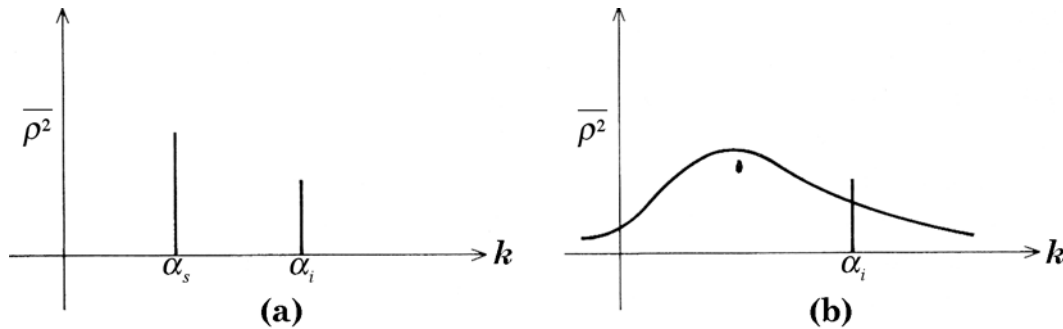


Figure 3.8. Broadening of wave number spectrum by amplitude variation. (a) Constant amplitude; (b) strong amplitude variation.

Consider now the case of tone-excited jets as shown in Figure 3.9. Without loss of generality, we will assume that the incident acoustic waves are from an external source outside the jet. The arguments presented below, however, would apply to internal acoustic disturbances coming out of the nozzle exit as well. On emerging from the nozzle exit, the jet flow consists of a uniform core surrounded by a mixing layer with inflexional velocity profile. Such a velocity profile supports a band of instability waves. From the standpoint of the inflexional instability waves, the amplitude of the incident sound wave rises rapidly near the nozzle exit to an approximately constant value slightly downstream as shown in the lower portion of Figure 3.9. Thus, there is a very abrupt amplitude variation of the forcing function. Such rapid changes, as is well known, produce an extremely broadband wave number spectrum. This spectrum easily overlaps that of the instability waves. Hence, the wave number matching condition is fulfilled and strong excitation of the instability waves by the incident sound waves takes place in the immediate vicinity downstream of the nozzle exit. This physical reasoning provides readily an explanation to the well-known experimental fact that shear layers are most susceptible to acoustic excitation downstream of a trailing edge.

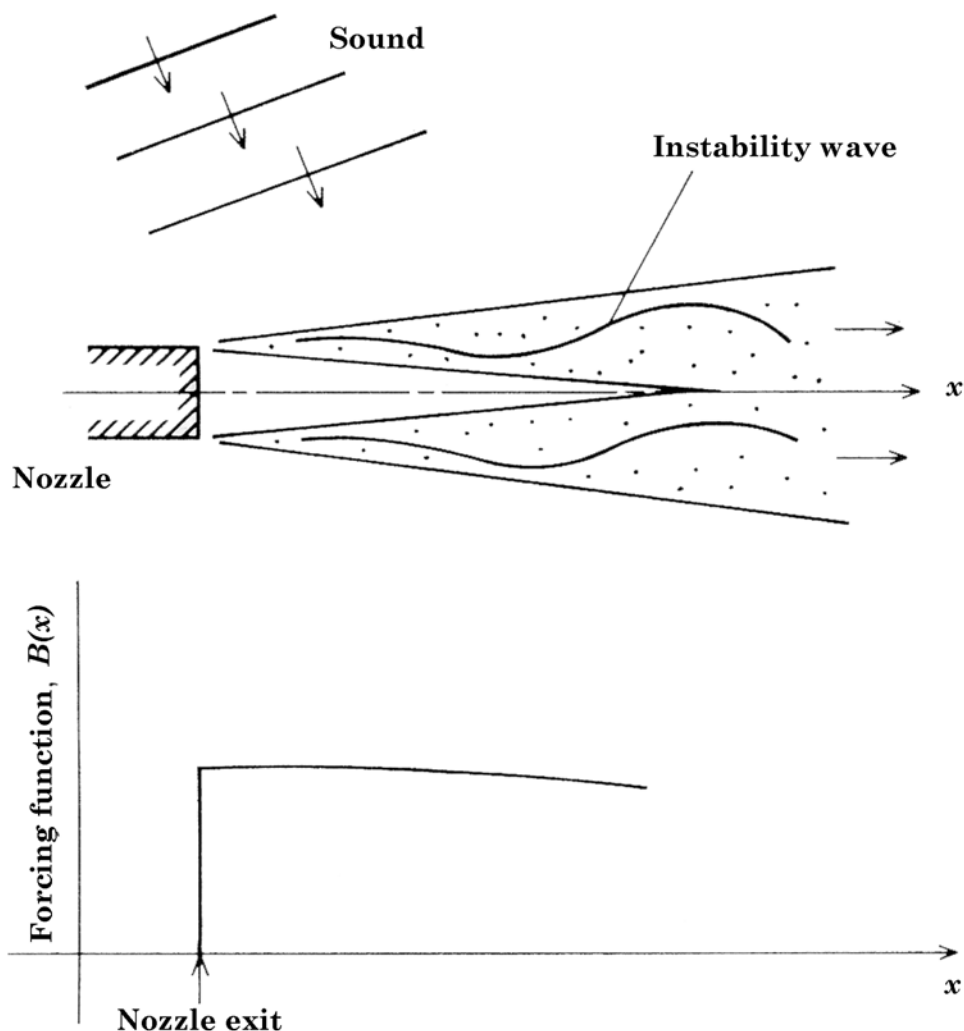


Figure 3.9. Forcing function as seen by the instability waves of a tone excited jet.

In the above, we have discussed how the wave number matching condition can be satisfied when there is a rapid amplitude variation of the incident sound waves. This is, of course, not the only way by which this necessary condition can be satisfied. It is easy to see this condition can again be met if, instead of having the amplitude of the incident sound wave varying, one can have a rapid spatial change in the mean flow velocity profile. In flow regions where this is realized, the instability wave characteristics, including the wave number, must undergo very rapid spatial changes also. Thus, the wave number spectrum of an instability wave of a fixed frequency is broadband. It is not difficult to visualize that the broadening of the instability wave number spectrum by mean flow variation could be sufficient to overlap with that of the incident

sound wave. In this way wave number matching can again be accomplished and strong excitation of the instability wave ensues. This type of flow condition occurs in shear layers near flow separation regions such as in the upper surfaces of airfoils at high angle of attack. The experiments of Ahuja *et al.* (1983, 1984) are excellent examples.

3.4 Amplified Instability Wave Spectrum

A high-speed jet is unstable only over a finite range of frequencies. As the instability waves of the jet are the energy source of resonance tones it follows that the tone frequencies must lie within the unstable frequency band. Linear instability wave theory indicates that the growth rate of a wave depends on its frequency, the shear layer thickness or the mean velocity profile, the jet Mach number and temperature, and the azimuthal mode number. Thus, waves at different frequencies will be amplified differently. The wave with the largest amplification or total growth would attain the highest amplitude, hence it would most likely generate a tone of the highest intensity. Here the characteristics of the amplified instability wave spectrum are discussed.

Linear instability wave theory is now a relatively well-established subject. The mathematical and computational procedure needed to determine the spatial growth rates of these waves are fully documented in the literature (see, e.g., Tam *et al.*, 1984, 1989).

A good approximation of the mean flow velocity profile of a jet is given by (3.8) and (3.9). The density $\bar{\rho}$ is related to the mean velocity \bar{u} through the Crocco's relation. The explicit relation is,

$$\frac{\rho_i}{\bar{\rho}} = \left(1 + \frac{\gamma-1}{2} M_j^2\right) \left[\frac{T_a}{T_r} + \left(1 - \frac{T_a}{T_r}\right) \frac{\bar{u}}{u_j} \right] - \frac{\gamma-1}{2} M_j^2 \left(\frac{\bar{u}}{u_j} \right)^2 \quad (3.22)$$

where T_a and T_r are the ambient and reservoir temperatures, respectively.

Insertion of the mean flow quantities into (3.11) leads to an eigenvalue problem. The governing equation is (3.11). The boundary conditions are,

$$r = 0, \quad \hat{p} \text{ is finite}$$

$$r \rightarrow \infty, \quad \hat{p} \rightarrow 0.$$

For a given frequency instability wave, k is the eigenvalue. The negative value of the imaginary part of k or $-k_i$ is the local growth rate of the instability wave. As the wave propagates downstream it sees a continuous change in the mean velocity and density profiles. Its spatial growth rate, therefore, changes as well. For a wave with a fixed frequency f or Strouhal number, $S = fD_j/U_j$, and azimuthal mode number n in a supersonic jet of Mach number M_j and temperature ratio T_r/T_a , the total amplification $A(S, n, M_j, T_r/T_a)$ is given by

$$A\left(S, n, M_j, \frac{T_r}{T_a}\right) = \exp\left[-\int_0^{x_c} k_i(x) dx\right] \quad (3.23)$$

where x_c is the location at which the wave reaches its maximum amplitude or the local growth rate is zero. Extensive experimental data indicate that b varies nearly linearly with x . That is, $db/dx = \sigma$ is a constant. By means of the linear relationship between b and x , the total growth integral on the right side of (3.23) may be rewritten in the dimensionless form (except for a factor σ)

$$I = -\int_{\frac{b_0}{R}}^{\frac{b_c}{R}} k_i\left(\frac{b}{R}\right) R d\left(\frac{b}{R}\right) \quad (3.24)$$

where b_0 is the half width of the mixing layers at the nozzle exit and $b_c = b(x_c)$.

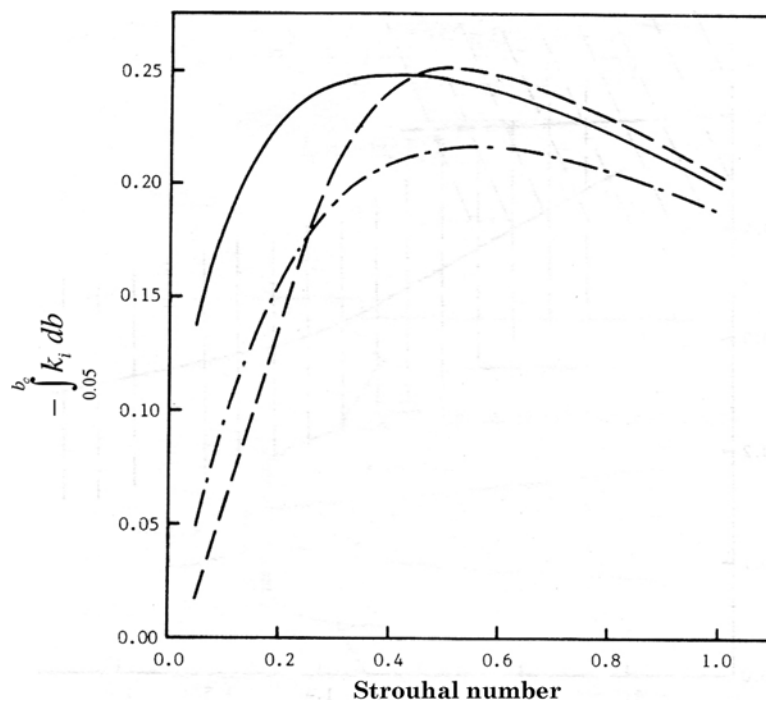


Figure 3.10. Total growth integral of the instability waves of a Mach 1.1 (cold) supersonic jet as a function of Strouhal number (fD_j/U_j): --- $n = 0$; — $n = 1$; and - · - · - $n = 2$ mode.

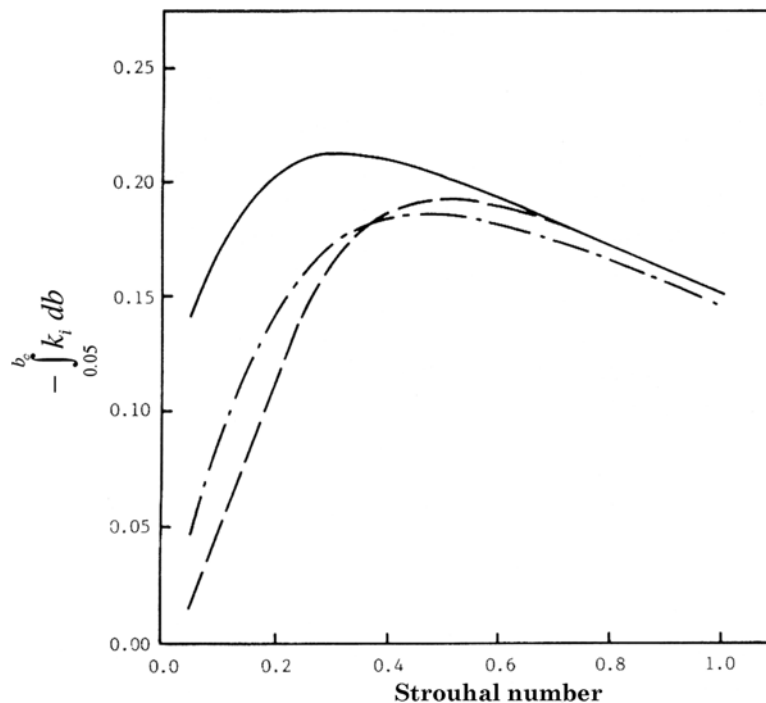


Figure 3.11. Total growth integral of the instability waves of a Mach 1.4 (cold) supersonic jet as a function of Strouhal number: --- $n = 0$; — $n = 1$; and - · - · - $n = 2$ mode.

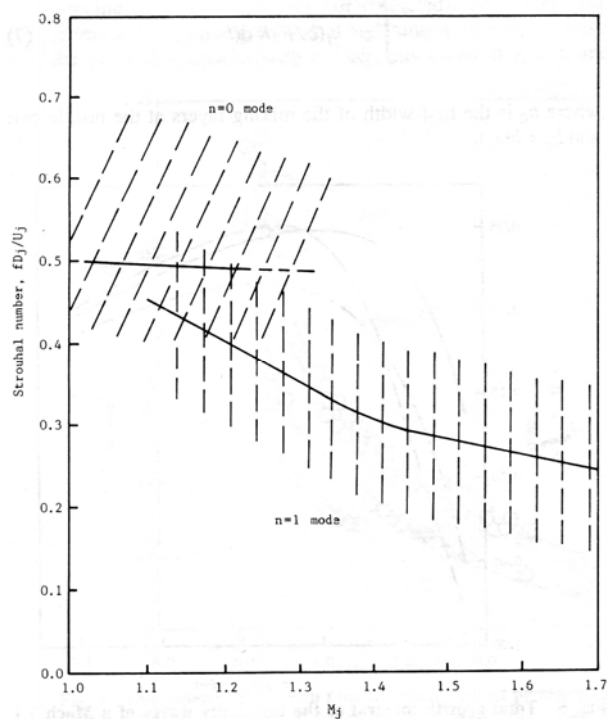


Figure 3.12. Range of the most amplified axisymmetric and helical instability wave modes of cold supersonic jets

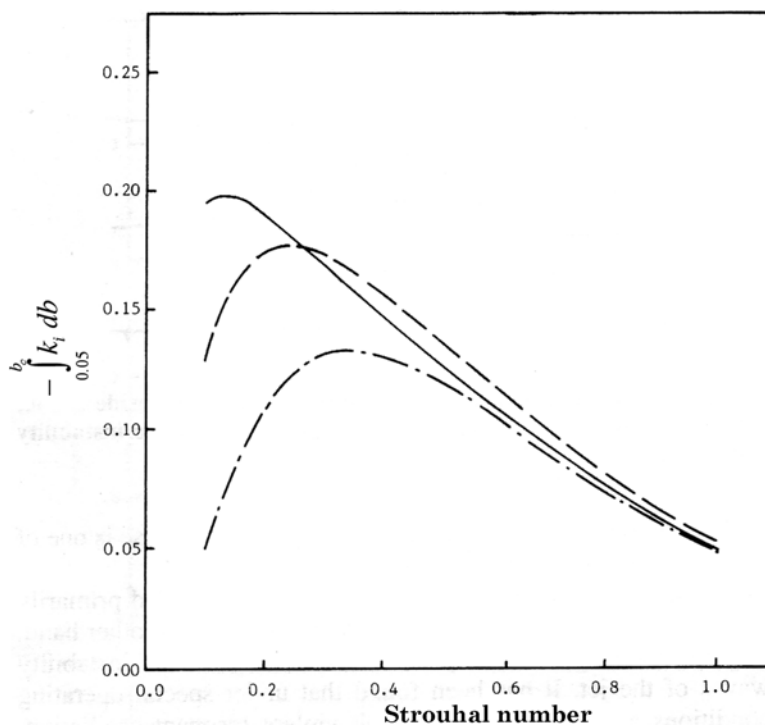


Figure 3.13. Total growth integral of the instability waves of a Mach 1.3 jet at $T_j/T_a = 2.0$ vs Strouhal number: --- $n = 0$; — $n = 1$; and - · - · - $n = 2$ mode.

Figure 3.10 shows the values of the total growth integral of the lowest three azimuthal modes, $n = 0, 1, 2$, as functions of Strouhal number for a Mach 1.1 cold jet ($T_r = T_a$). This figure shows that the axisymmetric mode ($n = 0$) has a slightly higher total growth than the other modes. The maximum amplification occurs at Strouhal number 0.5. The helical mode ($n = 1$) has a slightly smaller total amplification that peaks at a Strouhal number of 0.4. It is found, however, that the total amplification of the axisymmetric mode becomes smaller relative to the helical mode as the jet Mach number increases. At jet Mach number 1.4 the helical mode has the highest amplification of all the modes, as can easily be seen in Figure 3.11. This means that at low supersonic Mach numbers the axisymmetric mode dominates. The dominance gradually diminishes as the Mach number increases. At about $M_j = 1.3$ the helical mode becomes the dominant mode. Figure 3.12 shows the most amplified instability wave Strouhal number for the axisymmetrical and helical mode instability waves as functions of the jet Mach number ($T_r = T_a$). Obviously the axisymmetric mode wave peaks at a higher frequency and is an important wave mode only up to a Mach number of 1.3. The helical instability wave peaks at a lower frequency. It is the most amplified wave for $M_j > 1.3$. The shaded regions in Figure 3.12 represent the parameter space in which the unstable waves have significant total growth and hence are most likely to be observed.

The growth rates of the Kelvin-Helmholtz instability waves are strongly affected by the jet temperature. As the jet-to-ambient temperature ratio increases, the total growth of the axisymmetric mode instability waves becomes smaller and smaller when compared with the helical mode waves. Thus, they become less and less important. Figure 3.13 shows the total growth integrals of the $n = 0, 1$, and 2 modes as functions of Strouhal number for a Mach 1.3 hot jet at $T_j/T_a = 2.0$ (T_j is the fully expanded jet temperature). Clearly, the helical instability wave mode ($n = 1$) is dominant. The most amplified instability wave now has a Strouhal number of 0.13. This is substantially lower than that of a cold jet. In general, the Strouhal number of the most amplified instability wave decreases with an increase in T_j/T_a . In addition, it decreases with an increase in jet Mach number.

3.5 Super Resonance

As previously discussed, a duct or a diffuser can support a variety of normal duct modes of discrete frequency. If one of the frequencies falls into the unstable range of a jet, then resonance will result. Figure 3.14 shows a feedback loop formed inside a duct between an acoustic normal mode and a large scale instability wave of the jet. The jet shear layer near the nozzle exit is most receptive to excitations induced by the normal mode of the duct. Since the shear layer of the jet is thin just downstream of the nozzle, the growth rate of the instability wave is large. Thus, the excited instability wave grows rapidly as it propagates downstream. When the instability wave acquires a large amplitude, its oscillatory motion feeds energy into the duct mode. The duct mode, in turn, excites more instability waves. In this way, the feedback loop is closed and an acoustic resonance occurs.

Now as pointed out in the last section, different frequencies of an instability wave mode attain different total growth. There is, however, a frequency for which the total growth is the largest. Now if the frequency of the duct mode in the feedback loop coincides or very nearly coincides with the frequency of maximum growth of the same mode of instability wave, then the feedback would be most intense. Such a resonance is referred to as super resonance. Super resonance is violent and could lead to structural damage to an engine test cell.

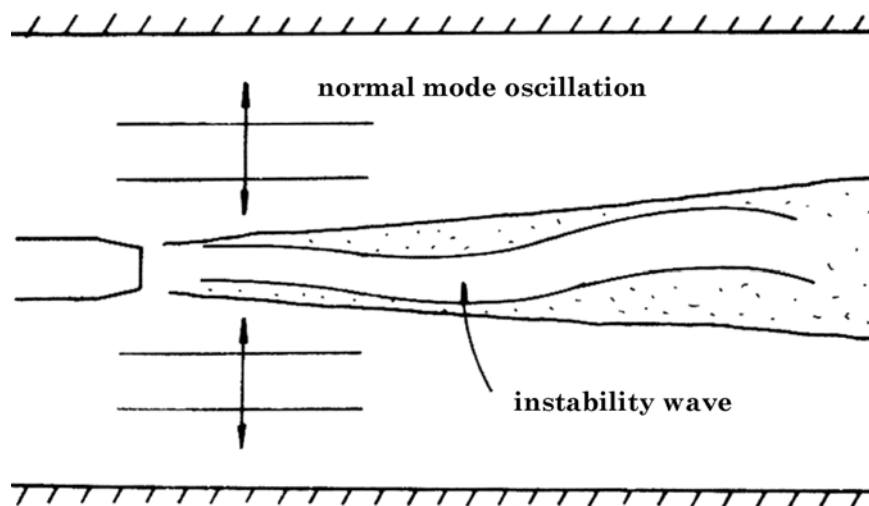


Figure 3.14. Schematic diagram of a feedback loop formed inside a duct between an acoustic normal duct mode and a large-scale instability wave of the jet.

References

- AHUJA, K.K. 1984 Basic experimental study of the coupling between flow instabilities and incident sound. *J. Sound & Vib.* **83**, 433–439.
- AHUJA, K.K. & BURRIN, R.H. 1984 “Control of flow separation by sound.” *AIAA paper* 84-2298.
- AHUJA, K.K., LEPICOVSKY, J. & BURRIN, R.H. 1982 “Noise and flow structures of tone excited jet.” *AIAA J.* **20**, 1700–1706.
- AHUJA, K.K. & TAM, C.K.W. 1982 A note on the coupling between flow instabilities and incident sound. *J. Sound & Vib.* **83**, 433–439.
- AHUJA, K.K., WHIPKEY, R.R. & JONES, G.S. 1983 Control of turbulent boundary layer flows by sound. *AIAA paper* 83-0726.
- BHAT, T.R.S. 2001 Boeing jet noise data.
- BECHERT, D.W. 1983 A model of the excitation of large scale fluctuations in a shear layer, *AIAA paper* 88-0724.
- CHAN, Y.Y. & WESTLEY, R. 1973 Directional acoustic radiation generated by spatial jet instability, *Can. Aero. & Space Inst. Trans.* **6**, 36–41.
- DAHL, M.D. & PAPAMOSCHOU, D. 2000 Analytical predictions and measurements of the noise radiated from supersonic coaxial jets. *AIAA J.* **38**, 585–591.
- DASH, S.M., WOLF, D.E. & SEINER, J.M. 1985. Analysis of turbulent underexpanded jets. PART 1. Parabolized Navier-Stokes model, SCIPVIX. *AIAA J.* **23**, 505–514.
- DAVIES, M.G. & OLDFIELD, D.E.S. 1962. Tones from a choked axisymmetric jet. *Acustica* **12**, 257–277.
- DAVIES, M.G. & OLDFIELD, D.E.S. 1962. Tones from a choked axisymmetric jet. PART 2. The self-excited loop and mode of oscillation. *Acustica* **12**, 267–277.
- HAMMITT, A.G. 1961 The oscillation and noise of an overpressure sonic jet. *J. Aerospace Sci.* **28**, 673–680.
- HARPER-BOURNE, M. & FISHER, M.J. 1974. The noise from shock waves in supersonic jets. *AGARD-CP-131* **11**, 1–13.
- LEPICOVSKY, J., AHUJA, K.K. & BURRIN, R.H. 1985 Tone excited jets. PART 3. Flow measurements. *J. Sound & Vib.* **102**, 71–91.
- LIEPMANN, H. & PUCKETT, A.E. 1947 *Introduction to Aerodynamics of a Compressible Fluid*. John Wiley & Sons, Inc. New York, 1947, pp. 239-241.
- LIEPMANN, H. & ROSHKO, A. 1957 *Elements of Gas Dynamics*. John Wiley & Sons, Inc., New York, 1957.

- MASSEY, K., AHUJA, K.K., JONES, R. III & TAM, C.K.W. 1994. Screech tones of supersonic heated free jets. *AIAA Paper* 94-0141.
- MICHALKE, A. 1984 Survey on jet instability theory. *Prog. Aerospace Sci.* **21**, 159–199.
- MILES, J.W. 1958 On the disturbed motion of a plane vortex sheet. *J. Fluid. Mech.* **4**, 538–552.
- MURDOCK, P.J. 1980 The generation of a Tollmien-Schlichting wave by a sound wave. *Proc. Royal Soc. Lond.* **A372**, 517–534.
- NORUM, T.D. & BROWN, M.C. 1993 Simulated high-speed flight effects on supersonic jet noise. *AIAA Paper* 93–4388
- NORUM, T.D. & SEINER, J.M. 1982a. Measurements of static pressure and far field acoustics of shock-containing supersonic jets. *NASA TM* 84521.
- NORUM, T.D. & SEINER, J.M. 1982b. Broadband shock noise from supersonic jets. *AIAA J.* **20**, 68–73.
- NORUM, T.D. 1983. Screech suppression in supersonic jets. *AIAA J.* **21**, 235–240.
- OERTEL, H. 1979 Mach wave radiation of hot supersonic jets. In *Mechanics of Sound Generation in Flows* (ed. E.A. Muller), Springer-Verlag, 1979, pp. 275–281.
- OERTEL, H. 1980 Mach wave radiation of hot supersonic jets investigated by means of the shock tube and new optical techniques. *Proc. Of the 12th Intl. Symp. On Shock Tubes and Waves. Jerusalem* (ed. A; Lifshitz & J. Rom), pp. 266–275.
- OERTEL, H. 1982 Coherent structures producing Mach waves inside and outside of the supersonic jet. Structure of Complex Shear Flow. *IUTAM Symp. Marseille*.
- PACK, D.C. 1950. A note on Prandtl's formula for the wave-length of a supersonic gas jet. *Q.J. Mech. Appl. Math.* **3**, 173–181.
- PANDA, J. 1998 Shock oscillation in underexpanded screeching jets. *J. Fluid Mech.* **363**, 173.
- PANDA, J., RAMON, G. & ZAMAN, K.B.M.Q. 2003 Underexpanded screeching jets from circular, rectangular and elliptic nozzles. *NASA Tech. Memo* 212481.
- PANDA, J. & SEASHOLTZ, R.G. 1999 Measurement of shock structure and shock-vortex interaction in underexpanded jets using Rayleigh scattering. *Phys. Fluids* **11**, 3761.
- PANDA, J., SEASHOLTZ, R.G. & ELAM, K.A. 2003 Further progress in noise source identification in high-speed jets. *AIAA paper* 2003-3126.
- PAPAMOSCHOU, D. & ROSHKO, A. 1986 Observations of supersonic free shear layers. *AIAA paper* 86-0162.
- POWELL A. 1953 On the noise emanating from a two-dimensional jet above the critical pressure. *Aeronautical Quarterly* **4**, 103–122
- POWELL A. 1953a On the mechanism of choked jet noise. *Proc. Phys. Soc. London* **B66**, 1039–1056.

- POWELL A. 1953b The noise of choked jets. *J. Acoust. Soc. Amer.* **25**, 385–389.
- PRANDTL L. 1904. Stationary waves in a gaseous jet. *Physikalische Zeitschrift* **5**, 599–601.
- RAMAN, G. 1996 Screech tones from rectangular jets with spanwise oblique shock cell structures. *AIAA paper* 96-0643.
- ROSEFJORD, T.J & TOMS, H.L. 1975. Recent observations including temperature dependence of axisymmetric jet screech. *AIAA J.* **13**, 1384–1386.
- SEDOV, L.I. 1959 *Similarity and Dimensional Methods in Mechanics*. Academic Press, New York.
- SEINER, J.M. 1984. Advances in high speed jet aeroacoustics. *AIAA Paper* 84-2275.
- SEINER, J.M., DASH, S.M. & WOLF, D.E. 1985. Analysis of turbulent underexpanded jets. PART 2. Shock noise features using SCIPVIS. *AIAA J.* **23**, 669–677.
- SEINER, J.M., MANNING, J.C. & PONTON, M.K. 1986. The preferred spatial mode of instability for a Mach 2 jet. *AIAA Paper* 86-1942.
- SEINER, J.M., MANNING, J.C. & PONTON, M.K. 1987. Model and full scale study of twin supersonic plume resonance. *AIAA Paper* 87-0244.
- SEINER, J.M. & NORUM, T.D. 1979. Experiments on shock associated noise of supersonic jets. *AIAA Paper* 79-1526.
- SEINER, J.M. & NORUM, T.D. 1980. Aerodynamic aspects of shock containing jet plumes. *AIAA Paper* 80-0965.
- SEINER, J.M., PONTON, M.K., JANSEN, B.J. & LAGEN, N.T. 1992. The effect of temperature on supersonic jet noise emission. *AIAA Paper* 92-02-046.
- SEINER, J.M. & YU, J.C. 1984. Acoustic near-field properties associated with broadband shock noise. *AIAA J.* **22**, 1207–1215.
- SHAPIRO, P.J. 1977 The influence of sound upon laminar boundary layer instability. *Acoustics and Vibration Laboratory Report* 83458-83560-1. M.I.T.
- SHERMAN, P.M., GLASS, D.R. & DULEEP, K.G. 1976. Jet flow field during screech. *Appl. Sci. Res.* **32**, 283–303.
- TAM, C.K.W. 1971 Directional acoustic radiation generated by shear layer instability. *J. Fluid Mech.* **46**, 757–768.
- TAM, C.K.W. 1978 Excitation of instability waves in a two-dimensional shear layer by sound. *J. Fluid Mech.* **89**, 357–371.
- TAM, C.K.W. 1981 The excitation of Tollmien-Schlichting waves in low subsonic boundary layers by free stream sound waves. *J. Fluid Mech.* **109**, 483–501.
- TAM, C.K.W. 1987. Stochastic model theory of broadband shock associated noise from supersonic jets. *J. Sound Vib.* **116**, 265–302.

- TAM, C.K.W. 1988. The shock cell structure and screech tone frequency of rectangular and non-axisymmetric supersonic jets. *J. Sound Vib.* **121**, 135–147.
- TAM, C.K.W. 1990. Broadband shock associated noise of moderately imperfectly expanded supersonic jets. *J. Sound Vib.* **140**, 55–71.
- TAM, C.K.W. 1991. Broadband shock associated noise from supersonic jets in flight. *J. Sound Vib.* **151**, 131–147.
- TAM, C.K.W. 1992. Broadband shock associated noise from supersonic jets measured by a ground observer. *AIAA J.* **30**, 2395–2401.
- TAM, C.K.W. 1995 Supersonic jet noise. *Annual Review of Fluid Mech.* **27**, 17–43
- TAM, C.K.W. 1998 Influence of nozzle geometry on the noise of high-speed jets. *AIAA J.* **36**, 1396–1400.
- TAM, C.K.W. 2005 Dimensional analysis of jet noise data. *AIAA paper* 2005-2938 (to appear in the *AIAA J.*).
- TAM, C.K.W. & AURIAULT, L. 1999 Jet mixing noise from fine-scale turbulence. *AIAA J.* **37**, 145–153.
- TAM, C.K.W. & BURTON, D.E. 1984 Sound generated by instability waves of supersonic flows. PART 2. Axisymmetric Jets. *J. Fluid Mech.* **138**, pp. 273–295.
- TAM, C.K.W. & CHEN, P. 1993. Turbulent mixing noise from supersonic jets. *AIAA J.* **32**, 1774–1780.
- TAM, C.K.W., CHEN, P. & SEINER, J.M. 1992. Relationship between instability waves and noise of high-speed jets. *AIAA J.* **30**, 1747–1752.
- TAM, C.K.W. & GANESAN, A. 2004 A modified $k - \varepsilon$ turbulence model for calculating the mean flow and noise of hot jets. *AIAA J.* **42**, 26–34.
- TAM, C.K.W., GOLEBIEWSKI, M. & SEINER, J.M. 1996 On the two components of turbulent mixing noise from supersonic jets. *AIAA paper* 96-1716.
- TAM, C. K. W. & HU, F. Q. 1989a On the three families of instability waves of high-speed jets. *J. Fluid Mech.* **201**, 447–483.
- TAM, C.K.W., JACKSON, J.A. & SEINER, J.M. 1985. A multiple-scales model of the shock cell structure of imperfectly expanded supersonic jets. *J. Fluid Mech.* **153**, 123–149.
- TAM, C.K.W. & MORRIS, P.J. 1985 Tone excited jets. PART 5. A theoretical model and comparison with experiment. *J. Sound & Vib.* **102**, 119–151.
- TAM, C.K.W., PASTOUCHENKO, N.N. & VISWANATHAN, K. 2005 Fine scale turbulence noise from hot jets. *AIAA J.* **43**, 1675–1683.
- TAM, C.K.W. & REDDY, N.N. 1996 Prediction method for broadband shock associated noise from supersonic rectangular jets. *J. Aircraft* **33**, 298–303.

- TAM, C.K.W., SEINER, J.M. & YU, J.C. 1986. Proposed relationship between broadband shock associated noise and screech tones. *J. Sound Vib.* **110**, 309–321.
- TAM, C.K.W., SHEN, H. & RAMAN, G. 1997 Screech tones of supersonic jets from beveled rectangular nozzles. *AIAA J.* **35**, 1119–1125.
- TAM, C.K.W. & TANNA, H.K. 1982 Shock associated noise of supersonic jets from convergent-divergent nozzles. *J. Sound & Vib.* **81**, 337–358.
- TAM, C.K.W. & ZAMAN, K.B.M.Q. 2000 Subsonic jet noise from axisymmetric and tabbed nozzles. *AIAA J.* **38**, 592–599.
- TANNA, H.K. 1977. An experimental study of jet noise. PART 1. Turbulent mixing noise. PART 2. Shock associated noise. *J. Sound Vib.* **50**, 405–444.
- TROUTT, T.R. & McLAUGHLIN, D.K. 1982. Experiments on the flow and acoustic properties of a moderate Reynolds number supersonic jet. *J. Fluid Mech.* **116**, 23–156.
- VISWANATHAN, K. 2002 Aeroacoustics of hot jets. *AIAA paper* 2002-2481.
- VISWANATHAN, K. 2002 Analysis of two similarity components of turbulent mixing noise. *AIAA J.* **40**, 1735–1744.
- VISWANATHAN, K. 2003 Jet aeroacoustic testing: issues and implications. *AIAA J.* **41**, 1674–1689.
- VISWANATHAN, K. 2004 Aeroacoustics of hot jets. *J. Fluid Mech.* **516**, 39–82.
- VISWANATHAN, K. & CLARK, L. 2004 Effect of nozzle internal contour on jet aeroacoustics. *Intl. J. Aeroacoustics* **3**, 103–135.
- WESTLEY, R. & WOOLEY, J.H. 1969. The near field sound pressures of a choked jet during a screech cycle. *AGARD CP 42* **23**, 1–13.
- WESTLEY, R. & WOOLLEY, J.H. 1970. Shock cell noise-mechanisms, the near field sound pressure associated with spinning screech mode. *Conference on Current Development in Sonic Fatigue, University of Southampton, England.*
- WESTLEY, R. & WOOLLEY, J.H. 1975. The near field sound pressures of a choked jet when oscillating in the spinning mode. *AIAA Paper* 75-479.
- WHITE, F.M. 2003 *Fluid Mechanics*, Chapter 5. McGraw-Hill, 2003 (5th Edition).
- YAMAMOTO, K., BRAUSCH, J.F., JANARDOM, B.A., HOERST, D.J., PRICE, A.O. & KNOTT, P.R. 1984 Experimental investigation of shock-cell noise reduction for single stream nozzles in simulated flight. *Comprehensive Data Report, Volume 1. NASA CR-168234*

Part II. Recommendations

1. Suppression of Super Resonance: the Method of Barriers

Super resonance is extremely violent. Once it occurs, it must be suppressed; otherwise the test cell could suffer severe structural damage. Engine development may be interrupted. In the past, AEDC had found that the spraying of large quantities of water could damp out the resonance to allow the testing to continue. The installation of Helmholtz resonators tuned to the resonance frequency also was somewhat effective in reducing resonance amplitude.

Here as a part of the consultant's report, a possible new method for the suppression of super resonance is described below.

Super resonance is driven by a feedback loop. So a natural way to suppress such a resonance is to break up the feedback. The feedback loop consists of two major components. They are the instability waves of the jet flow and the normal acoustic modes of the diffuser/duct of the engine test cell. Now for high temperature circular jets, the most amplified instability waves have azimuthal wave number equal to ± 1 . These are helical or flapping mode instability waves. For rectangular jets, the most amplified waves belong to the antisymmetric flapping mode. Now, in order for the instability wave to couple to a duct acoustic mode, the duct mode must also be a flapping mode (or a combination of left and right hand helical mode, $n = \pm 1$). This is a necessary condition for coupling the oscillatory motion of the duct mode to the flapping motion of the instability wave of the jet. So a possible suppression method is to insert barriers inside a diffuser/duct to disallow any flapping duct modes. This can be achieved by installing barriers inside the duct so that there is no symmetric plane across the center of the duct. A flapping duct mode requires such a symmetry. A barrier configuration that disallow flapping duct modes is as shown in Figure A. It is easy to see for a barrier configuration as shown, there is no symmetric plane through the center of the duct. In the absence of mode matching between the most amplified instability waves and duct modes, the feedback loop is broken and super resonance may be avoided.

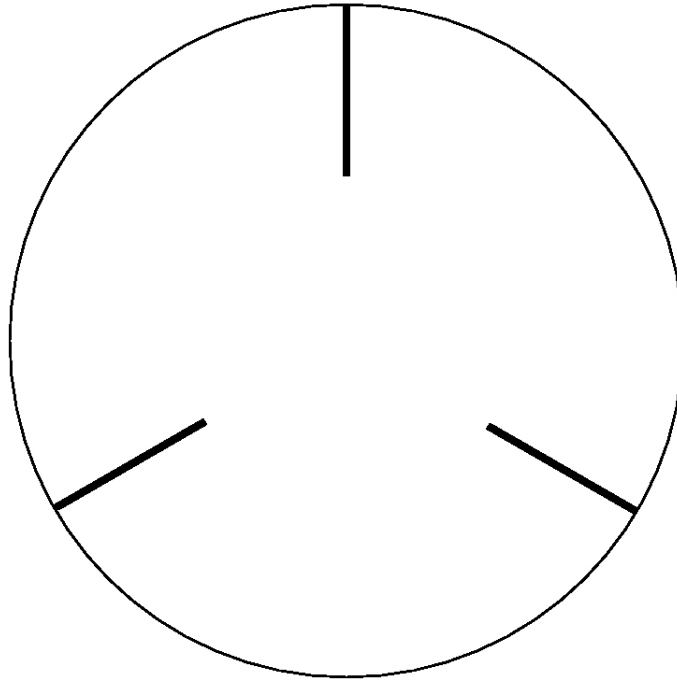


Figure A. Schematic diagram of barriers inserted inside a diffuser to disallow flapping duct modes

II. Establishing a CAA Capability at AEDC

In planning for the establishment of a CAA capability at AEDC, it is important to recognize that this capability has to be consistent with the overall mission of AEDC. With this as the background, it is easy to identify the two main purposes for establishing a CAA capability at AEDC. They are:

1. To support engine testing and development.
2. To support future engine test cell design and operation.

The principal activities associated with the first purpose are:

- a. Computation of the acoustic characteristics of existing engine test cells.
- b. Computation of the aeroacoustic characteristics of jet engine exhaust.
- c. Offering a trouble-shooting capability for unexpected problems encountered in routine engine tests.

To accomplish (a) and (b) engineers may use computer codes developed in-house or externally. The use of external codes, however, still requires a capable in-house engineer to run the code. Short term problems would best be handled by an in-house CAA person. Longer term problems may be resolved with assistance from outside consultants.

To support future engine test cell design and operations would require an in-house engineer with deeper understanding of aeroacoustics of engine test cells and CAA methodology. This is necessary and desirable as test cell geometry and operating conditions may change during the design phase. CAA codes required may be developed in-house with consultant assistance or developed externally with input and participation of AEDC engineers.

PERSONNEL REQUIREMENTS — It is believed that AEDC should have, at least, one on-site engineer with extensive acoustic experience and knowledge of CAA methodology. It is important to point out that just having programming skill, even with CFD experience, is not sufficient. Many aeroacoustic problems cannot be solved by computing alone. There is a need to know or have a fair idea of the physics of the problem. It would be good to add a junior CAA person so as to form a basic team. This may be a CFD person with strong desire to switch over to the CAA area. They can work with existing CFD engineers to provide a core CAA capability at AEDC.

CODE DEVELOPMENT STRATEGY — In CFD, an often adopted strategy is to acquire an all-purpose CFD code. Such a code would allow engineers to do numerous types of CFD problems. This is a good strategy for CFD, as most engineers would only need to learn to run a single code. In CAA, this may not be the best strategy. The reason is simple. CAA problems are often very dissimilar. Each class of problems has its own characteristics. As a result, there is, at the present time, no all-purpose CAA code. Also the run time for CAA codes is, in most cases, very long. To keep the run time reasonable, it is necessary to use codes that are optimized for the particular class of problem one wishes to solve. All-purpose code cannot be highly optimized. So the run time will inevitably be fairly long. With the above in mind, it is recommended that the development of a set of dedicated CAA codes for engine testing and development purposes be regarded as a priority in the establishment of a CAA capability at AEDC.